Ultrafast chemical dynamics simulations for experiments

Lauren Bertram

New College

University of Oxford

A thesis submitted for the degree of

Doctor of Philosophy

Trinity 2024

Acknowledgements

Firstly, I would like to say an enormous thank you to my supervisor, Prof. Adam Kirrander, for your endless support, encouragement and guidance throughout my DPhil studies. I have learned so much and you have helped me grow into a much more confident scientist. I feel incredibly fortunate to have had the opportunity to work with you over the last four years and am very grateful to be able to spend another year in the group.

I would also like to thank the other members of the Kirrander group (past and present) for fruitful discussions and for making this experience unforgettable. They are Dr Kyle Acheson, Dr Lewis Hutton, Dr Andrés Moreno Carrascosa, Dr Mats Simmermacher, Joe Cooper, Jakub Kara, James Merrick and Eirik Moen Liane. I look forward to another year of fun together.

To Joe, I cannot thank you enough. I could not have made it through the past four years without you. You have always been there for me, from answering my countless questions to supporting me through every challenge. I am extremely thankful to have such a supportive partner by my side.

Finally, I would like to thank my family, especially my parents, who have been a constant source of encouragement throughout my studies. Their never-ending belief in me has continually inspired me to pursue what I love.

Abstract

Photochemistry is a crucial discipline that governs the interaction of molecules with light, but it presents significant challenges due to the difficulties of coupled nuclear and electronic dynamics. While new light sources have enabled measurements on ultrafast timescales, these experiments often yield results that are difficult to interpret and typically require substantial theoretical support. This thesis utilises electronic structure calculations and nonadiabatic dynamics simulations to shed light on a number of recent experiments. Three examples of complex chemical systems are explored, focusing on the investigation of potential energy surfaces and photodynamics, with the findings compared to ultrafast experiments.

First, trajectory surface hopping simulations are employed to study the photoinduced ring-conversion reaction in cyclopentadiene, revealing that photorelaxation leads to a mixture of hot cyclopentadiene and the photoproduct bicyclo[2.1.0]pentene. Observables for novel ultrafast X-ray scattering experiments are computed and the possibility of retrieving electronic information from the scattering signal is discussed. Next, six azanaphthalene systems are investigated, beginning with static analysis to explain the variations in internal conversion and intersystem crossing rates across the molecular series. This allowed for the interpretation of recent transient absorption spectroscopy experiments and illustrated how subtle changes in the nitrogen positions can significantly impact the photochemical behaviour. Nonadiabatic dynamics simulations are subsequently performed on a representative subset, confirming the qualitative predictions, albeit with some discrepancy in the timescales. Finally, the Rydberg state dynamics in N,N'-dimethylpiperazine are simulated as an example of excited state charge transfer. The time-resolved photoelectron spectrum is predicted and displays how the molecule slowly converts between two excited state structures.

Ultimately, this thesis demonstrates how computational simulations allow greater insight into the complex photochemical dynamics observed in state-of-the-art experiments.

Contents

Appendices

List of Figures

List of Abbreviations

ADC(2)	Algebraic diagrammatic construction to the second-order
AIMS	*Ab initio* multiple spawning
BE	Binding energy
BOA	Born-Oppenheimer approximation
BP	Bicyclo[2.1.0]pentene
CASPT2	Complete active space second-order perturbation theory
CASSCF	Complete active space self-consistent field
CC	Coupled cluster
CC2	Second-order approximate coupled cluster singles and doubles
CCSD	Coupled cluster singles and doubles
CI	Conical intersection
CISD	Configuration interaction singles and doubles
COSMO	Conductor-like screening model
CP	Cyclopentadiene
DFT	Density functional theory
DMP	*N*,*N*′-dimethylpiperazine
FC	Franck-Condon
FCI	Full configuration interaction
FEL	Free-electron laser
FWHM	Full width at half maximum
GGA	Generalised gradient approximation
HF	Hartree-Fock
IAM	Independent atom model
IC	Internal conversion
IP	Ionisation potential

IRC	Intrinsic reaction coordinate
ISC	Intersystem crossing
LIIC	Linear interpolation in internal coordinates
LDA	Local density approximation
MCE	Multiconfigurational Ehrenfest
MCSCF	Multiconfigurational self-consistent field
MCTDH	Multiconfigurational time-dependent Hartree
MECI	Minimum energy conical intersection
MECP	Minimum energy crossing points
MEP	Minimum energy pathway
MP2	Møller-Plesset Perturbation theory, second-order
MS-CASPT2	Multi-state complete active space second-order perturbation theory
PDF	Pair distribution function
PE	Potential energy
PES	Potential energy surface
RASSCF	Restricted active space self-consistent field
RMSD	Root mean square deviation
SA-CASSCF	State-averaged complete active space self-consistent field
SCS	Spin-component scaled
SOC	Spin-orbit coupling
SOCMEs	Spin-orbit coupling matrix elements
TAS	Transient absorption spectroscopy
TDDFT	Time-dependent density functional theory
TDSE	Time-dependent Schrödinger equation
TISE	Time-independent Schrödinger equation
TP	Tricyclo[2.1.0.0^{2,5}]pentane
TRPES	Time-resolved photoelectron spectroscopy
TS	Transition state
TSH	Trajectory surface hopping
UED	Ultrafast electron diffraction

UXS	Ultrafast X-ray scattering
VR	Vibrational relaxation
XFEL	X-ray free-electron laser
XMS-CASPT2	Extended multi-state complete active space second-order perturbation theory
ZPE	Zero-point energy

List of Publications

Publications included in this thesis:

- Lauren Bertram, Peter M. Weber and Adam Kirrander. "Mapping the photochemistry of cyclopentadiene: from theory to ultrafast X-ray scattering". *Faraday Discussions*, 2023, **244**, 269.
- Lisa Huang, Lauren Bertram, Lingyu Ma, Nathan Goff, Stuart W. Crane, Asami Odate, Thomas Northey, Andrés Moreno Carrascosa, Mats Simmermacher, Sri Bhavya Muvva, Joseph D. Geiser, Matthew J. Lueckheide, Zane Phelps, Mengning Liang, Xinxin Cheng, Ruaridh Forbes, Joseph S. Robinson, Matthew J. Hayes, Felix Allum, Alice E. Green, Kenneth Lopata, Artem Rudenko, Thomas J. A. Wolf, Martin Centurion, Daniel Rolles, Michael P. Minitti, Adam Kirrander, Peter M. Weber. "The Ring-Closing Reaction of Cyclopentadiene Probed with Ultrafast X-ray Scattering". *The Journal of Physical Chemistry A*, 2024 **128**, 4992.
- Malcom Garrow, Lauren Bertram, Abi Winter, Andrew W. Prentice, Stuart W. Crane, Paul D. Lane, Stuart J. Greaves, Martin J. Paterson, Adam Kirrander and Dave Townsend, "Excited state dynamics of azanaphthalenes reveal opportunities for the rational design of photoactive molecules", *Communications Chemistry*, 2025, **8**.

Other publications that are not included in this thesis:

- Lauren Bertram, Samuel J. Roberts, Matthew W. Powner, Rafał Szabla. "Photochemistry of 2-thiooxazole: a plausible prebiotic precursor to RNA nucleotides". *Physical Chemistry Chemical Physics*, 2022, **24**, 21406.

1
Introduction

1.1 Photochemistry

Photochemistry is the study of chemical processes arising from the absorption of one or more photons. Photoexcitation induces dynamics leading to chemical reactions, which play a fundamental role in processes seen in nature such as photosynthesis [1], vision [2–4] and the formation of vitamin D [5–7]. Moreover, there are numerous applications of photochemistry and photophysics, which include photovoltaics [8, 9], organic light-emitting diodes (OLEDs) [10–12], photodynamic therapies [13, 14], and others.

The basis of photochemistry is that upon absorption of a photon, a molecule is excited from the electronic ground state into a higher-lying electronic state, known as an excited state. Excited states are often unstable and can undergo a variety of decay mechanisms back to the ground state. These mechanisms are commonly depicted in a Jabłonski diagram [15] as shown in Fig. 1.1. In this example, the molecule is excited into a particular vibrational level in the S_2 state and following this electronic transition, vibrational relaxation (VR) occurs. The molecule can then undergo internal conversion (IC) into the S_1 state, which is a non-radiative transition that occurs between electronic states of the same multiplicity without the emission of a photon. From here, there are two photorelaxation pathways to the ground state, in which either IC or fluorescence can occur, where fluorescence is a radiative process that requires the emission of a photon. Alternatively, the molecule can access the triplet state from S_1 *via* intersystem crossing (ISC), which is a non-radiative process that occurs between two electronic states of different spin multiplicities. Once in the T_2 state, IC to the lowest energy triplet state, T_1, can take place. From here, the ground state can be reached by either ISC or emission of a photon, known as phosphorescence. It should be noted that both ISC and phosphorescence are formally spin-forbidden processes and hence, often occur on slower timescales compared to the respective processes between singlet states, namely, IC and fluorescence.

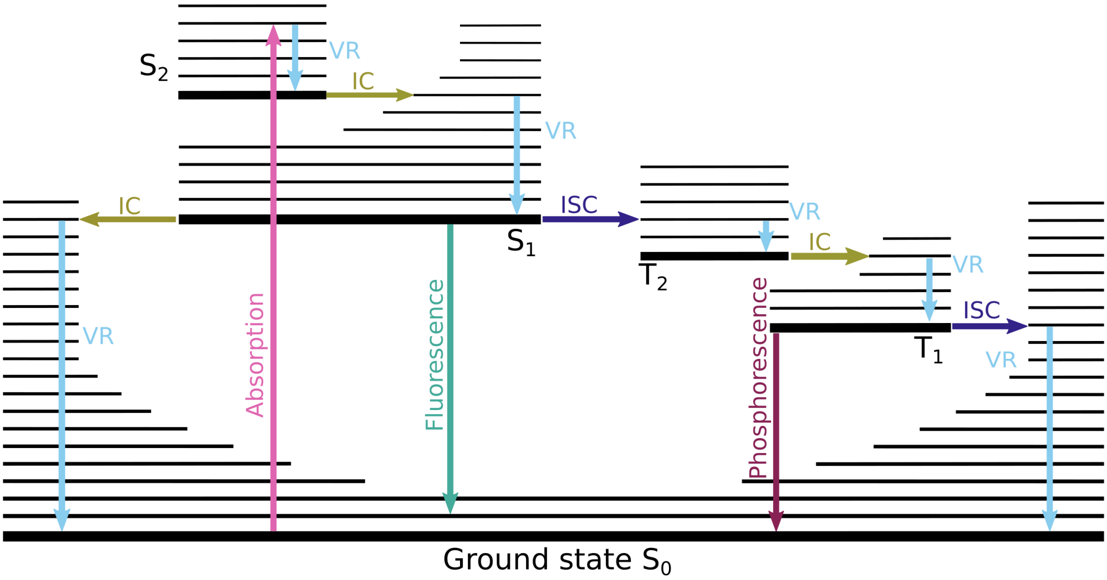

Figure 1.1: A Jabłonski diagram depicting the radiative and non-radiative decay processes in a molecule upon absorption of a photon, namely, fluorescence, phosphorescence, internal conversion (IC), intersystem crossing (ISC) and vibrational relaxation (VR).

This thesis focuses on exploring the non-radiative photorelaxation mechanisms occurring on ultrafast timescales, specifically in the range of femtoseconds (10^{-15} s) to picoseconds (10^{-12} s). These mechanisms are initiated by the excitation of a molecular wave packet to an excited state, which then evolves on this state until a crossing with another electronic state is reached, allowing IC to occur. In particular, the wave packet evolves on a potential energy surface (PES), which is a multidimensional landscape that depends on the nuclear coordinates in the molecule. An example of this process is illustrated in Fig. 1.2, where a wave packet is initially excited to the S_1 state in the Franck-Condon (FC) region of isomer A. The wave packet then traverses the S_1 PES, approximately following the gradient until it reaches a conical intersection (defined as CoIn in Fig. 1.2), where the S_1 and ground states become degenerate. The conical intersection facilitates a transition to the ground state through IC, resulting in either the formation of isomer B or the regeneration of isomer A, with the outcome strongly depending on the topography of the PES in this region, as well as the trajectory of the wave packet. This schematic example represents various *cis-trans* isomerisation reactions, including the isomerisation of retinal in Rhodopsin [4].

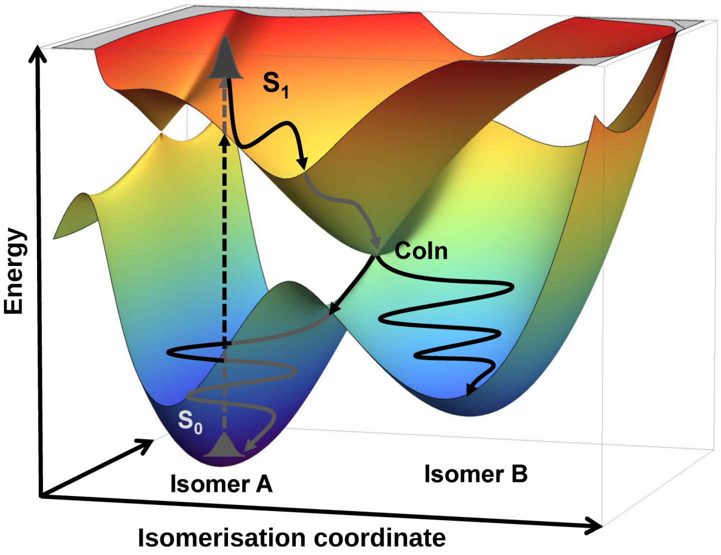

Figure 1.2: Schematic of a potential energy surface (PES) showing the excitation of a wave packet from the Franck-Condon (FC) region in Isomer A onto the S_1 state. The wave packet evolves on this state until the conical intersection (CoIn) with the ground state is accessed and IC to the ground state occurs either returning to Isomer A or forming Isomer B. Figure adapted from Ref. [16].

Understanding photorelaxation mechanisms, such as the example depicted in Fig. 1.2, may allow for new opportunities to control and design photochemical reactions. As an example, electronic excited states can have multiple types of character. Two examples encountered in this thesis are valence and Rydberg states. Valence states involve excitation purely within the valence orbitals, which are localised orbitals formed of the highest occupied atomic shell. In contrast, Rydberg states, involve excitation into Rydberg orbitals, which are large, diffuse atomic-like orbitals. These two types of excited states show very different dynamics after excitation, with Rydberg states generally leading to slower dynamics, while valence states give much faster decays. Therefore, a qualitative understanding of these mechanisms offers the potential to design new molecules for practical applications. Consequently, the field of photochemistry is a widely researched topic which has advanced significantly over the past few decades. This is largely due to developments in experimental techniques and theoretical methods for investigating these reactions, which will be discussed in the following sections.

1.2 Time-resolved experimental techniques

Time-resolved experimental techniques enable the observation of photoexcited processes in molecules by utilising a pump-probe scheme, with a typical set up shown in Fig. 1.3. First, a pump pulse is used to excite the molecule, initiating the photochemical reaction. A probe pulse is then employed at specific delay times to monitor the reaction dynamics. By varying the delay times Δt between the pump and probe pulses, information can be extracted about the dynamics of the system. A variety of experiments utilise a pump-probe scheme, and three relevant techniques will be discussed in the next section, each connected to the projects presented later in this thesis.

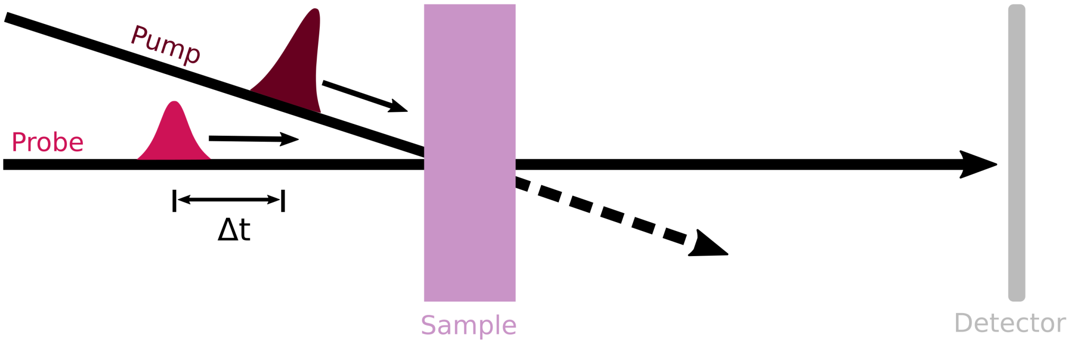

Figure 1.3: A typical pump-probe set up, where the system is excited by a pump pulse, and the photoexcited dynamics are monitored at certain time delays with a probe pulse.

1.2.1 Time-resolved photoelectron spectroscopy

Time-resolved photoelectron spectroscopy (TRPES) is an important technique to elucidate photoexcited dynamics [17–20]. Following excitation, a probe pulse ionises the molecule, and the kinetic energy of the emitted photoelectron is recorded at the detector as a function of pump-probe delay. The photoelectron kinetic energy is directly related to the binding energy, which is the energy required to remove an electron from a specific electronic state, and hence, is sensitive to the type of excited state probed. For instance, Fig. 1.4 shows a typical TRPES experiment, where the molecule is excited into the S_1 electronic state. After a certain delay time Δt a probe pulse ionises the molecule, in this schematic to the D_0 state, leading to the ejection of a photoelectron. The kinetic energy of this electron is the difference between the probe energy and the binding energy. Consequently, by knowing the kinetic energy, the binding energy of the photoelectron can be deduced.

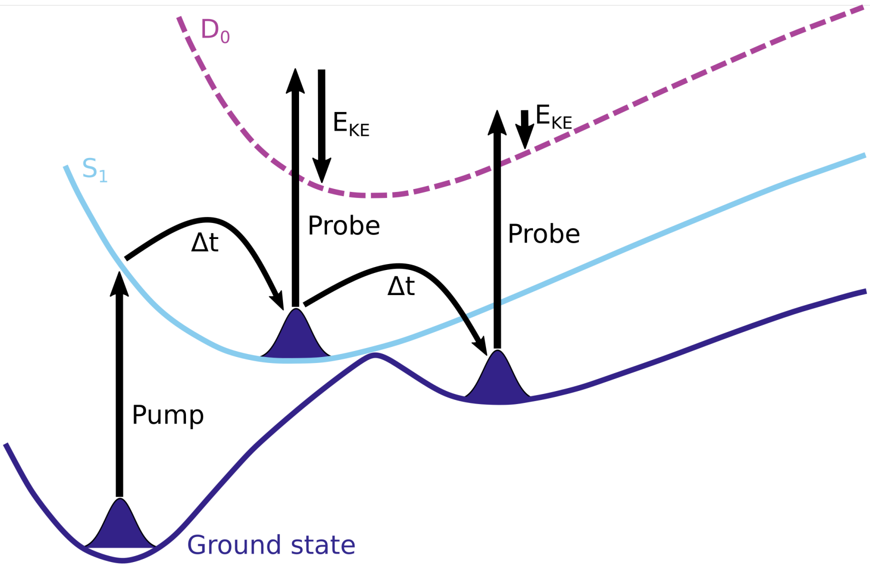

Figure 1.4: A time-resolved photoelectron spectroscopy (TRPES) scheme, utilising a pump-probe set up, where photoexcitation from the ground state occurs and at specific time delays a probe pulse ionises the molecule. The kinetic energy of the ejected photoelectron is defined as the difference between the probe pulse and the binding energy.

Figure 1.4 demonstrates how TRPES monitors changes in electronic states. At the first time delay Δt when the molecule is in the S_1 state, the emitted photoelectron has a large kinetic energy, which corresponds to a small binding energy. Conversely, at the subsequent time delay, when the molecule has returned to the ground state, the photoelectron's kinetic energy is smaller, leading to an increased binding energy. Therefore, variations in the binding energy indicate the molecule's progression on the PESs, tracking its relaxation across different electronic states and, indirectly, allowing for insights into the molecular geometry evolution throughout the photoexcited dynamics.

A key advantage of photoelectron spectroscopy is that the photoionisation cross-section, which is the likelihood of a specific transition from a neutral to an ionic state, is often non-zero for many transitions. Consequently, TRPES is a good technique for monitoring all types of excited states, including those that are typically dark in absorption spectroscopy. In this thesis, approximate methods are employed to calculate the TRPES observables. Specifically, the binding energy is determined by calculating the energy difference between the neutral and ionic states, while the photoelectron cross-section is approximated using the norm of the Dyson orbital, a one-electron orbital that describes the overlap between the neutral and ionic states.

1.2.2 Transient absorption spectroscopy

Transient absorption spectroscopy (TAS) [21] is another widely used spectroscopic method to study excited state dynamics in molecules. After excitation with the pump pulse, a probe pulse induces a transition from the current excited state to a higher-lying one. Therefore, TAS can monitor changes in absorption as a function of pump-probe delay times, providing insight into the reaction dynamics, which is illustrated in Fig. 1.5. This simplified schematic demonstrates the process of excited state absorption, where, after photoexcitation, the molecule evolves on the S_1 surface and undergoes a transition to S_2 when the probe pulse is employed. Following relaxation to the ground state, the second probe pulse induces a transition to S_1. Since these two transitions occur at different energies, corresponding changes will be observed in the transient absorption spectrum. By tracking these changes in absorption, photorelaxation pathways that proceed through IC or ISC can be inferred [22–24].

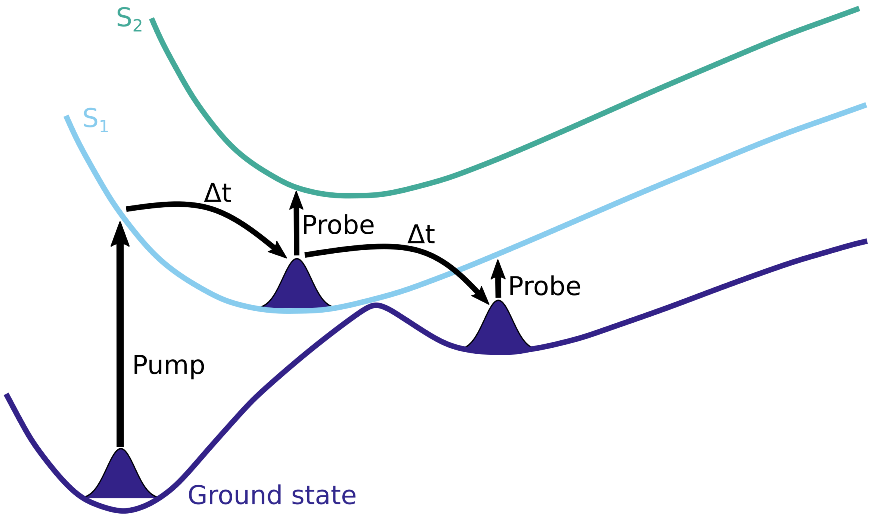

Figure 1.5: A schematic of a transient absorption spectroscopy (TAS) experiment illustrating excited state absorption. Following photoexcitation into an excited state, the probe pulse can induce a transition to a higher-lying state.

Similar to photoelectron spectroscopy, the probability of a particular transition in excited state absorption is determined by the photoabsorption cross-section, although now the transition occurs between two neutral states. This is accurately approximated by the square of the norm of the transition dipole moment, which corresponds to the off-diagonal element of the dipole matrix. This principle governs all photoabsorption processes and is therefore also relevant to the excitation processes induced by the pump pulse.

Furthermore, TAS has the ability to monitor multiple processes simultaneously. Besides excited state absorption, the transient absorption spectrum often contains information about ground state bleaching and stimulated emission. Ground state bleaching arises from the depletion of molecules in the ground state as a result of absorption following the pump pulse, though its detection depends on the energy of the probe pulse. Moreover, in some cases, the probe can stimulate the emission of a photon as the molecule relaxes back to the ground state. However, this process is not directly relevant to the work discussed later in this thesis.

1.2.3 Ultrafast X-ray scattering

Although TRPES and TAS provide insights into the nature of electronic states accessed as a molecule evolves following excitation, they do not directly reveal changes in molecular geometry. As a result, alternative methods are used to probe the structural dynamics of molecules, with ultrafast X-ray scattering (UXS) emerging as a particularly powerful technique [25]. This technique works by detecting the X-rays that are scattered off the electrons within a molecule. These scattered photons can be analysed to reveal the relative positions of atoms within the molecule. In particular, UXS utilises short, high-intensity X-ray pulses generated by X-ray free-electron lasers (XFELs) [26]. These pulses can probe ultrafast processes at the atomic and molecular levels, including nuclear dynamics.

UXS experiments typically employ a pump-probe scheme, as depicted in Fig. 1.6. The molecule is excited with an optical pump pulse, initiating the photochemical reaction. Following this, an X-ray probe pulse is utilised at different delay times and the X-rays scattered by the sample are then collected on a detector. The signal on the detector is typically recorded as a function of the momentum transfer vector $\mathbf{q}$, which is defined as the difference between the incident and scattered wave vectors $\mathbf{k}_0$ and $\mathbf{k}_s$, respectively. Moreover, the magnitude of the momentum transfer vector is related to the scattering angle θ as $q = 2|\mathbf{k}_0|\sin(\theta/2)$.

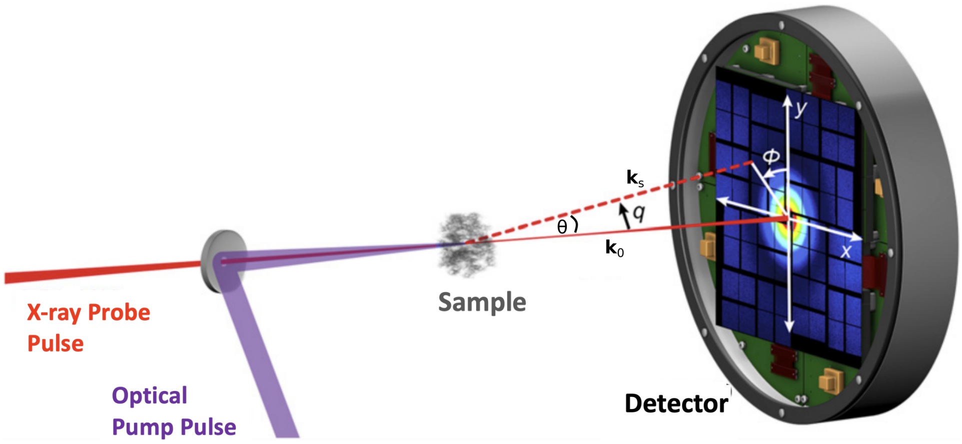

Figure 1.6: Schematic of an ultrafast X-ray scattering (UXS) experimental setup, where the molecule is photoexcited by an optical pump pulse and then an X-ray probe pulse is employed at different time delays. Figure adapted from Ref. [27].

The scattering patterns obtained from UXS experiments provide information about the structural dynamics in photoexcited processes in reciprocal space. However, to obtain real space structural information about the nuclear dynamics in a molecule, such as bond lengths, inversion can be performed [28]. Inversion involves Fourier transforming the scattering data into real space to obtain a pair distribution function (PDF), which describes the probability of finding two atoms at a specific distance from each other, allowing information about the atomic structure to be retrieved. Nevertheless, inversion can be challenging for a number of reasons. Firstly, converting a PDF into a molecular geometry is challenging without theory because the PDF only provides information about the distances between pairs of atoms and not the full three-dimensional arrangement of atoms in a molecule. Additionally, with the standard resolution and measurement range of current experiments, the PDF often has limited resolution, restricting the amount of information that can be extracted. Therefore, it is often necessary to combine theory with experiment to aid interpretation of the scattering signal.

In parallel, ultrafast electron diffraction (UED) is a closely related technique that uses an electron beam to probe the molecule instead of X-rays [29]. While UED offers similar capabilities to UXS, it provides additional scattering information from nuclei, thereby capturing more details about light elements. UED also benefits from a higher cross-section, resulting in a stronger overall signal. However, achieving high time-resolution with UED is complicated by space-charge effects within the electron pulse. In contrast, UXS, which only contains information about the electrons, often presents a clearer and more straightforward interpretation. Consequently, this thesis concentrates on UXS.

1.2.4 Comparison of experimental techniques

The techniques discussed in this section provide valuable insights into the ultrafast dynamics of molecules by examining different aspects of the system. For example, spectroscopic techniques such as TRPES and TAS probe energy gaps between different electronic states. Specifically, TRPES measures the energy gap between an excited state and an ionised state, while TAS tracks the difference between two excited states. Both approaches provide detailed information about population dynamics, with TRPES offering the additional advantage of detecting excited states that are typically dark in TAS. While these methods are able to track excited state population transfer and capture the timescales of electronic dynamics, they are less effective at providing information about nuclear dynamics. This limitation arises because electronic energy gaps can be identical across different nuclear geometries [30]. Consequently, these techniques cannot directly resolve structural changes.

In contrast, scattering techniques provide detailed information about changes in the molecular geometry by primarily mapping nuclear positions, as the core electrons closely resemble the positions of the nuclei. However, because nuclear dynamics dominate the signal over changes in electronic states, scattering techniques offer minimal information about the population dynamics and electronic state transitions [31].

These different techniques enable the key aspects of a system to be probed. For instance, if a molecule exhibits minimal changes in geometry, scattering methods may not reveal significant changes. Similarly, if there is little variation in the electronic states, spectroscopic techniques may not provide much insight. Therefore, the chosen experimental observable will alter depending on the dynamics of the molecule.

1.3 Connecting theory to experiment

Time-resolved experiments are commonly performed in parallel to theoretical studies to assist with the interpretation of experimental data and gain insight into the ultrafast processes occurring. In principle, UXS experiments can provide information about the structural dynamics of a system in real space; however, typically, supporting calculations are required [27, 32]. Additionally, experiments such as TRPES and TAS do not provide direct information about the evolution of molecular geometries. Furthermore, experiments can only infer the existence of certain nonadiabatic processes that cannot be directly observed. On the contrary, theory provides the framework to understand the fundamental principles governing these ultrafast dynamics on a molecular level. By simulating how a system evolves over time after photoexcitation, theory can predict the changes in electronic structure and molecular geometry that occur on ultrafast timescales and how these changes govern the outcome of photochemical processes.

In order to connect theory to experiment, it is important to accurately simulate the observables that experiments measure. Theoretical methods, such as nonadiabatic molecular dynamics simulations can model the photorelaxation processes that occur upon excitation, allowing for the calculation of observables which can be compared directly with experimental data. For example, in TRPES, the kinetic energy of the photoelectrons is directly related to the binding energy of electrons in the molecule, which is influenced by the electronic state and geometry of the molecule at the time of ionisation. The binding energy can be calculated from the simulations at every time step, along with the ionisation probability, and hence, the predicted photoelectron signal can be computed to compare with experiment. This comparison helps to validate the theoretical methods in addition to explaining experimental observations and the underlying processes.

Nevertheless, it can be challenging to find a method that accurately describes the molecule while being sufficiently cheap computationally to perform the simulations and to calculate the observables, especially when the size of the molecule and duration of the dynamics increases. Therefore, a detailed investigation of the molecule being studied is required in order to arrive at a combination of an electronic structure model and dynamics method, which provide reasonably accurate simulations and, hence, observables, while remaining computationally feasible. This delicate trade-off will be discussed throughout the thesis for a subset of molecular systems of varying sizes.

1.4 Overview and aims of thesis

In Chapter 2, a brief description of the theory that will be used throughout this thesis will be given, including the fundamentals of quantum mechanics and its application to molecular systems. Furthermore, the chosen method to propagate the nonadiabatic dynamics simulations in this thesis will be detailed in addition to the different electronic structure methods mentioned throughout. Next, in Chapter 3, the photoinduced ring-conversion reaction of cyclopentadiene is modelled with accurate electronic structure calculations and nonadiabatic molecular dynamics simulations, in addition to investigating the reactions that occur on the hot ground state. To connect these theory simulations to UXS experiments, the time-dependent X-ray scattering signal is computed and compared to the experimental results. Chapter 4 explores the photorelaxation pathways in six azanaphthalene systems with quantum chemical calculations to rationalise lifetimes from recent TAS experiments in a systematic manner. Following on, Chapter 5 expands upon the previous chapter by performing nonadiabatic dynamics simulations for a subset of these azanaphthalenes to determine how closely the key features identified in the electronic structure relate to the actual dynamics. Moreover, the discrepancies observed in these simulations compared to experiment are also discussed. Finally, Chapter 6 explores the charge transfer dynamics occurring in N,N'-dimethylpiperazine (DMP) upon excitation into an electronic Rydberg state, resulting in large structural changes to the molecular geometry. Dynamics simulations are performed and directly related to previous experiments by computing the time-resolved photoelectron spectrum and X-ray scattering signals for the ensemble of trajectories. Due to the fact that computing the TRPES signal requires the ion states to be calculated, the DMP cation has also been investigated.

Together, these chapters use theoretical calculations to gain insights into important real-world systems. This is achieved through careful comparison of theoretical results with high-level computational methods and state-of-the-art experimental data. Overall, this thesis aims to show how modern theoretical and experimental approaches can be combined to fully understand the complex photochemistry of molecular systems, provide an example on how to study similar molecules and, finally, investigate in detail the photochemistry of three important systems.

2
Theory

2.1 Introduction

In this chapter, the theoretical framework that underpins the research in this thesis will be reviewed. The focus of this body of work is investigating the ultrafast dynamics in various molecules that occurs following photoexcitation. To simulate these photoexcited dynamics, approximations are necessary to model the nuclear and electronic wave packets, which will be discussed in detail. Additionally, to connect the theoretical simulations to experiment, relevant observables are computed where applicable, and hence, these methods will also be outlined. However, firstly the fundamental principles of quantum mechanics will be discussed, starting with the time-dependent Schrödinger equation.

2.2 Time-dependent Schrödinger equation

The time evolution of a molecular system is governed by the time-dependent Schrödinger equation (TDSE),

$$i\hbar\frac{\partial}{\partial t}\Psi(\mathbf{r},\mathbf{R},t) = \hat{H}(\mathbf{r},\mathbf{R})\Psi(\mathbf{r},\mathbf{R},t), \tag{2.1}$$

where i is the imaginary unit, $\hbar$ is the reduced Planck's constant, $\Psi(\mathbf{r},\mathbf{R},t)$ is the molecular wave function and $\hat{H}(\mathbf{r},\mathbf{R})$ is the molecular Hamiltonian, with $\mathbf{r}$ and

R referring to the vectors of the electronic and nuclear coordinates, respectively. Henceforth, atomic units will be used in this chapter, where e.g. $\hbar = 1$. The time-independent Schrödinger equation (TISE) can then be derived by the separation of variables technique and is given by,

$$\hat{H}\Psi(\mathbf{r},\mathbf{R}) = E\Psi(\mathbf{r},\mathbf{R}). \tag{2.2}$$

The time-independent molecular Hamiltonian, $\hat{H}(\mathbf{r},\mathbf{R})$, is described by the total kinetic and potential energies of the system, and is expressed in atomic units as,

$$\begin{aligned}\hat{H}(\mathbf{r},\mathbf{R}) &= -\sum_{A=1}^{M}\frac{1}{2M_A}\nabla_A^2 - \sum_{i=1}^{N}\frac{1}{2}\nabla_i^2 - \sum_{i=1}^{N}\sum_{A=1}^{M}\frac{Z_A}{r_{iA}} + \sum_{i=1}^{N}\sum_{j>i}^{N}\frac{1}{r_{ij}} + \sum_{A=1}^{M}\sum_{B>A}^{M}\frac{Z_A Z_B}{r_{AB}} \\ &= \hat{T}_N(\mathbf{R}) + \hat{T}_e(\mathbf{r}) + \hat{V}_{eN}(\mathbf{r},\mathbf{R}) + \hat{V}_{ee}(\mathbf{r}) + \hat{V}_{NN}(\mathbf{R}),\end{aligned} \tag{2.3}$$

where M_A is the mass of nucleus A, Z_A and Z_B are the charges on nuclei A and B, respectively, and r_{ij} is the distance between electrons i and j. Additionally, r_{AB} denotes the distance between nuclei A and B, while r_{iA} refers to the distance between electron i and nucleus A. The Hamiltonian consists of a kinetic energy term for the nuclei ($\hat{T}_N$) and electrons ($\hat{T}_e$), in addition to the Coulomb nucleus-electron ($\hat{V}_{eN}$), electron-electron ($\hat{V}_{ee}$) and nucleus-nucleus ($\hat{V}_{NN}$) interaction terms. Inserting the molecular Hamiltonian into Eq. 2.1 or 2.2 yields equations that do not have an analytical solution in general, and a combination of approximations and suitable numerical methods are required.

2.3 Born-Oppenheimer approximation

The Born-Oppenheimer approximation (BOA) is of fundamental importance in quantum chemistry and is based upon the fact that the nuclei are significantly heavier than the electrons, and hence, their velocities are considerably slower [33]. Therefore, in the BOA, nuclear and electronic motion are decoupled, allowing the electronic molecular Hamiltonian to be written in the form,

$$\begin{aligned}\hat{H}_{\mathrm{el}}(\mathbf{r};\mathbf{R}) &= -\sum_{i=1}^{N}\frac{1}{2}\nabla_i^2 - \sum_{i=1}^{N}\sum_{A=1}^{M}\frac{Z_A}{r_{iA}} + \sum_{i=1}^{N}\sum_{j>i}^{N}\frac{1}{r_{ij}} + \sum_{A=1}^{M}\sum_{B>A}^{M}\frac{Z_A Z_B}{r_{AB}} \\ &= \hat{T}_e(\mathbf{r}) + \hat{V}_{eN}(\mathbf{r},\mathbf{R}) + \hat{V}_{ee}(\mathbf{r}) + \hat{V}_{NN}(\mathbf{R}),\end{aligned} \tag{2.4}$$

where $\hat{H}_{\mathrm{el}}(\mathbf{r};\mathbf{R})$ now has a parametric dependence on the nuclear coordinates, $\mathbf{R}$. Therefore, for a fixed set of nuclear positions the electronic TISE can be solved using,

$$\hat{H}_{\mathrm{el}}(\mathbf{r},\mathbf{R})\psi_{\mathrm{el}}(\mathbf{r};\mathbf{R}) = E_{\mathrm{el}}(\mathbf{R})\psi_{\mathrm{el}}(\mathbf{r};\mathbf{R}), \tag{2.5}$$

which yields the electronic energy, $E_{\mathrm{el}}(\mathbf{R})$. Solving the electronic TISE for many nuclear positions obtains the adiabatic PES. Moreover, as the electronic and nuclear motion are decoupled in the BOA, the evolution of the time-dependent molecular wave function on different electronic states is uncoupled, and can be approximated by a product of the time-independent electronic wave functions, $\psi_i(\mathbf{r};\mathbf{R})$, and time-dependent nuclear wave functions, $\chi_i(\mathbf{R},t)$, given by,

$$\Psi(\mathbf{r},\mathbf{R},t) = \chi_i(\mathbf{R},t)\psi_i(\mathbf{r};\mathbf{R}), \tag{2.6}$$

where i is the electronic state of interest. Therefore, in the BOA framework, the system evolves on one adiabatic PES. This approximation remains valid when the electronic states are well separated. However, in regions where the electronic states come close together, the nonadiabatic coupling between the electronic states and nuclear motion becomes significant, and therefore the BOA breaks down due to the exclusion of these effects. Hence, in order to describe the nonadiabatic effects in these regions and the evolution of the system on more than one adiabatic PES, the Born-Huang expansion is necessary.

2.4 Nonadiabatic couplings

The Born-Huang expansion [34] is an exact ansatz in which the molecular wave function is written as a linear combination of the adiabatic wave functions, $\psi_i(\mathbf{r};\mathbf{R})$, in the form,

$$\Psi(\mathbf{r},\mathbf{R},t) = \sum_i^{\infty} \chi_i(\mathbf{R},t)\psi_i(\mathbf{r};\mathbf{R}) \tag{2.7}$$

where $\chi_i(\mathbf{R},t)$ are the time-dependent coefficients, also known as the nuclear wave functions, for each electronic state $\psi_i(\mathbf{r};\mathbf{R})$. Formally, the sum runs over all electronic states i, but in practice, the sum is always truncated. Inserting this expansion into Eq. 2.1 obtains,

$$i\frac{\partial}{\partial t}\chi_j(\mathbf{R},t) = \left[\hat{T}_N(\mathbf{R}) + E_j(\mathbf{R})\right]\chi_j(\mathbf{R},t) - \sum_A \frac{1}{2M_A}\sum_i \Lambda_{ij}\chi_i(\mathbf{R},t) \tag{2.8}$$

where,

$$\Lambda_{ij} = \left\langle \psi_i|\nabla_A^2|\psi_j\right\rangle_r + 2\cdot\left\langle \psi_i|\nabla_A|\psi_j\right\rangle_r \cdot \nabla_A. \tag{2.9}$$

The first two terms in the square-brackets in Eq. 2.8, describe the evolution of the nuclear wave function on a particular electronic state, where the time-independent PES arises from the $E_j(\mathbf{R})$ term. Additionally, Λ_{ij} introduces the couplings between nuclear wave functions evolving on different electronic states through the derivative and scalar couplings, $\mathbf{d}_{ij}^A$ and D_{ij}^A, respectively, where their matrix elements are defined as,

$$\mathbf{d}_{ij}^A(\mathbf{R}) = \left\langle \psi_i|\nabla_A|\psi_j\right\rangle_r, \tag{2.10}$$

and

$$D_{ij}^A(\mathbf{R}) = \left\langle \psi_i|\nabla_A^2|\psi_j\right\rangle_r. \tag{2.11}$$

These nonadiabatic coupling terms originate from the nuclear kinetic energy operator, $\hat{T}_N$, acting on the electronic wave functions, ψ_i. When the electronic states are well separated, the coupling terms in Eq. 2.9 can be neglected, simplifying the equation to,

$$i\hbar\frac{\partial}{\partial t}\chi_j(\mathbf{R},t) \approx [\hat{T}_N + E_j(R)]\chi_j(\mathbf{R},t), \tag{2.12}$$

when D_{jj}^A is also ignored, which is a valid approximation as these diagonal elements are typically small. This constrains the nuclear wave function to a single electronic state and also decouples nuclear and electronic motion, recovering the BOA. Thus, nonadiabatic couplings can be seen as a mechanism that enables the transition between adiabatic states. Furthermore, the scalar coupling is normally negligible compared to the derivative or nonadiabatic coupling and hence, is often ignored when computing the couplings.

Alternatively, the derivative coupling $\mathbf{d}_{ij}^{A}$ can be written in the form [35],

$$\mathbf{d}_{ij}^{A} = \frac{\langle \psi_i | \nabla \hat{H}_{\text{el}} | \psi_j \rangle}{E_j - E_i}, \tag{2.13}$$

which clearly demonstrates the correlation between the size of the coupling and the energy gap between the electronic states. As the separation between states increases, the coupling becomes negligible, but when the states become degenerate, the coupling approaches infinity.

It is important to note that the nonadiabatic coupling terms are defined within the adiabatic representation, where the electronic Hamiltonian is diagonal, and the off-diagonal elements of the nuclear kinetic energy operator correspond to the nonadiabatic coupling terms between states. In contrast, in the diabatic representation, the nuclear kinetic energy operator is diagonal, eliminating these nonadiabatic coupling terms. Instead, the coupling terms appear as off-diagonal elements in the electronic Hamiltonian. Since the diabatic representation is challenging to define for all systems, the adiabatic representation is generally preferred for mixed quantum-classical dynamics.

2.5 Conical Intersections

In systems with more than one degree of freedom, two adiabatic states of the same multiplicity can become degenerate, known as a conical intersection (CI) [35–37]. These intersections often play a dominant role in the internal conversion of polyatomic molecules, mediating the nonadiabatic transitions between different electronic states. CIs exist within a seam space, where degeneracy is preserved and the local minimum within this space is known as a minimum energy conical intersection (MECI). There are two coordinates that lift the degeneracy, namely the $\mathbf{g}$ and $\mathbf{h}$ vectors, which are given by,

$$\mathbf{g} = \frac{1}{2}(\langle \psi_i(\mathbf{r};\mathbf{R}) | \nabla \hat{H}_{\text{el}}(\mathbf{r};\mathbf{R}) | \psi_i(\mathbf{r};\mathbf{R}) \rangle - \langle \psi_j(\mathbf{r};\mathbf{R}) | \nabla \hat{H}_{\text{el}}(\mathbf{r};\mathbf{R}) | \psi_j(\mathbf{r};\mathbf{R}) \rangle), \tag{2.14}$$

and

$$\mathbf{h} = \langle \psi_i(\mathbf{r};\mathbf{R}) | \nabla \hat{H}_{\text{el}}(\mathbf{r};\mathbf{R}) | \psi_j(\mathbf{r};\mathbf{R}) \rangle. \tag{2.15}$$

The **g** vector corresponds to the energy difference gradient, whereas the **h** vector is defined as the nonadiabatic coupling and this two dimensional subspace that lifts the degeneracy is known as branching plane [38].

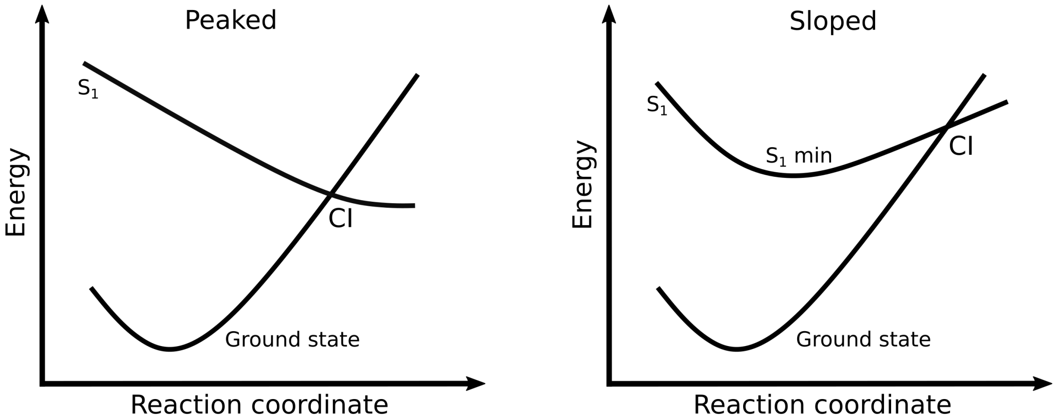

Figure 2.1: Schematic example of a peaked and sloped conical intersection (CI) between the electronic ground state and the first excited singlet state.

Moreover, CIs are primarily classified into two topographies: peaked and sloped, which can significantly influence the rate of nonadiabatic transfer from the upper state to the lower state [35, 36]. A schematic example of a peaked and sloped CI between the electronic ground state and first excited singlet state is depicted in Fig. 2.1. Peaked CIs correspond to a barrierless transition, enabling efficient internal conversion to the lower state. In contrast, sloped CIs are located near the minimum of the upper state. As a result, the system often reaches this minimum before undergoing internal conversion to the lower lying state, leading to less efficient population transfer. Therefore, understanding the topographies is essential for predicting the overall photochemistry of a molecule.

2.6 Intersystem Crossing

In addition to nonradiative transitions between electronic states of the same multiplicity, these transitions can also occur between electronic states of different spin multiplicities, a process known as intersystem crossing (ISC) [39, 40]. Since

ISC requires a change in spin multiplicity, it is a formally forbidden process in a non-relativistic framework, however, spin-orbit coupling (SOC), which is a relativistic effect, can facilitate this process [39]. Thus, SOC plays an important role in photochemistry by enabling access to longer-lived triplet states, and introducing new photorelaxation pathways that may not be present in the singlet manifold.

SOC arises from the interaction between an electron's spin and orbital angular momentum. This interaction gives rise to mixing of the orbital and spin degrees of freedom, allowing coupling between electronic states of different spin multiplicities. The SOC is most widely computed with the Breit-Pauli Hamiltonian defined as,

$$\hat{H}_{\mathrm{SOC}} = \frac{1}{2c^2}\left[\sum_i \sum_A \frac{Z_A}{r_{iA}^3}\left(\hat{\mathbf{r}}_{iA} \times \hat{\mathbf{p}}_i\right) \cdot \hat{\mathbf{s}}_i - \sum_i \sum_{j \neq i} \frac{1}{r_{ij}^3}\left(\hat{\mathbf{r}}_{ij} \times \hat{\mathbf{p}}_i\right) \cdot \left(\hat{\mathbf{s}}_i + 2\hat{\mathbf{s}}_j\right)\right], \tag{2.16}$$

where c is the speed of light, $\hat{\mathbf{r}}_{iA} \times \hat{\mathbf{p}}_i$ is the angular momentum of electron i with respect to nucleus A, $\hat{\mathbf{r}}_{ij} \times \hat{\mathbf{p}}_i$ is the angular momentum of electron i with respect to electron j and the $\hat{\mathbf{s}}_i$ is the spin-operator of electron i. The first term in Eq. 2.16, describes the interaction between the spin magnetic moment of an electron i with the magnetic moment arising from its orbiting in the field of nucleus A. Therefore, the SOC is dependent on the nuclear charge Z_A, where a higher nuclear charge leads to larger SOC and, hence, it becomes more important in molecules with heavier atoms.

The second term is composed of a spin-same-orbit coupling term and a spin-other-orbit coupling term, where the spin-same-orbit coupling term is analogous to the first term, however, the field is generated by the motion of electron j. The spin-other-orbit term arises from the coupling between the spin magnetic moment of electron j and the orbital magnetic moment of electron i and vice versa [39]. Using this SOC Hamiltonian, the spin-orbit coupling matrix elements (SOCMEs) between two states are calculated as,

$$[\hat{H}_{\mathrm{SOC}}]_{ij} = \langle \psi_i | \hat{H}_{\mathrm{SOC}} | \psi_j \rangle, \tag{2.17}$$

where i and j are two electronic states with different spin multiplicities. From Eq. 2.17, it is clear that the magnitude of the SOC and hence, the rate of ISC, is dependent on the character of states involved in the electronic transition. The relation between the nature of this transition and the rate of ISC has been described qualitatively by El-Sayed's rules [41], which state that the total angular momentum must be conserved in order to achieve large SOC, and therefore a change of spin must be accompanied by a corresponding change in the angular momentum. Thus, the El-Sayed rules predict that the rate of ISC would be faster for e.g. a $^1\pi\pi^* \rightsquigarrow {}^3n\pi^*$ transition compared to a $^1\pi\pi^* \rightsquigarrow {}^3\pi\pi^*$ transition, as a consequence of the latter transition involving the same orbitals and hence, the total angular momentum is not conserved as there is no change in angular momentum for this transition.

2.7 Nonadiabatic molecular dynamics

As previously discussed in Section 2.3, the solution to the TDSE requires knowledge of the electronic energies $E(\mathbf{R})$, and the two nonadiabatic coupling terms, $\mathbf{d}_{ij}^{A}(\mathbf{R})$ and $D_{ij}^{A}(\mathbf{R})$, between all of the electronic states considered. Therefore, in most cases a fully quantum treatment of both the nuclei and electrons is limited to smaller systems. For example, grid-based approaches such as multiconfigurational time-dependent Hartree (MCTDH) [42], are only feasible for molecules with a few degrees of freedom as pre-computed PESs of N-dimensions are required to propagate the nuclear amplitudes. This procedure scales exponentially with the number of degrees of freedom and hence, for larger molecules these methods are unfeasible and approximations must be made.

In contrast, trajectory based methods are commonly used to compute the nonadiabatic dynamics in larger molecules, where an ensemble of trajectories are propagated and the PESs are calculated 'on-the-fly' during the dynamics. There are several trajectory based methods, for example, Ehrenfest [43] and surface-hopping [44, 45], which are termed mixed quantum-classical methods, where the nuclei are propagated classically and the electrons are propagated with quantum methods. Additionally, methods such as multiconfigurational Ehrenfest (MCE) [46] and *ab initio* multiple spawning (AIMS) [47] are known as semi-classical methods due to the incorporation of quantum nuclear effects. These methods are more computationally unfavourable and hence, will not be discussed further. In this thesis, trajectory surface hopping will be employed for the calculation of the nonadiabatic molecular dynamics, and will be discussed in more detail next.

2.7.1 Trajectory surface hopping

In trajectory surface hopping (TSH), the nuclei are propagated classically on a single adiabatic surface, analogous to Born-Oppenheimer molecular dynamics (BOMD). However, unlike BOMD, where the system remains on one adiabatic PES throughout the simulations, TSH incorporates the ability to switch states allowing it to effectively describe photochemical processes, which is demonstrated in Fig. 2.2. TSH introduces nonadiabatic effects through a stochastic algorithm that enables the transfer of population between electronic states during the dynamics. Moreover, in TSH, an ensemble of independent trajectories are used to represent the spread of a nuclear wave packet [45].

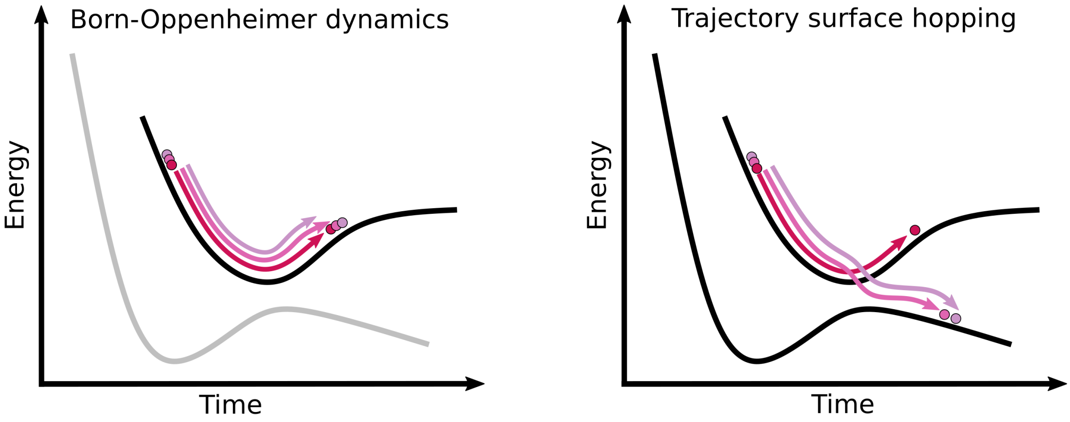

Figure 2.2: A schematic of Born-Oppenheimer dynamics and trajectory surface hopping. In the Born-Oppenheimer picture, the dynamics are constrained to a single adiabatic state, whereas a stochastic algorithm in surface hopping allows population transfer to other states.

Within TSH, the nuclei are propagated classically according to Newton's equations of motion:

$$M_A \frac{\partial^2 \mathbf{R}_A}{\partial t^2} = -\frac{\partial E_{\mathrm{el}}^{\lambda}}{\partial \mathbf{R}_A}, \tag{2.18}$$

where M_A is the mass of nucleus A, $\mathbf{R}_A$ is the position of nucleus A and finally, E_{el} is the electronic energy of the current electronic state, λ. The velocity-Verlet algorithm [48] is usually employed to integrate Eq. 2.18. Additionally, the total electronic wave function can be expanded by,

$$\Psi_{\mathrm{el}}(\mathbf{r}, \mathbf{R}, t) = \sum_i c_i(t)\psi_i(\mathbf{r}; \mathbf{R}), \tag{2.19}$$

where $c_i(t)$ are the time-dependent expansion coefficients, which correspond to the electronic wave function $\psi_i(\mathbf{r}; \mathbf{R})$, summing over i basis states. Substituting this into the TDSE leads to the equation of motion for the electrons:

$$\frac{\partial c_j}{\partial t} = -\sum_i \left[\frac{i}{\hbar} H_{ji} + K_{ji}\right] c_i, \tag{2.20}$$

where H_{ji} is the matrix element of the electronic Hamiltonian given by,

$$H_{ji} = \langle \psi_j | H_{\mathrm{el}} | \psi_i \rangle_r. \tag{2.21}$$

The electronic Hamiltonian in Eq. 2.4 can be used in systems where only singlet states need to be calculated. However, as established in Section 2.6, ISC is important in many molecules, which have significant SOC, and hence, an additional term for SOC must be included, leading to the total electronic Hamiltonian [49],

$$\hat{H}^{\mathrm{tot}}_{\mathrm{el}} = \hat{H}_{\mathrm{el}} + \hat{H}_{\mathrm{SOC}}. \tag{2.22}$$

Inserting this into Eq. 2.21 results in a non-diagonal Hamiltonian matrix, however, employing a unitary transformation, as implemented in SHARC [50], yields a diagonal total Hamiltonian matrix known as the diagonal representation [49]. The diagonal representation mixes states of different multiplicities due to SOC. This concept is illustrated in Fig. 2.3, which highlights the differences between adiabatic and diagonal states. In the adiabatic representation, the states are unaffected by SOC, resulting in two singlet states and one triplet state in the figure. However, when transformed into the diagonal representation, the states mix, and are labelled with numerical ordering based on energy. SOC also lifts the degeneracy of the triplet state, leading to a total of five states.

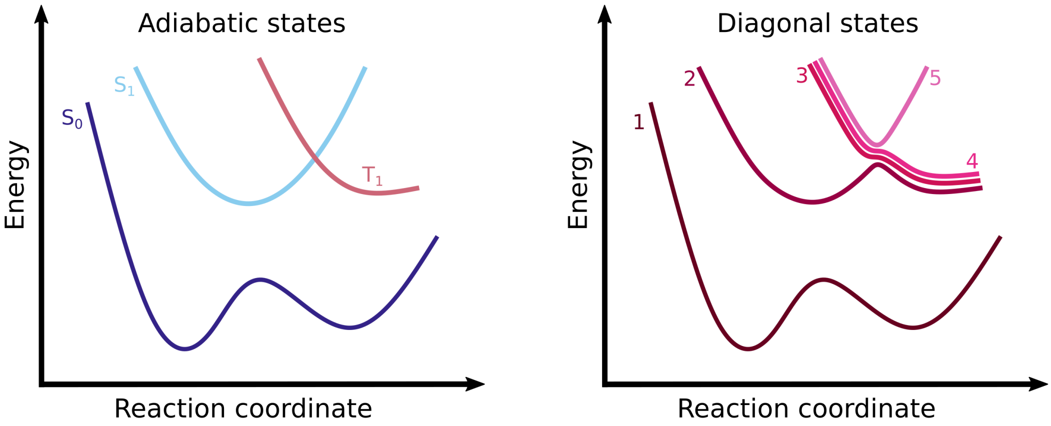

Figure 2.3: Difference between states in the adiabatic and diagonal representation. Here, two singlet states and one triplet state are shown in the adiabatic representation. Transforming these states into the diagonal representation leads to mixing of states and the triplet degeneracy is lifted.

Returning to Eq. 2.20, K_{ji} can be calculated as the dot product of the nuclear velocity vector and the nonadiabatic coupling vector between the two states j and i, which is expressed as,

$$K_{ji} = \mathbf{v} \cdot \langle \psi_j | \nabla | \psi_i \rangle_r. \tag{2.23}$$

Therefore, K_{ji} can be calculated utilising the nonadiabatic coupling vectors, however, these are often unavailable and hence, the wave function overlap method can be employed as an approximation to calculate K_{ji} using [51, 52],

$$K_{ji}\left(t + \frac{\Delta t}{2}\right) \approx \frac{1}{2\Delta t}(S_{ji}(t, t+\Delta t) - S_{ji}(t+\Delta t, t)), \tag{2.24}$$

where the overlaps S_{ji} are defined as,

$$S_{ji}(t, t+\Delta t) = \langle \psi_j(t) | \psi_i(t+\Delta t) \rangle. \tag{2.25}$$

Furthermore, the probability of transitioning between the current electronic state j and another electronic state i is evaluated at every time step in the dynamics; the most common method to compute this is Tully's fewest switches algorithm [53], which minimises the number of hopping events in one time step, Δt. The hopping probability from state j to state i is calculated with,

$$P_{j \to i} = max\left[0, -\frac{2\Delta t}{\rho_{ii}} \Re(\rho_{ij} K_{ji})\right], \tag{2.26}$$

where the electronic density matrix ρ_{ij} is,

$$\rho_{ij}(t) = c_i(t)c_j^*(t). \tag{2.27}$$

Once the hopping probability is calculated, a random number, r, is generated in the [0,1] interval and a hop will occur if the following condition is satisfied:

$$\sum_{n=1}^{i-1} P_{j\to n}(t) < r_t \leq \sum_{n=1}^{i} P_{j\to n}(t). \tag{2.28}$$

If a hop occurs, the kinetic energy of the nuclei is adjusted in order to conserve the total energy, as the new active state will have a different potential energy compared to the previous state. For transitions from a lower state to a higher-lying one, if the energy available to rescale the kinetic energy is less than the difference between these two states, then the hop is rejected and this is known as a frustrated hop [53].

2.7.1.1 Decoherence

TSH suffers from the ‘overcoherence’ problem, where the electronic populations are propagated with too much coherence, which arises from the fact that the electronic amplitudes for the different states are forced to evolve along the active state in the trajectory. Therefore, this does not take into consideration that after a nonadiabatic transition, the electronic states will have different gradients, which in reality would lead to the amplitudes on the non-active state dissipating over time.

There are multiple schemes that can correct for this issue, however, the most commonly used is Granucci and Persico’s energy-based decoherence scheme [54, 55]. This scheme uses a damping factor of $e^{\Delta t/\tau_{ij}}$ for the populations of all states, $c_j(t)$, other than the active state $c_i(t)$, with,

$$\tau_{ij} = \frac{\hbar}{|E_i - E_j|}\left(1 + \frac{C}{E_{\mathrm{KE}}}\right), \tag{2.29}$$

where C is the decoherence parameter, which has a value of 0.1 Hartree. Once, the populations are damped, this change in population for states j is added to the current state i.

2.7.2 Initial conditions

As mentioned previously, the nature of a wave packet is depicted by an ensemble of independent trajectories in TSH. The classical propagation of these trajectories requires both initial positions and momenta, which are extracted from the wave function using the Wigner distribution [56, 57], given by,

$$W(q,p) = \frac{1}{\pi}\int_{-\infty}^{\infty} dq'\psi^*(q-q')\psi(q+q')\exp(-2iq'p), \tag{2.30}$$

where q and p are the positions and momenta, respectively. In a molecular system, the ground state is modelled as a set of uncoupled harmonic oscillators for all vibrational normal modes and, hence, is only reliable in systems where this is a good approximation. Sampling the Wigner distribution for all vibrational normal modes gives position and momentum distributions of the nuclei for each of the individual points in phase-space. The more individual points sampled, the better the representation of the original wave function [56, 57].

Once the initial conditions are acquired, specific excitation conditions based on the excitation energies and oscillator strengths may be applied to obtain a restricted set of initial conditions for the dynamics simulations. In a given excitation range, the maximum $p_{k,\alpha}$ value of

$$p_{k,\alpha} = \frac{f^{\text{osc}}_{k,\alpha}}{E^2_{k,\alpha}} \tag{2.31}$$

is calculated, where $f^{\text{osc}}_{k,\alpha}$ and $E_{k,\alpha}$ is the oscillator strength and excitation energy, respectively, of initial condition k and excited state α. A random number is then produced in the range of [0,1] for each excited state and if

$$r_{k,\alpha} < \frac{p_{k,\alpha}}{p_{\text{max}}}, \tag{2.32}$$

then the excited state for a particular initial condition is selected for the dynamics simulations. This excited state selection scheme, as implemented in SHARC [58], allows for direct comparison with experiment, as the nonadiabatic dynamics simulations can be performed with a good model of the experimental pulse.

Additionally, by obtaining initial conditions from the Wigner distribution, it is possible to approximate the absorption spectrum, which is discussed in further detail in Appendix A.

2.8 Electronic structure theory

In order to determine the energies and gradients of the electronic states as well as the nonadiabatic couplings between states, an electronic structure method is required. Electronic structure methods compute wave functions by invoking approximations for solving the TISE in Eq. 2.2, and hence, the aforementioned quantities can be calculated. Obtaining accurate energies and gradients is key for producing quality simulations as it has been shown that the dynamics are more dependent on the electronic structure compared to the dynamics method of choice [59]. There are a variety of electronic structure methods, and the ones encountered later in this thesis will be detailed here, however, a brief description of Hartree-Fock theory will be given first, to aid explanation of the other methods.

2.8.1 Hartree-Fock theory

Hartree-Fock (HF) theory [60] is the simplest acceptable *ab initio* approach in which, the wave function is written as a single Slater determinant of one-particle orbitals,

$$\Psi_{\mathrm{HF}}(\mathbf{x}_1, \mathbf{x}_2, \ldots, \mathbf{x}_N) = \frac{1}{\sqrt{N!}} \begin{vmatrix} \phi_1(\mathbf{x}_1) & \phi_2(\mathbf{x}_1) & \ldots & \phi_n(\mathbf{x}_1) \\ \phi_1(\mathbf{x}_2) & \phi_2(\mathbf{x}_2) & \ldots & \phi_n(\mathbf{x}_2) \\ \vdots & \vdots & \ddots & \vdots \\ \phi_1(\mathbf{x}_N) & \phi_2(\mathbf{x}_N) & \ldots & \phi_n(\mathbf{x}_N) \end{vmatrix}, \tag{2.33}$$

where $\phi_i(\mathbf{x}_j)$ denotes a spin orbital i for an electron j with coordinates $\mathbf{x}_j$. This fulfills the requirement that the wave function is antisymmetric, satisfying Pauli's exclusion principle. The Fock operator acts on each of these spin orbitals,

$$\hat{f}_i \phi_i = \epsilon_i \phi_i, \tag{2.34}$$

which derives the HF equations, with the one-electron Fock operator ($\hat{f}_i$) given by,

$$\hat{f}_i = -\frac{1}{2}\nabla_i^2 - \sum_A \frac{Z_A}{r_{iA}} + v_i^{\mathrm{HF}}, \tag{2.35}$$

where the electron-electron repulsion term is treated in a mean field way using the HF potential υ_i^{HF}, which depends on the other spin orbitals. A self-consistent field (SCF) method is used to solve the HF equations by minimising the total HF energy E_{HF} according to the variational principle.

The HF method suffers from several deficiencies, with the first being a lack of electron correlation, of which there are two types: static and dynamic. Static correlation arises when a single electronic configuration is insufficient to describe the molecule, while dynamic correlation is due to the instantaneous repulsion between electrons. As a consequence of using a single Slater determinant, HF does not capture static correlation and dynamic correlation is also not accounted for due to the use of a mean field approach. Therefore, the electron correlation energy, E_{corr}, in a system is often defined as,

$$E_{\text{corr}} = E_{\text{exact}} - E_{\text{HF}}, \tag{2.36}$$

which is the difference between the exact energy, E_{exact}, and the HF energy, E_{HF}. Additionally, this method can only calculate the ground state and is unable to describe multiconfigurational regions of the PES, for example where the ground and excited states become degenerate. Thus, higher level methods are necessary for the calculations of ground and excited states.

2.8.2 Complete active space self-consistent field theory

As mentioned in the previous section, HF has shortcomings as a consequence of using a single Slater determinant, which can be improved upon by including excited state Slater determinants in the wave function. In contrast to HF, full configuration interaction (FCI) describes the wave function as a linear combination of Slater determinants, which can be written as:

$$\Psi = c_0\Psi_0 + \sum_{a,r} c_a^r \Psi_a^r + \sum_{\substack{a<b\\ r<s}} c_{ab}^{rs}\Psi_{ab}^{rs} + \sum_{\substack{a<b<c\\ r<s<t}} c_{abc}^{rst}\Psi_{abc}^{rst} + \ldots, \tag{2.37}$$

where c represents the expansion coefficients that are varied in the configuration interaction procedure with the molecular orbitals fixed. Moreover, the first term corresponds to the ground state determinant (Ψ_0), while the second and third terms sum over all singly (Ψ_a^r) and doubly (Ψ_{ab}^{rs}) excited determinants, respectively, and so on. FCI provides the exact solution within a given basis set, however, this method is extremely computationally expensive and is often truncated to include only single excitations (CIS) or single and double excitations (CISD).

Alternatively, both the expansion coefficients and the molecular orbitals can be optimised, which is the principle of multiconfigurational self-consistent field (MCSCF) theory. In particular, one popular approach is complete active space self-consistent field (CASSCF) theory [61–63], which involves splitting the orbitals into three subspaces: inactive, active and virtual (a schematic is shown in Fig. 2.4). The inactive orbitals are fully occupied whereas the virtual orbitals are unoccupied, and both of these subspaces are not included in the configuration interaction calculation. The active orbitals form a subspace, known as the active space, where electron correlation is treated by performing a FCI calculation inside this space. Therefore, the CASSCF wave function is given by,

$$\Psi_{\mathrm{CASSCF}} = \sum_i c_i \Phi_i, \tag{2.38}$$

where c_i are the expansion coefficients and Φ_i are the determinants describing a particular configuration inside the active space. Both expansion coefficients *and* orbitals are then varied to minimise the energy. This procedure can be extended to include excited states by averaging over a certain number of states, which is known as state-averaged CASSCF (SA-CASSCF).

Selecting an active space for the CASSCF calculations is non-trivial and involves choosing a specific number of electrons and orbitals, denoted by (n,m), where n is the number of electrons and m is the number of orbitals. For instance, a $(4,4)$ active space is shown in Fig. 2.4, where all possible configurations within the active space contribute to the CASSCF wave function. The active space must accurately capture all regions of the PES that may be explored during dynamics simulations for all relevant electronic states. If the orbitals in the active space fail to represent a particular region correctly, the CASSCF calculations will be inaccurate

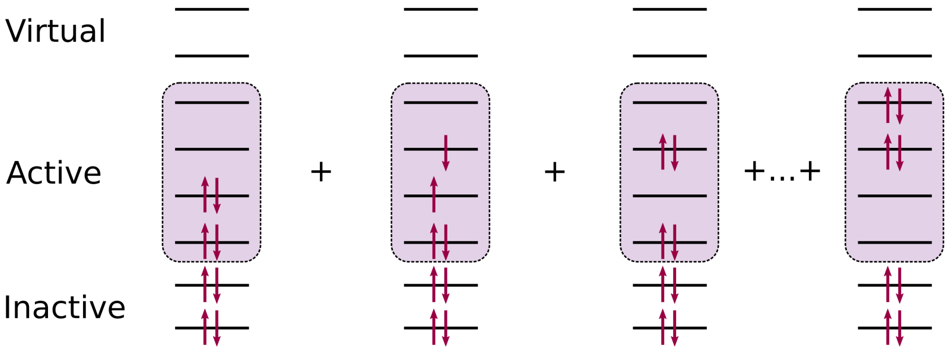

Figure 2.4: Schematic diagram depicting a (4,4) active space, composed of four electrons in four orbitals.

for that region. A common issue in dynamics simulations arises when the active space fails to describe a region correctly, leading to the rotation of orbitals and their replacement with a different set, which in turn causes stability issues and an unphysical description of the dynamics. As a result, choosing an active space often involves extensive testing, and since CASSCF scales exponentially with the number of orbitals, there is typically a trade-off between accuracy and computational cost.

Due to the wave function considering different electronic configurations inside the active space, CASSCF accounts for static correlation and hence, can describe regions where the ground state is highly multiconfigurational, such as at CIs between the first excited state and the ground state. Nevertheless, the limitation of this method is the lack of dynamic correlation, as the virtual orbitals are not included in the configuration interaction procedure. Therefore, this can lead to issues such as incorrect ordering of excited states and overestimation of vertical excitation energies [64, 65], however, there are methods that improve upon CASSCF, which will be discussed next.

2.8.3 Complete active space second-order perturbation theory

Complete active space second-order perturbation theory (CASPT2) [66–68] is a multireference method, which is a correction to the CASSCF wave function. In CASPT2, second-order Rayleigh-Schrödinger perturbation theory is applied to the

CASSCF wave function, incorporating dynamic correlation by treating interactions with virtual orbitals as perturbative corrections. An additional improvement in systems where multiple electronic states are calculated is to use multi-state (MS) [69] and extended multi-state (XMS) CASPT2 [70]. MS-CASPT2 is known to produce accurate vertical excitation energies, however, it often has issues in other areas of the PES, especially around CIs. In contrast, XMS-CASPT2 resolves the instabilities around CIs [71], however, the vertical excitation energies are usually less accurate. Furthermore, XMS-CASPT2, is more sensitive to the number of electronic states included in the calculation due to the use of one Fock operator for all states, whereas in MS-CASPT2 there is a state-specific Fock operator in the formulation of the zeroth-order Hamiltonian. Nevertheless, XMS-CASPT2 is typically chosen for calculations of excited state PESs and in dynamics simulations when appropriate.

XMS-CASPT2 can produce very accurate energies and PESs, however, in a similar manner to CASSCF, it is still heavily dependent on the choice of active space. Another problem with this method is the presence of intruder states, which arise from configurations not included in the reference space but have energies close to the reference state. Therefore, the energy denominator in the second-order perturbation theory approaches zero causing large perturbation corrections. To correct for this issue, a real or imaginary shift can be applied to the zeroth-order Hamiltonian, which shifts these intruder states by a constant amount and does not significantly affect the results [72, 73]. Finally, XMS-CASPT2 is computationally demanding, particularly in larger systems, which require larger active spaces and a large number of states. Therefore, it is often unfeasible to use this method for dynamics simulations apart from in small molecules with moderate active spaces. Thus, XMS-CASPT2 is typically used as a benchmark for less expensive methods, which can be used to compute the dynamics.

2.8.4 Algebraic diagrammatic construction scheme

Defining active spaces that accurately describe the entire PES while remaining computationally feasible for the nonadiabatic dynamics simulations is often challenging.

Consequently, single-reference methods, which use a single electronic configuration as a reference to construct the excited states, are frequently required. These methods are generally effective in systems without significant static correlation, where the ground state is predominantly comprised of a single electronic configuration and is well separated from the excited states. A widely used single-reference method for excited state calculations is the algebraic diagrammatic construction to the second order (ADC(2)) method [74, 75]. ADC(2) is a linear response method based on a MP2 ground state wave function, which calculates correlated excited states by applying excitation operators to obtain excitation energies. Only singly excited states can be described by second order perturbation theory and hence, ADC(2) is unsuitable for systems where doubly excited states play an important role.

Moreover, ADC(2) has been shown to perform well in many systems and is stable in TSH dynamics simulations [76]. However, this method cannot accurately describe regions around S_1/S_0 CIs [77], and as a result, cannot be used to propagate dynamics through these CI regions onto the ground state. Nevertheless, there are some strategies to address this limitation, such as terminating the dynamics on the excited state or inducing a hop to the ground state just before reaching the CI [76, 78]. The former approach allows for identifying photorelaxation pathways, though it does not provide insight into the formation of photoproducts. The latter approach enables the determination of potential photoproducts, but the outcome is highly sensitive to the timing of the hop, which can significantly influence the dynamics and the resulting photoproduct formation. Moreover, in some cases, forcing a hop may not be viable, as the molecule may still pass through the CI region on the ground state. Despite these challenges, ADC(2) has been shown to correctly identify photorelaxation mechanisms in dynamics simulations, though it may overestimate the rate of nonradiative decay [59, 76].

Finally, the accuracy of ADC(2) can be improved by using spin-component scaling (SCS), which originates from MP2 [79]. In SCS, separate scaling factors are applied to the same-spin (c_{ss}) and opposite-spin (c_{os}) components of the correlation energy, with $c_{ss} = 1/3$ and $c_{os} = 6/5$. This adjustment generally improves the accuracy of SCS-ADC(2) over standard ADC(2), particularly in the calculation of excitation energies in the FC region and along PESs. Additionally, SCS-ADC(2) significantly reduces the discrepancies in error between valence and Rydberg states [80], similar to what is observed with the CC2 method, which will be discussed in the following section [81, 82].

2.8.5 Coupled cluster methods

Coupled cluster (CC) methods are another class of highly accurate methods, which do not require the use of an active space. In the CC approach, a cluster operator $\hat{T}$ is applied exponentially to a reference wave function,

$$\Psi_{\mathrm{CC}} = \mathrm{e}^{\hat{T}}\Psi_{\mathrm{HF}} \tag{2.39}$$

where Ψ_{HF} is the HF wave function and $\hat{T}$ includes all possible excitations from the references state, such that

$$\hat{T} = \hat{T}_1 + \hat{T}_2 + \hat{T}_3 + \dots, \tag{2.40}$$

where $\hat{T}_1$, $\hat{T}_2$ and $\hat{T}_3$ are the cluster operators for single, double and triple excitations, respectively. Similar to FCI, including all excitations in CC is unfeasible and hence, the CC methods are truncated, where only including $\hat{T}_1$ yields CC singles (CCS), whereas including both $\hat{T}_1$ and $\hat{T}_2$ gives CC singles and doubles (CCSD). However, CCSD is still often unachievable, and therefore, to reduce computational effort the $\hat{T}_2$ cluster operator can be approximated with second-order perturbation theory, giving the CC2 method [83].

Excited states can be computed with these methods either using a linear response [83] or equations of motion approach [84]. Exploration of excited state PESs is more advantageous with CC2 as it is a more affordable method compared to CCSD. Nevertheless, CCSD is often used for highly accurate benchmarking in molecular systems [85]. Analogous to ADC(2), CC2 cannot describe regions of the PES with a multiconfigurational ground state, as a consequence of being a single-reference method. Moreover, CC2 has been shown to be unstable in TSH simulations, where degeneracies between states are observed, due to numerical instabilities, and hence, ADC(2) is the favourable electronic structure method in dynamics simulations [59, 76]. However, CC2 is known to give more accurate vertical excitation energies, especially the SCS variant [80]. Nevertheless, in this thesis, a case is presented where the excited state dynamics are carried out using CC2, as the focus is solely on the evolution of the molecule on a single excited state, without the involvement of other excited states.

2.8.6 Density functional theory

The final electronic structure method discussed in this section, is density functional theory (DFT) [86], which is an alternative to all methods previously discussed known as *ab initio* methods. In DFT, the electron density $\rho(\mathbf{r})$ describes the distribution of the electrons in a system and can be obtained from the wave function $\Psi(\mathbf{r}_1, \mathbf{r}_2, \ldots, \mathbf{r}_N)$ by,

$$\rho(\mathbf{r}) = N \int dr_2 \cdots \int dr_N \Psi^*(\mathbf{r}, \mathbf{r}_2, \ldots, \mathbf{r}_N)\Psi(\mathbf{r}, \mathbf{r}_2, \ldots, \mathbf{r}_N), \tag{2.41}$$

where $\mathbf{r}_1, \mathbf{r}_2, \ldots, \mathbf{r}_N$ are the coordinates of N electrons. In a reference system of non-interacting electrons [87], the total energy of the system is expressed as,

$$E[\rho] = \int d\mathbf{r}\rho(\mathbf{r})\upsilon_{\text{ext}}(\mathbf{r}) + T_{\text{s}}[\rho] + J[\rho] + E_{\text{xc}}[\rho] \tag{2.42}$$

where υ_{ext} is the external potential, corresponding to the interaction between the electrons and nuclei, $T_{\text{s}}[\rho]$ is the kinetic energy, $J[\rho]$ denotes the Coulomb repulsion energy and finally $E_{\text{xc}}[\rho]$ is the exchange-correlation energy. The exact form of the exchange-correlation energy $E_{\text{xc}}[\rho]$ is unknown and must be approximated. There are three main approaches to calculate this energy, with the first known as the local density approximation (LDA) [87], which assumes that the exchange-correlation energy density $\epsilon_{\text{xc}}(\rho(\mathbf{r}))$ at a point depends only on the local electron density and the functional is given by,

$$E_{\text{xc}}^{\text{LDA}}[\rho] = \int \rho(\mathbf{r})\epsilon_{\text{xc}}^{\text{LDA}}(\rho(\mathbf{r}))d\mathbf{r}, \tag{2.43}$$

where $\epsilon_{\mathrm{xc}}^{\mathrm{LDA}}(\rho(\mathbf{r}))$ is the exchange-correlation energy density of a uniform electron gas and can be decomposed into constituents of exchange ϵ_{x} and correlation ϵ_{c}. A further improvement takes into account the gradient of the electron density, which is known as the generalised gradient approximation (GGA) [88], with the functional expressed as,

$$E_{\mathrm{xc}}^{\mathrm{GGA}}[\rho, \nabla\rho] = \int \rho(\mathbf{r})\epsilon_{\mathrm{xc}}^{\mathrm{GGA}}(\rho(\mathbf{r}), \nabla\rho(\mathbf{r}))d\mathbf{r}, \tag{2.44}$$

where $\epsilon_{\mathrm{xc}}^{\mathrm{GGA}}(\rho(\mathbf{r}), \nabla\rho(\mathbf{r}))$ now considers the electron density ρ and the gradient of the electron density $\nabla\rho$. The third approach is to use hybrid functionals, which incorporate a portion of exact exchange from HF. In this thesis the PBE0 hybrid functional is used with the form,

$$E_{\mathrm{xc}}^{\mathrm{PBE0}}[\rho] = aE_{\mathrm{x}}^{\mathrm{HF}} + (1-a)E_{\mathrm{x}}^{\mathrm{PBE}} + E_{\mathrm{c}}^{\mathrm{PBE}}, \tag{2.45}$$

where $a = 0.25$ [89]. The PBE0 functional combines exact exchange from HF into the PBE GGA functional [90]. Moreover, the choice of approximate functional for $E_{\mathrm{xc}}[\rho]$ is not obvious and can significantly affect the results in DFT. Therefore, the choice of functional requires benchmarking with higher level electronic structure methods. Nevertheless, DFT is a commonly used method for calculating ground state chemistry as it is computationally efficient and has high accuracy in many systems [91], and hence, will be employed later in this thesis for exploration of ground state processes.

To extend DFT to the calculation of excited states, time-dependent density functional theory (TDDFT) is used. TDDFT typically utilises a linear response approach to compute excitation energies from the ground state DFT calculations [92]. While TDDFT is widely employed, it shares limitations with other single-reference methods like ADC(2) and CC2, particularly in systems with static correlation. Additionally, TDDFT often struggles to accurately describe charge-transfer states [93, 94]. In this thesis, TDDFT was briefly explored for some studies, but it produced qualitatively incorrect results for the molecules in question, and thus will not be further discussed.

2.9 Observables

Here, the calculation of observables that enable direct comparison with experiment will be discussed. Specifically, the focus will be on time-resolved experiments, which use a pump-probe scheme to monitor the dynamic changes in a molecule. Later in this thesis, the trajectories obtained from TSH simulations will be utilised to calculate observables for both ultrafast X-ray scattering and time-resolved photoelectron spectroscopy, in order to connect the theory simulations to experimental results. Consequently, this section will discuss the theory behind computing the observables for these two experiments.

2.9.1 Ultrafast X-ray scattering

Ultrafast X-ray scattering (UXS) is a technique used to elucidate structural dynamics on ultrafast timescales. The X-ray probe pulse scatters off the electrons in the molecule and these scattered photons are recorded on a detector. The incident X-ray photons have an angular frequency and wave vector of ω_0 and $\mathbf{k}_0$, respectively, whereas the corresponding quantities for the scattered photons are ω_s and $\mathbf{k}_\mathrm{s}$. Therefore, the momentum-transfer vector $\mathbf{q}$ can be defined as the difference between the incident and scattered wave vectors $\mathbf{k}_0$ and $\mathbf{k}_\mathrm{s}$ such that,

$$\mathbf{q} = \mathbf{k}_0 - \mathbf{k}_\mathrm{s}. \tag{2.46}$$

Furthermore, if $\omega_0 \approx \omega_\mathrm{s}$ then the momentum transfer vector $\mathbf{q}$ is independent of ω_s, denoted by $\tilde{\mathbf{q}}$ and hence, the differential cross-section for total X-ray scattering is given by [95, 96],

$$\frac{d\sigma}{d\Omega} \propto \left(\frac{d\sigma}{d\Omega}\right)_\mathrm{Th} \sum_{i,j}^{N} \langle \chi_j(t) | \Lambda_{ji}(\tilde{\mathbf{q}}, \bar{\mathbf{R}}) | \chi_i(t) \rangle, \tag{2.47}$$

where $(d\sigma/d\Omega)_\mathrm{Th}$ is the Thomson scattering cross-section for a free electron and $|\chi_i(t)\rangle$ is the time-dependent nuclear wave packet evolving on electronic state $|\phi_i(\bar{\mathbf{R}})\rangle$. Additionally, Λ_{ij} is the total X-ray scattering probability of the molecule with nuclear coordinates $\bar{\mathbf{R}} = (\mathbf{R}_1, \ldots, \mathbf{R}_{N_\mathrm{at}})$ in electronic states, $|\phi_i(\bar{\mathbf{R}})\rangle$ and $|\phi_j(\bar{\mathbf{R}})\rangle$, defined by,

$$\Lambda_{ji}(\tilde{\mathbf{q}}, \bar{\mathbf{R}}) = \langle \phi_j(\bar{\mathbf{R}}) | \hat{L}^\dagger \hat{L} | \phi_i(\bar{\mathbf{R}}) \rangle, \tag{2.48)}$$

with the scattering operator $\hat{L}$ expressed as,

$$\hat{L} = \sum_{n=1}^{N_\mathrm{e}} \mathrm{e}^{(i\tilde{\mathbf{q}}\cdot\mathbf{r}_n)}. \tag{2.49}$$

The scattering matrix elements $\Lambda_{ji}(\tilde{\mathbf{q}}, \bar{\mathbf{R}})$ can also be written in terms of one- and two-electron parts,

$$\Lambda_{ji}(\tilde{\mathbf{q}}, \bar{\mathbf{R}}) = N_\mathrm{e}\delta_{ij} + \Lambda_{ji}^{2\mathrm{e}}(\tilde{\mathbf{q}}, \bar{\mathbf{R}}), \tag{2.50}$$

where the first term is the one-electron part and corresponds to the number of electrons N_e when $i = j$ and the second term is the two-electron scattering matrix element, which can be written as,

$$\Lambda_{ji}^{2\mathrm{e}}(\tilde{\mathbf{q}}, \bar{\mathbf{R}}) = 2 \iint \mathrm{e}^{i\tilde{\mathbf{q}}\cdot(\mathbf{r}_2-\mathbf{r}_1)}\rho_{ji}(\mathbf{r}_1, \mathbf{r}_2, \bar{\mathbf{R}})d\mathbf{r}_1 d\mathbf{r}_2, \tag{2.51}$$

and is the double Fourier transform of the two-electron density $\rho_{ji}(\mathbf{r}_1, \mathbf{r}_2, \bar{\mathbf{R}})$, given by,

$$\rho_{ji}(\mathbf{r}_1, \mathbf{r}_2, \bar{\mathbf{R}}) = \langle\phi_j(\bar{\mathbf{R}})|\hat{\rho}(\mathbf{r}_1, \mathbf{r}_2)|\phi_i(\bar{\mathbf{R}})\rangle, \tag{2.52}$$

with

$$\hat{\rho}(\mathbf{r}_1, \mathbf{r}_2) = (1/2)\sum_{m}^{N_\mathrm{e}} \sum_{n\neq m}^{N_\mathrm{e}} \delta(\mathbf{r}_1 - \mathbf{r}_m)\delta(\mathbf{r}_2 - \mathbf{r}_n), \tag{2.53}$$

where $\mathbf{r}_1$ and $\mathbf{r}_2$ are the coordinates of electron one and two, respectively [95, 96].

In Eq. 2.50, the one- and two-electron terms where $i = j$ contribute significantly more to the scattering signal, by at least two orders of magnitude, compared to where $i \neq j$. This dominant contribution is referred to as the total scattering, which is the primary focus of this thesis. The total scattering signal, which reflects the nuclear dynamics, includes both elastic and inelastic contributions. The elastic component is proportional to the absolute squared form factor,

$$|F_i(\tilde{\mathbf{q}})|^2 = |\langle\phi_i(\bar{\mathbf{r}})|\hat{L}|\phi_i(\bar{\mathbf{r}})\rangle|^2 = \left|\int \mathrm{e}^{i\tilde{\mathbf{q}}\cdot\mathbf{r}_1}\rho_i(\mathbf{r}_1)d\mathbf{r}_1\right|^2, \tag{2.54}$$

which can be written as the absolute squared Fourier transform of the one-electron density $\rho_i(\mathbf{r}_1)$. The inelastic scattering component $S_i(\tilde{\mathbf{q}})$, which results from an

X-ray photon inducing an electronic transition in a molecule, can then be calculated by subtracting the elastic component from the total scattering,

$$S_i(\tilde{\mathbf{q}}) = \Lambda_{ii}(\tilde{\mathbf{q}}, \bar{\mathbf{R}}) - |F_i(\tilde{\mathbf{q}})|^2. \tag{2.55}$$

It should be noted that so far all equations have been defined for perfectly aligned molecules, where the scattering is dependent on both the geometry and the direction of the molecule. However, a gas-phase sample does not contain any rotational information, and thus to allow direct comparison to experiment, the scattering probabilities have to be rotationally averaged, which is detailed elsewhere [31]. Moreover, when rotationally averaged, the scattering loses all angular dependence and therefore, now only depends on the magnitude of $\tilde{\mathbf{q}}$, denoted as $\tilde{q}$.

The total [97, 98] and elastic [99–102] scattering cross-sections can be calculated for a set of TSH trajectories, using electronic structure methods, such as CASSCF, to compute the one- and two-electron densities. In addition the nuclear wave packet can be represented as an ensemble of equally weighted trajectories, where each trajectory is on a particular electronic state at time t. However, this is commonly too resource intensive and hence, approximate matrix elements can be calculated using the independent atom model (IAM) [103]. The IAM approximation considers the molecule as a set of isolated atoms centred at the positions of the nuclei, where the electron density around each atom is assumed to be isotropic, and does not include any effects due to bonding. This approach is effective as the core electrons closely follow the motion of the nuclei [104]. Therefore, the total scattering according to the IAM is,

$$\Lambda_{\mathrm{IAM}}(\tilde{\mathbf{q}}, \bar{\mathbf{R}}) = |F_{\mathrm{IAM}}(\tilde{\mathbf{q}})|^2 + S_{\mathrm{IAM}}(\tilde{\mathbf{q}}) = \left| \sum_{A=1}^{N_A} f_A^{\mathrm{IAM}}(\tilde{q}) \mathrm{e}^{i\tilde{\mathbf{q}}\mathbf{R}_A} \right|^2 + \sum_{A=1}^{N_A} S_A^{\mathrm{IAM}}(\tilde{q}), \tag{2.56}$$

where $f_A(\tilde{q})$ are the tabulated atomic form factors for elastic scattering, and $S_A(\tilde{q})$ are the corresponding atomic inelastic scattering terms, which describe the isotropic scattering from each atom A [105]. The elastic scattering depends on the nuclear positions R_A, whereas the inelastic terms are independent of molecular geometry. Moreover, when rotational averaging is included, the equation becomes,

$$\Lambda_{\mathrm{IAM}}(\tilde{q}, \bar{\mathbf{R}}) = \sum_{A,B}^{N_A} f_A^{\mathrm{IAM}}(\tilde{q}) f_B^{\mathrm{IAM}}(\tilde{q}) \frac{\sin \tilde{q} R_{AB}}{\tilde{q} R_{AB}} + \sum_{A=1}^{N_A} S_A^{\mathrm{IAM}}(\tilde{q}), \tag{2.57}$$

where R_{AB} is the distance between atoms A and B. Although the IAM method is relatively successful, it does have some shortcomings such as not including effects due to distortion of the electron density [100, 106, 107] in addition to information about electronic states [99], both of which are important in photochemical reactions.

2.9.2 Time-resolved photoelectron spectroscopy

Time-resolved photoelectron spectroscopy (TRPES) is a tool employed to investigate photochemical dynamics, where the probe pulse ionises the molecule from a specific electronic state, ejecting a photoelectron. The kinetic energy of these photoelectrons, at different time delays, gives insight into the evolution of the molecule in different electronic states. The binding energy, which is a measure of how strongly bound an electron is in a molecule, can be directly calculated from the kinetic energy. Considering a one photon process, the binding energy E_{BE} is given by,

$$E_{\mathrm{BE}} = \hbar\omega - E_{\mathrm{KE}}, \tag{2.58}$$

where ω is the angular frequency of the probe and E_{KE} in the kinetic energy of the photoelectron.

The photoionisation cross-section σ_{if} is proportional to the squared electric dipole transition moment $\mathbf{D}_{if}^k$, within the dipole approximation, and is defined as

$$\sigma_{if} \propto |\langle \Psi_i | \boldsymbol{\mu} \cdot \boldsymbol{\epsilon} | \Phi_f^k \rangle|^2, \tag{2.59}$$

where Ψ_i is the wave function of the initial state, Φ_f^k is the wave function of the final continuum state, where k refers to the momentum of the photoelectron, and finally, $\boldsymbol{\mu} \cdot \boldsymbol{\epsilon}$ is the dot product of the dipole operator and the probe field [108]. If an approximation is made that ionisation occurs between specific electronic states, from the neutral molecule to the ion, Φ_f^k can be written as a product of the wave function for the final ion state Ψ_f and the photoelectron wave function Ψ_k^{el}, and hence, the dipole transition moment can be written as,

$$\mathbf{D}_{if}^{k} = \langle \Psi_i | \boldsymbol{\mu} \cdot \boldsymbol{\epsilon} | \Psi_f \Psi_k^{\text{el}} \rangle = \langle \phi_{if}^{d} | \boldsymbol{\mu} \cdot \boldsymbol{\epsilon} | \Psi_k^{\text{el}} \rangle, \tag{2.60}$$

where ϕ_{if}^{d} is the one-electron Dyson orbital [109, 110], which is the overlap between the initial and final wave functions, of the neutral and cationic states, respectively,

$$\phi_{if}^{\text{d}}(\mathbf{r}) = \sqrt{N} \int \Psi_i(r_1, \ldots, r_N) \Psi_f(r_2, \ldots, r_N) dr_2 \ldots dr_N. \tag{2.61}$$

Moreover, the norm of the Dyson orbitals gives the probability of a transition, and hence the photoionisation cross-section can be approximated as the squared Dyson norm. Thus, this approximation is applied to calculate the photoelectron signal for an ensemble of TSH trajectories later in this thesis. For each trajectory, the Dyson orbitals and norms are calculated at each time step between the active the state in the simulation and the ion states of interest to calculate the approximate photoionisation cross-section, which is then convolved with a Gaussian function to produce the photoelectron signal at each time step. Therefore, the photoelectron signal is calculated using,

$$S(t, E_{\text{BE}}) = \sum_{\gamma}^{N_{\text{traj}}} \sum_{f}^{N_{\text{ion}}} |\langle \Psi_i^{\gamma} | \Psi_f^{\gamma} \rangle|^2 g(\Delta t, E_{\text{BE}}), \tag{2.62}$$

where $|\langle \Psi_i^{\gamma} | \Psi_f^{\gamma} \rangle|^2$ is the squared Dyson norm, in which $|\Psi_i^{\gamma}\rangle$ is the wave function of the initial state, corresponding to the active state in the TSH simulations, and $|\Psi_f^{\gamma}\rangle$ is the wave function of the final ion state. The Dyson norms are computed between the active state and all ion states of interest for all trajectories. Finally, $g(\Delta t, E_{\text{BE}})$ is the Gaussian function, which takes into account the cross-correlation between the pump and probe, and is centred at the binding energy E_{BE}. Although this method provides a computationally efficient way of calculating an approximate photoelectron signal, it will have shortcomings as it does not take into consideration the wave function of the photoelectron or the dipole moment of the transition. Improved approximations that include explicit representations of the free photoelectron can be found in approaches such as ezDyson [111] and the R-matrix method [112].

3

Cyclopentadiene

Sections of this chapter have been reproduced from Ref. [113] with permission from the Royal Society of Chemistry.

3.1 Introduction

Conjugated polyenes are known to undergo ultrafast photochemical reactions, which include *cis*-*trans* isomerisation [2, 114, 115] and pericyclic reactions such as electrocyclic reactions and sigmatropic rearrangements. The formation of highly strained ring products through photochemical electrocyclic ring closure with a high quantum yield is of particular interest and could potentially lead to new synthetic methods of these energetically unfavourable systems [116–118]. Butadiene has been used as prototype for conjugated dienes to gain insight into the ultrafast photorelaxation mechanisms and is known to have two competing mechanisms: *cis*-*trans* isomerisation and electrocyclic ring closure [119–121]. Larger ring systems, such as cyclo-octa-1,3-diene, also exhibit competing mechanisms including *cis*-*trans* isomerisation upon excitation [114, 122].

In contrast, a molecule with a conformational lock such as cyclopentadiene (CP), will remove the competing isomerisation process. CP has been the subject of intense study, having previously been used as a model system for *s*-*cis*-diene molecules to explore their ultrafast dynamics, both experimentally [123–125] and theoretically [126]. The main focus of these studies was the very short timescale nonadiabatic photorelaxation pathways, and not the subsequent ground state dynamics leading to the formation of photoproducts. CP is known to form two highly strained photoproducts: bicyclo[2.1.0]pentene (BP) and tricyclo[2.1.0.0^{2,5}]pentane (TP), where electrocyclic ring closure occurs [116–118] and these geometries are shown in Fig. 3.1.

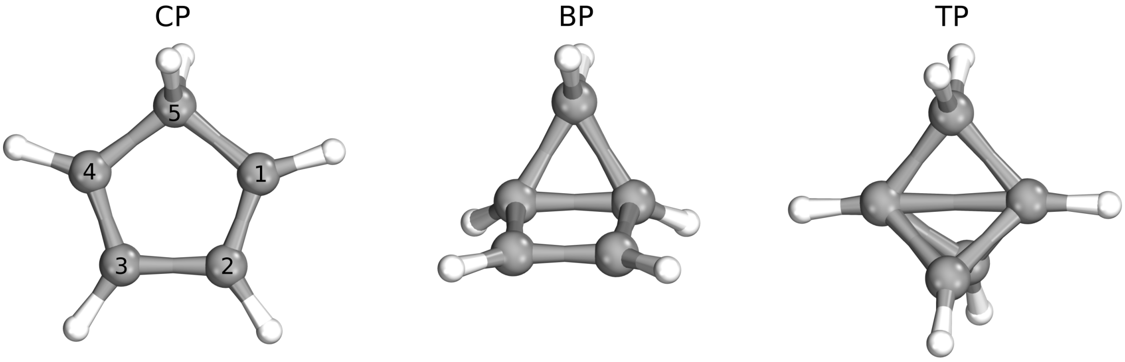

Figure 3.1: Ground state geometries of cyclopentadiene (CP), bicyclo[2.1.0]pentene (BP) and tricyclo[2.1.0.0^{2,5}]pentane (TP), with a numbering scheme given for CP, which is referred to later in the text.

The ultrafast dynamics in CP upon excitation to the $1B_2$ ($\pi\pi^*$) state has been explored experimentally using time-resolved ionisation mass and photoelectron spectroscopy [123–125]. It is thought that the relaxation from the $1B_2$ state to the ground state occurs through the spectroscopically dark $2A_1$ state. However, this state has been located theoretically and has been shown to lie above the $1B_2$ state in the FC region [126–129]. Consequently, time-resolved experimental studies have invoked CIs to explain the short timescale dynamics.

The experimental study by Fuß *et al.* used intense-field ionisation to track the short time (< 350 fs) dynamics of CP, suggesting two competing processes for the relaxation of CP and proposed the mechanism shown in Fig. 3.2 [123]. Following excitation to the $1B_2$ state, the authors proposed that the molecule decays to the dark $2A_1$ state within 37 fs from where two different CIs with the ground state are invoked, associated with two photochemical pericyclic reactions: either an electrocyclisation reaction to form BP and TP (71 fs) or a 1,3-sigmatropic hydrogen shift with a time

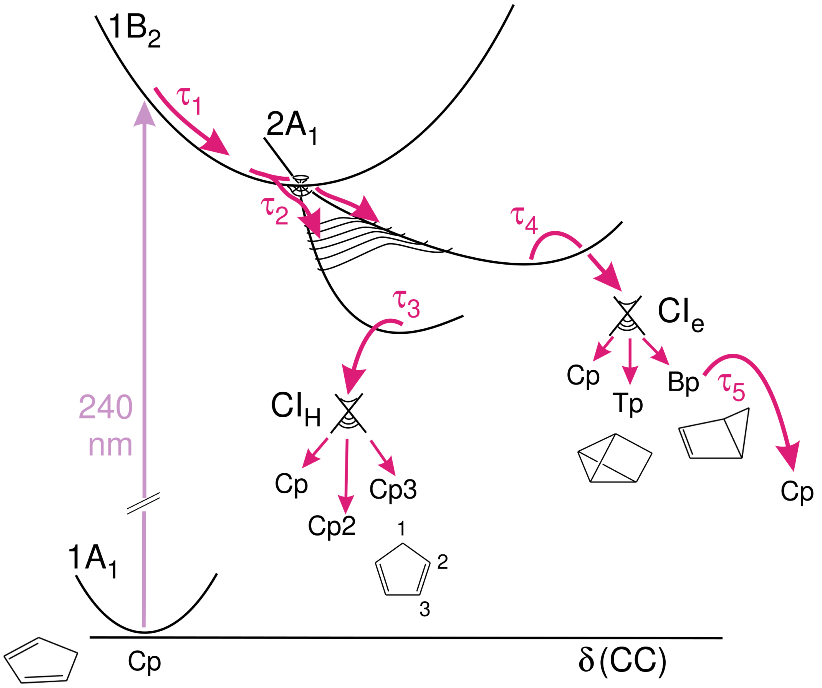

Figure 3.2: Photorelaxation mechanism of CP proposed by Fuß *et al.*, upon excitation at 240 nm. Figure adapted from Ref. [123].

constant of 333 fs, where the hydrogen shift is thought to be dominant. In addition, the long scale dynamics (time constant of ≈ 19 ps) on the hot ground state was also observed and was ascribed to the thermal back reaction from BP to CP.

Theoretically, the ultrafast dynamics of CP has been explored using AIMS with MS-CASPT2 for the electronic structure [126]. From these simulations, upon 100% excitation into S_1 ($1B_2$) it was observed that torsion around one or both of the carbon-carbon double bonds is essential for reaching the S_1/S_0 CI seam. Kuhlman *et al.* associated this torsion motion with the disrotatory mechanism that would occur to form the BP photoproduct, however, the simulations were terminated once the ground state was populated and therefore, no photoproducts were observed.

Despite these previous studies, the formation of the highly-strained photoproducts have not been directly observed in the ultrafast dynamics experiments [123, 124] or the theoretical investigation by Kuhlman *et al.* [126]. These strained ring structures are sufficiently distorted from the CP, which makes this system an interesting and suitable target for UXS experiments. Therefore, the aim of this body of work is determine the mechanistic details of the formation of these photoproducts and predict signals for upcoming UXS experiments.

Hence, in this chapter, the ultrafast dynamics of CP are investigated using an ensemble of surface hopping trajectories to simulate the nonadiabatic transitions. The simulations are extended to include ground state dynamics up to 10 ps in order to locate the formation of photoproducts on the hot ground state. Finally, to predict scattering signals in UXS gas-phase experiments, which were later performed, the time-dependent X-ray scattering signal is computed at multiple levels of theory, and contributions from the different pathways are elucidated.

3.2 Computational methods

3.2.1 Excited state electronic structure

The electronic structure was calculated at the XMS-CASPT2 level [70], with the cc-pVDZ basis set, using the BAGEL 1.1 software package [130, 131]. A level shift of 0.3 Hartree was applied along with the SS-SR contraction scheme. The $(4,4)$ active space, shown in Fig. 3.3, consists of four electrons in four orbitals, with two sets of π and π^* orbitals. The resulting XMS(3)-CASPT2(4,4)/cc-pVDZ method is the default method in all calculations.

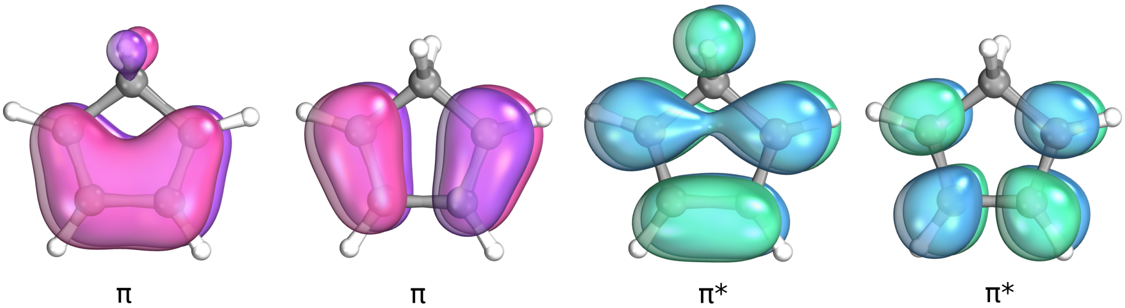

Figure 3.3: The (4,4) active space in CP, consisting of 2 π and 2 π^* orbitals.

The ground state minimum energy geometry of CP and the photoproducts were optimised and vibrational normal modes determined. The MECIs were located, and potential energy (PE) profiles were constructed by linear interpolation in internal coordinates (LIIC) between the ground state minimum energy geometry and the relevant MECIs and/or ground state minimum energy geometries of photoproducts. The MECI leading to the BP photoproduct was visualised by expanding along the direction of the orthonormalised branching plane vectors, X and Y, in Cartesian coordinates.

3.2.2 Franck-Condon calculations

The vibronic spectrum of CP was computed using adiabatic hessian FC calculations [132] with the FCclasses 3.0 software package [133]. This method computes the overlap between vibrational states using a harmonic approximation around the minima of the ground and excited states. The spectrum is then calculated by summing over all transitions with significant overlap. Initially, only the ground vibrational state of the ground electronic state is populated (a 0 K approximation, as no hot bands were observed experimentally). The transitions are then broadened using a Gaussian with a 0.032 eV FWHM, chosen to maximise agreement with the experimental data. A constant transition dipole moment was assumed (the Condon approximation), as no Herzberg-Teller effects were observed in the experimental spectrum.

To calculate the spectrum, the ground state minimum of CP was re-optimised with SCS-MP2 and the $1B_2$ state was optimised with SCS-ADC(2) [74, 75], utilising the aug-cc-pVQZ basis set. Both optimisations were performed with symmetry constraints of C_{2v} in Turbomole 7.7 [134]. SCS-ADC(2) provides a good description of the $1B_2$ state, compared to XMS(3)-CASPT2(4,4) and allows the vibrational spectrum to be calculated easily.

3.2.3 Absorption spectrum and nonadiabatic dynamics

The UV-vis absorption spectrum was calculated using the SHARC software package [58] from 10^4 initial geometries obtained by sampling the Wigner distribution of the ground state harmonic oscillator at 0 K, with excitation energies and oscillator strengths computed at each geometry. Initial conditions for the nonadiabatic dynamics were sampled using an excitation window of 5.07-5.13 eV, consistent with a laser pulse duration of 70 fs at 243 nm.

The nonadiabatic excited state dynamics were simulated using Tully's fewest switches surface hopping algorithm [53] as implemented in the SHARC 2.1 software package [58, 135, 136] interfaced with BAGEL [130, 131]. Granucci and Persico's energy-based decoherence scheme was used with a decoherence parameter of 0.1 Hartree [54]. The excited state dynamics were propagated with a 0.1 fs time step for the nuclei and an electronic time step of 0.004 fs.

The trajectories were propagated until they reached the electronic ground state, at which point they were propagated for a further 15 fs before switching to a different method as described below. The method is changed as the $(4, 4)$ active space is unstable for some geometries accessed during the dynamics on the hot ground state. A range of DFT functionals (see Appendix B.1) were evaluated against XMS-CASPT2 PE profiles to identify a suitable functional for the ground state dynamics, and PBE0/def2-SV(P) was found to produce very similar results to XMS-CASPT2 along the PE ground state profiles. Therefore, the ground state trajectories were propagated using PBE0/def2-SV(P) as implemented in Turbomole 7.5 [137] interlinked with Newton-X 2.4 [138, 139]. The final geometries and velocities from the XMS-CASPT2 trajectories were used as a starting point for these ground state trajectories, which were propagated for 20 ps with a 0.05 fs time step, where the smaller integration step is used to account for the large kinetic energy on the ground state.

3.2.4 Ground state reactions

Further analysis of the ground state chemistry was carried out using DFT with the PBE0 functional [89] and the def2-TZVP basis set in the Orca 4.2.1 software package [140]. The ground state minima of CP and the photoproducts were re-optimised with this level of theory and the transition states (TSs) between CP and the photoproducts were located. To validate these TSs, intrinsic reaction coordinate (IRC) pathways were computed, following the reaction coordinate associated with the imaginary frequency to the nearest minimum in the forward and reverse directions [141]. These IRC pathways lead to the expected reactant and product for both

TSs, confirming the nature of the TSs. Minimum energy pathways (MEPs) were computed between CP, the TS and the photoproducts using the nudged elastic band (NEB) approach to visualise the PES [142].

Finally, time constants for the ground state processes were calculated using RRKM theory, evaluating the sum and density of vibrational states classically, in order to compute the rate constant with the following expression,

$$k(E) = \frac{\Pi_{i=1}^{s}\nu_i}{\Pi_{i=1}^{s-1}\nu_i^{\ddagger}}\left(\frac{E-E_0}{E}\right)^{s-1}, \tag{3.1}$$

where ν_i and $\nu_i^{\ddagger}$ are the vibrational frequencies of the reactant and TS, respectively, E is the internal energy of the system, E_0 is the barrier height and s is the degrees of freedom. The internal energy is approximated as the sum of the reactants zero-point energy (ZPE) and the central excitation energy used for the dynamics simulations (5.1 eV).

3.2.5 Ultrafast X-ray scattering

The UXS signals for the ensemble of trajectories were calculated using the rotationally averaged form of the IAM (Eq. 2.57), where each trajectory is weighted equally. Moreover, the *ab initio* X-ray scattering signals were computed using the theory discussed in Section 2.9.1. The wave functions were calculated from single point calculations at the XMS(3)-CASPT2(4,4) level with the cc-pVDZ basis set using Cartesian spherical harmonics in the OpenMolcas v22.10 electronic structure software package [143, 144].

3.3 Results and discussion

3.3.1 Electronic structure

The ground state minimum energy geometry of CP consists of a planar ring structure and the ground state electronic configuration in the (4,4) active space is comprised of four electrons in the two π orbitals. At this geometry, the S_1 state has a vertical excitation energy of 5.30 eV and is a $\pi\pi^*$ state, while the S_2 state lies ~1.2 eV above S_1 and is composed of approximately a 50% contribution from a doubly excited $\pi \rightarrow \pi^*$ transition. The ordering of these excited states and their excitation energies is consistent with previous experimental [124, 145] and theoretical work [126, 128, 129, 146], where the $1B_2$ $\pi\pi^*$ state is lower in energy than the $2A_1$ $((\pi)^2 \rightarrow (\pi^*)^2)$ state in the FC region.

In the previous experimental work by Fuß *et al.*, a CI associated with an electrocyclisation reaction to form BP was hypothesised [123] and Kuhlman *et al.* found three S_1/S_0 MECIs at the MS(3)-CASPT2(4,4)/6-31G** level of theory [126]. Two of these MECIs correspond to torsion around one of the double bonds (*eth*1-MECI and *eth*2-MECI), and the third is associated with disrotatory motion where both double bonds twist (*dis*-MECI). All three MECIs located by Kuhlman *et al.* are related to torsion of the ring, and hence, are likely to be correlated to the electrocyclisation reaction from CP to BP. Therefore, each of these geometries were optimised using XMS(3)-CASPT2(4,4)/cc-pVDZ and all three optimisations converged to a single S_1/S_0 MECI. The geometry of this MECI, included in Fig. 3.5, is very similar to *eth*1-MECI, with torsion around one of the double bonds occurring. This is in agreement with the findings of Santolini *et al.*, who used restricted active space self-consistent field (RASSCF) with a $(5, 4, 5) + 3p$ active space to optimise these three S_1/S_0 MECIs and, similarly, only found one geometry [146]. Furthermore, their converged S_1/S_0 MECI structure also had a similar geometry to *eth*1-MECI.

The region around the S_1/S_0 MECI has been investigated by expanding along the orthonormalised branching plane vectors, X and Y, in Cartesian coordinates and is shown in Fig. 3.4. The X vector is predominantly associated with the torsion around the $C_3{-}C_4$ bond, leading to changes in the $C_2{-}C_3{-}C_4{-}C_5$ dihedral angle, while the Y vector is related to changes in the $C_1{-}C_2$, $C_2{-}C_3$ and $C_3{-}C_4$ bond lengths. From analysis according to Galván *et al.* [147], this MECI is peaked, and therefore, it is likely to act as a funnel for photorelaxation from the S_1 state to the ground state, and hence, once the MECI is approached, the ground state will be quickly populated. In addition, this MECI is bifurcating, leading to two different photoproducts. Depending on the direction that the MECI is approached, it may

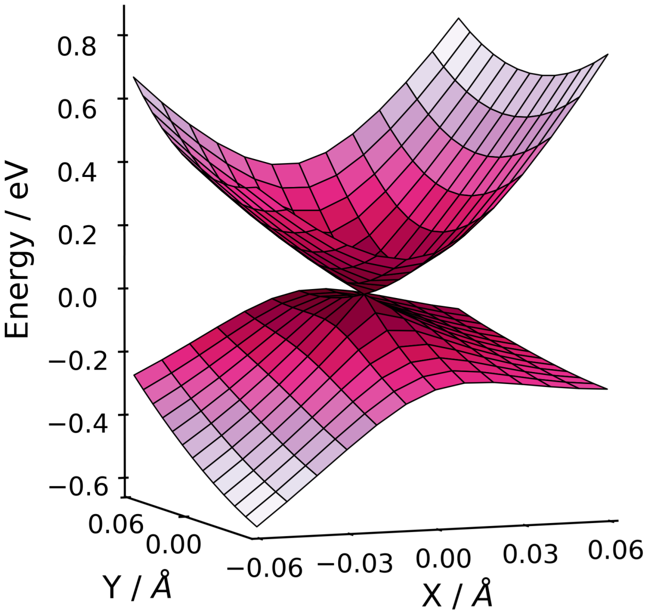

Figure 3.4: Visualisation of the region around the peaked, bifurcating S_1/S_0 MECI leading to the BP photoproduct, calculated at the XMS(3)-CASPT2(4,4)/cc-pVDZ level of theory.

lead to the formation of different photoproducts, which is consistent with later observations in the dynamics simulations. Following the negative displacement of both branching plane vectors, will lead to CP, and following the direction of the positive displacement will lead to the ring strained photoproduct BP.

To visualise the stretch of the PES connecting the ground state minimum energy geometry of CP, in the FC region, to the located S_1/S_0 MECI, the PE LIIC is shown on the left-hand side (LHS) of Fig. 3.5. Along the S_1 surface, this pathway has a barrierless transition to the S_1/S_0 MECI. Therefore, accessing this MECI from the FC region on the S_1 surface would likely be predicted to be a relatively facile process. In the FC region, the S_1 state has $\pi\pi^*$ character while S_2 possesses a large amount of doubly excited state character. Moving across the PES to the central region of the LIIC pathway, the characters of S_1 and S_2 mix, resulting in both states having partial $\pi\pi^*$ and doubly excited state character. This indicates that the coupling between these two states, in this region of the PES, is fairly large.

As the MECI is approached and the energies of the two states begin to diverge, the character of the two states return to their original character in the FC region.

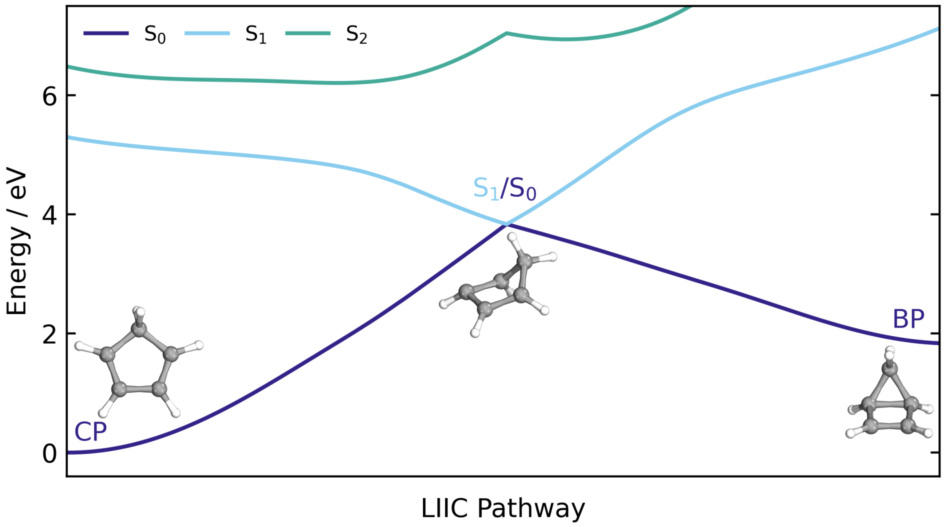

Figure 3.5: LIIC pathway connecting the S_0 minimum energy geometry of CP to the photoproduct BP *via* the S_1/S_0 MECI. Both pathways are computed at the XMS(3)-CASPT2(4,4)/cc-pVDZ level of theory.

As the S_1/S_0 MECI is associated with torsion of the ring, it has a geometry resembling the formation of BP. Furthermore, analysis of the branching plane vectors, shown in Fig. 3.4, leads to geometries heading towards BP in one direction. Therefore, it is reasonable to predict that this MECI lies along the pathway to the formation of the BP photoproducts, which makes this electrocyclisation reaction quite accessible. Thus, the LIIC pathway on the LHS of Fig. 3.5 was extended to include the pathway from the MECI to BP, which is shown on the right-hand side (RHS). From the S_1/S_0 MECI, the pathway is barrierless to BP, and hence, the formation should be readily occurring once this MECI has been traversed. However, as the MECI is bifurcating the photoproduct formed will likely depend on the direction that the MECI is approached.

In addition to a CI associated with the electrocyclisation reaction, Fuß *et al.* predicted a CI related to a hydrogen shift reaction, either a 1,2- or 1,3-hydrogen shift, where the H atom migrates from C_5 to either C_1 or C_2, respectively [123]. A CI has previously been located for the 1,3-H shift in propene, using CASSCF, and the migrating H is located above C_2 with a bond distance of 1.8 Å [148]. Thus, this distance was applied between C_1 and the migrating H in CP and this geometry was optimised at the XMS(3)-CASPT2(8,8)/cc-pVDZ level. The increased active space includes the two C−H σ orbitals and the two C−H σ^* orbitals, as required to describe the migration of H to another C atom. The only MECI geometry that was located has a much longer bond distance between C_1 and the migrating H of ~2.8 Å, included in Fig. 3.6 (a), and is a peaked, single path MECI leading to H dissociation rather than H migration. In the LIIC pathway, shown in Fig. 3.6 (a), there is a barrier along the S_1 surface, from CP to this S_1/S_0 MECI, which is absent along the pathway to access the S_1/S_0 MECI associated with electrocyclisation, and therefore the electrocyclisation is likely the dominant pathway.

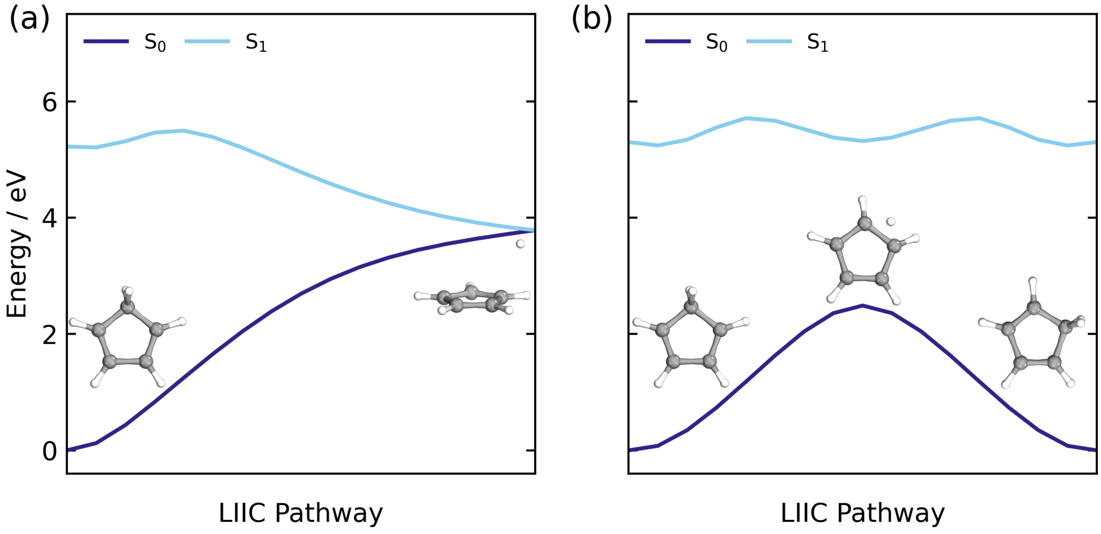

Figure 3.6: LIIC pathway connecting the S_0 minimum energy geometry of CP to the S_1/S_0 MECI associated with H dissociation (a) and the 1,2-hydrogen shift product of CP (b). Both pathways are computed at the XMS(3)-CASPT2(8,8)/cc-pVDZ level of theory.

Furthermore, a LIIC pathway was constructed from CP to the 1,2-hydrogen shift product of CP, to confirm there was no MECI associated with the 1,2-H shift pathway. Again, these energies were computed at the XMS(3)-CASPT2(8,8)/cc-pVDZ level and the resulting pathway is shown in Fig. 3.6 (b). Across this pathway, there is a large energy gap between the S_1 state and the ground state and there are no regions that resemble a S_1/S_0 crossing point. Therefore, it seems highly probable that the hydrogen shift reaction is a ground state process that is accessed *via* the same S_1/S_0 MECI that leads to the electrocyclisation reaction.

3.3.2 Absorption spectrum

3.3.2.1 Nuclear ensemble approach

The UV-vis absorption spectrum was calculated from the ground state ensemble and is shown in Fig. 3.7 [149]. The spectrum contains one absorption band with a peak maximum around 5.17 eV (240 nm). The only contributing state to this absorption band is S_1 and the maximum of this band is comparable to the vertical excitation energy of S_1 in the FC region, which is ascribed to the optically bright $\pi\pi^*$ state ($1B_2$). The spectrum also has a small contribution at 6.0-6.2 eV from the dark doubly excited S_2, $(\pi)^2 \rightarrow (\pi^*)^2$, state.

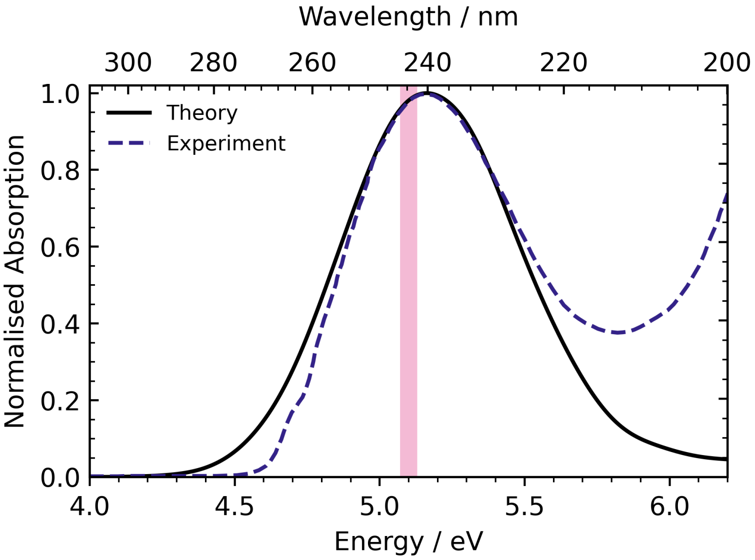

Figure 3.7: UV-vis absorption spectrum of CP simulated at the XMS(3)-CASPT2(4,4)/cc-pVDZ level compared to the experimental spectrum reported by Schalk *et al.* [124]. The excitation window (5.07-5.13 eV) used for the nonadiabatic dynamics simulations is shown by the pink shaded region on the spectrum.

Comparing to the experimental absorption spectrum reported by Schalk *et al.* [124], also included in Fig. 3.7, the peak maximum of the calculated spectrum is almost identical to that of the experimental spectrum and the shape of the broad peak is also similar. However, at higher energies, in the region between

5.75 and 6.2 eV, there is an onset of another absorption band in the experimental data, which is absent in the calculations. This absorption is due to the 3s and 3p Rydberg states, which are not included in the (4,4) active space. The reason for excluding the Rydberg orbitals is that the Rydberg states shift to higher energies as the molecular geometry distorts away from the FC region towards the S_1/S_0 MECI, and hence, these states are not involved in the dynamics at our chosen excitation wavelength. Finally, Fig. 3.7 shows the excitation window at 5.07-5.13 eV, for the nonadiabatic surface hopping dynamics simulations, as a pink shaded region. The excitation region is used to to simulate the same region as in recent experiments performed on CP [150].

3.3.2.2 Franck-Condon calculations

Although the experimental spectrum by Schalk *et al.*, included in Fig. 3.7, has no vibrational structure, the spectrum previously reported by Sabljíc and McDiarmid, shows vibrational progressions [151]. To gain insight into these vibrational progressions, FC calculations have been computed, where the adiabatic hessian of the initial and final states are used to calculate the overlap of the vibrational wavefunction (see Section 3.2.2) [132]. As this approximation is only valid for a ground and excited state that has sufficient overlap, an excited state minimum that lies close to the ground state FC geometry is required. In CP, the optimisation of the S_1 minimum without symmetry leads to a minimum with little overlap with the FC region and hence, symmetry restrictions of C_{2v}, were invoked to optimise the $1B_2$ state. The optimised $1B_2$ minimum, corresponds to a slight elongation of the double bonds from 1.35 Å in the ground state to 1.4 Å, and is a TS on the S_1 surface, where the imaginary frequency corresponds to the out of plane motion of the whole CH_2 moiety. This TS is assumed to be sufficiently long-long lived, and the imaginary frequency leads towards the direction of the S_1/S_0 MECI, associated with electrocyclic ring closure.

The vibrational spectrum for the $1B_2$ state, computed with SCS-ADC(2)/aug-cc-pVQZ, is shown in comparison to the spectrum presented by Sabljíc and

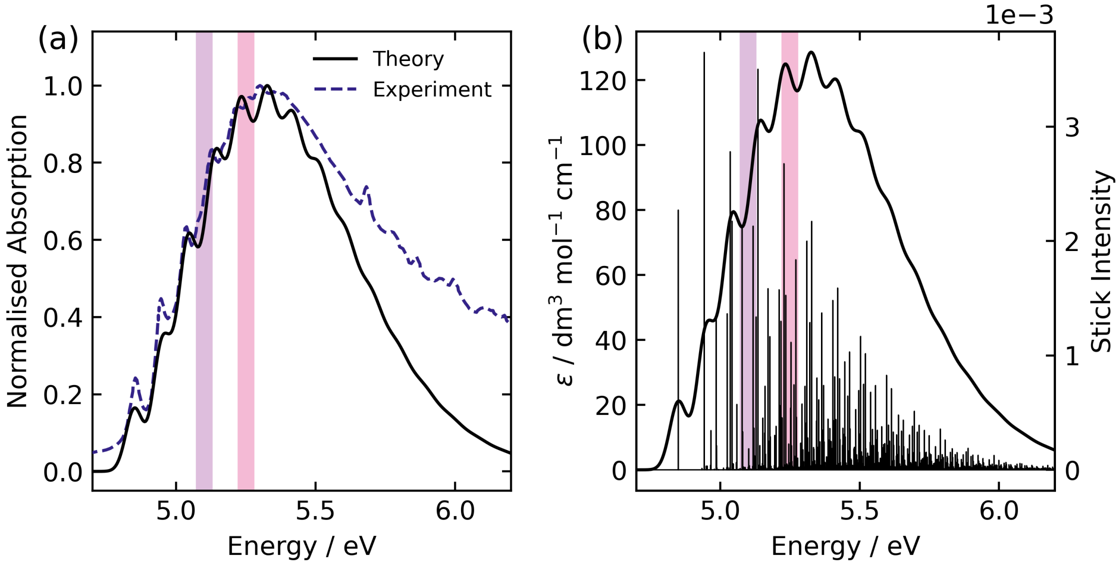

Figure 3.8: Vibrational spectrum of the $1B_2$ state in CP, compared to experiment (a) [151], and individual contributions to the this spectrum shown in (b). The spectrum has been calculated at the SCS-ADC(2)/aug-cc-pVQZ level of theory and the stick spectra have been convoluted using a Gaussian with a FWHM of 0.032 eV. The spectrum has been shifted by 0.08 eV for comparison purposes.

McDiarmid in Fig. 3.8 (a), where the theoretical spectrum has been shifted by 0.08 eV for comparison purposes [151]. Although the $1B_2$ state is slightly higher in energy than in the experimental spectrum, the shape and relative positions of the vibrational progressions are almost identical. Sabljíc and McDiarmid proposed these progressions are due to the C=C stretching vibration with a vibrational frequency of 745 cm^{-1} in the excited state. However, from analysis of the stick spectrum, shown in Fig. 3.8 (b), the FC active mode contributing to these vibrational peaks is associated with the $C_1{-}C_4$ stretching vibration, with a frequency of 750 cm^{-1}. Interestingly, this mode leads to formation of the four-membered ring observed in BP. In addition to this FC active mode, each peak is comprised of multiple underlying transitions, associated with the C=C and $C_2{-}C_3$ stretching vibrations. Moreover, Sabljíc and McDiarmid estimated the excited state lifetime as 37 fs, which is consistent with the mean time period, 33 fs, of the two most important modes contributing to the vibrational structure, namely the $C_1{-}C_4$ and $C_2{-}C_3$ stretching vibrations.

As a note, the peak maximum in the Sabljíc and McDiarmid spectrum is located 0.15 eV higher in energy compared to the spectrum reported by Schalk *et al.*

[124, 151]. Therefore, two excitation regions are shown in Fig. 3.8 (b). Firstly, the purple shaded region corresponds to the excitation window of 5.07-5.13 eV on the Sabljíc and McDiarmid spectrum and the pink shaded region corresponds to 5.07-5.13 eV in Fig. 3.7, which is used for the surface hopping simulations. From analysis of the stick spectra, in Fig. 3.8 (b), both regions will excite the C_1-C_4 and C=C stretching vibrations. The main difference is that in the higher energy pink region, the C_2-C_3 stretching vibration would also be excited. However, as vibrational states are not explicitly defined in surface hopping, this difference is unlikely to make a large impact on the results of the simulations.

3.3.3 Dynamics simulations

3.3.3.1 Populations

Surface hopping excited state dynamics simulations of CP were performed using the excitation window of 5.07-5.13 eV, with ∼480 trajectories starting on the bright S_1 state. The resulting classical adiabatic populations for the first 250 fs, shown in Fig. 3.9, reveal that the excited state population in S_1 is quickly transferred to the ground state, as the S_1 population decreases by 50% in approximately 75 fs. This timescale is similar to the AIMS simulations by Kuhlman *et al.*, where the S_1 population decreased by 50% in 53 fs [126]. Figure 3.9 also shows a small amount of population transfer (∼5%) to the S_2 state in the initial 10 fs. This population transfer takes place in regions where the nonadiabatic coupling between the S_1 and S_2 states is large, as observed when calculating the LIIC path from the FC region to the S_1/S_0 MECI in Fig. 3.5. Subsequently, the S_2 population returns to S_1 when the CI with the ground state is approached.

Finally, Fig. 3.9 shows a small population ascribed to H-atom dissociation, identified as trajectories associated with dissociation of the H atom on C_5. Since the $(4, 4)$ active space used in the simulations does not describe H-dissociation correctly, these trajectories are terminated. In addition, a small number of trajectories crash when they reach nonphysical molecular geometries (including one ring-opening) for which the CASSCF fails to converge. These failed trajectories only make up

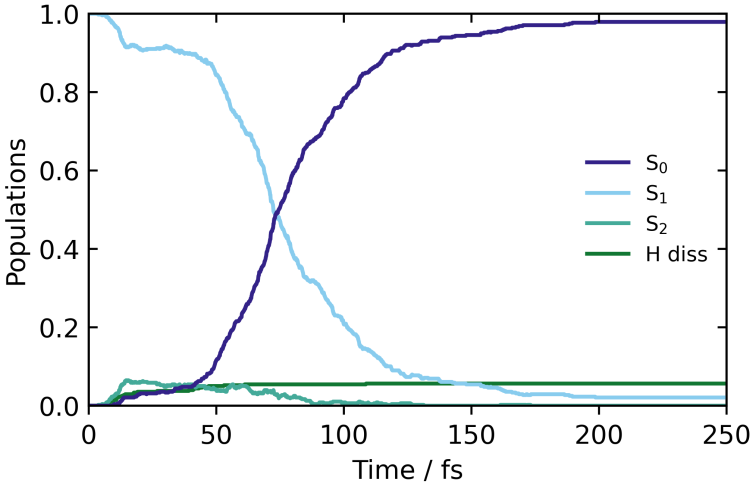

Figure 3.9: Classical populations of the ground and two excited states, of CP, over the time it takes for the trajectories to populate the ground state.

~1% of the total ensemble, and explain why the S_1 population does not decay fully to zero at longer timescales.

3.3.3.2 Formation of bicyclo[2.1.0]pentene

In order to track the number of trajectories that form the BP structure, two internal coordinates were monitored over the time of the dynamics simulations, namely the $C_1{-}C_4$ bond distance and the $C_1{-}C_5{-}C_4$ bond angle. These two internal coordinates change significantly in BP compared to the CP geometry. Comparing the ground state equilibrium geometries of CP and BP, the $C_1{-}C_4$ bond distance decreases from 2.36 → 1.54 Å and the $C_1{-}C_5{-}C_4$ bond angle decreases from 103.4 → 60.7°, respectively. The $C_1{-}C_4$ bond distance for short and long timescale dynamics is shown in Fig. 3.10 (a). In the short timescale dynamics, up to 250 fs, there are oscillations around the ground state equilibrium bond distance for the first 50 fs, followed by a splitting in the trajectories at around 75-125 fs, which is within the time frame for the $S_1 \rightarrow S_0$ population transfer (Fig. 3.9). At 75 fs, when half of the population in S_1 has been transferred to S_0, the bond distance in most trajectories is in the range of 2 to 2.25 Å, which correlates to the trajectories being in a geometry similar to the S_1/S_0 MECI with a bond distance of 2.06 Å.

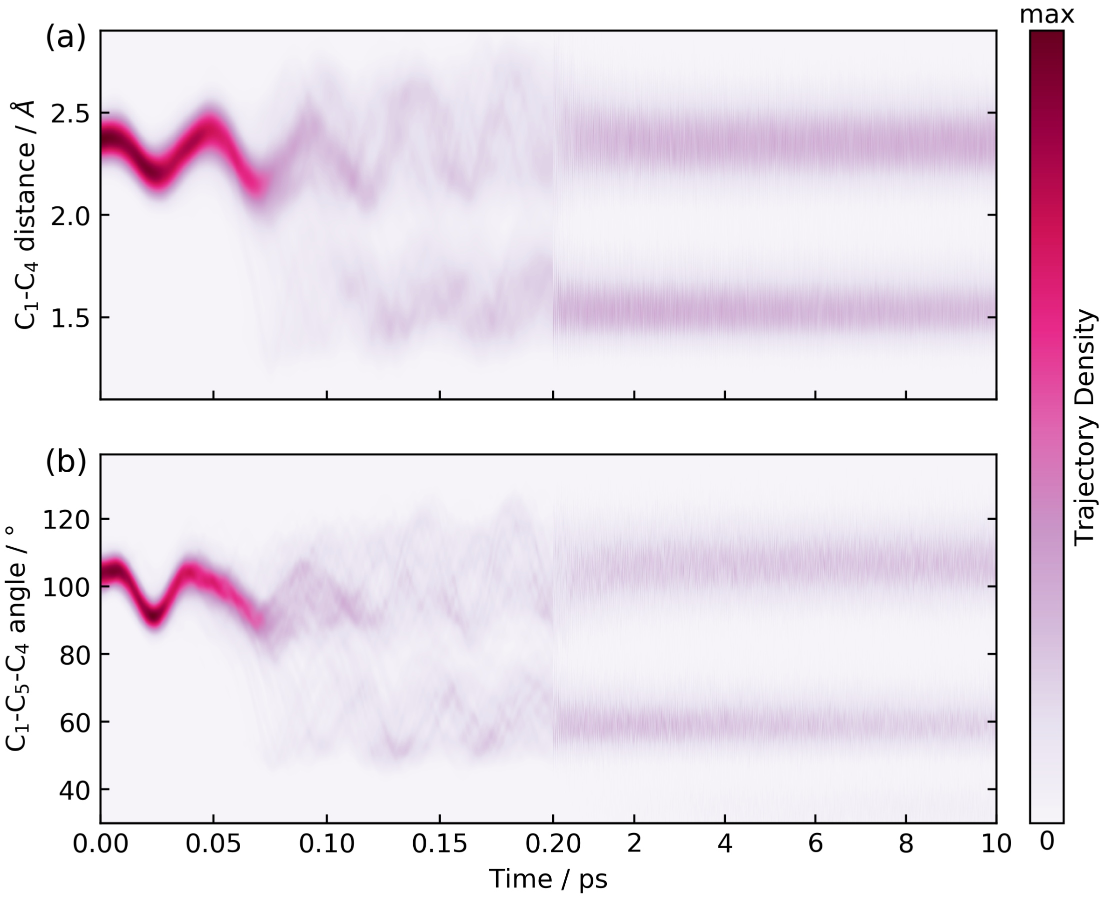

Figure 3.10: Time dependence of the $C_1{-}C_4$ bond distance (a) and the $C_1{-}C_5{-}C_4$ bond angle (b) during the dynamics simulations. Note that the scale on the axis changes after 0.2 ps, in order to show more of the detail for the early-time dynamics.

Figure 3.10 (a) also shows the time dependence of the $C_1{-}C_4$ bond distance on longer timescales, up to 10 ps. From this convolution plot, it can be seen that there is a clear separation, where trajectories are either in a geometry with a $C_1{-}C_4$ bond distance centred around ~1.6 or 2.4 Å, corresponding to either BP or CP, respectively. Therefore, it can be concluded that there are two possible pathways for the trajectories to follow: one that leads to a CP like geometry and one where the BP photoproduct is formed. In addition, analysis of the trajectories that lead to CP-like geometries on the electronic ground state, reveals hydrogen shift reactions, in agreement with Fuß *et al.* [123]. However, in Fuß's prediction these two different pathways are accessed *via* two different S_1/S_0 CIs. In contrast, only one CI seam has been located with XMS(3)-CASPT2(4,4)/cc-pVDZ and from analysis of the branching plane around the MECI, shown in Fig. 3.4, the direction of approach on S_1 may determine, which photoproduct is formed. Nevertheless, upon examination of the geometry at the point where a hop occurs from S_1 to S_0, in each of the trajectories, a general trend is observed, where the geometries that are most similar to the MECI, favour the formation of BP on the ground state. Moreover, the geometries, which have a more distorted ring structure compared to the MECI, form CP-like structures and lead to a hydrogen shift on the ground state. However, there is no particular internal coordinate that induces this distortion. It is also worth noting that these hopping geometries still retain a geometry resembling the S_1/S_0 MECI.

Furthermore, little trajectory density is observed between the two different product bands centred at either 1.6 or 2.4 Å, over long timescales in Fig. 3.10, indicating a very small degree of interconversion. In fact, only five trajectories interconvert, which are attributed to the back reaction from BP to CP on the hot ground state, and this only occurs after 6 ps. Therefore, the number of trajectories that follow each of the pathways is approximated by using a cutoff central bond distance of 2.0 Å to separate the two geometries. Using this metric, 44% of trajectories are found to follow the pathway that forms the BP structure, *via* an electrocyclisation reaction, and 55% of the trajectories follow the CP pathway that leads to a hydrogen shift or H dissociation. This ratio differs to the branching ratio stated by Fuß *et al.*, where 80% followed the hydrogen shift pathway and 20% followed the electrocyclisation pathway leading to BP [123]. Although these branching ratios are different, the results are in qualitative agreement with regards to the dominant pathway and photoproduct.

Tracking the time-dependence of the $C_1{-}C_5{-}C_4$ bond angle throughout the simulations, which can be seen in Fig. 3.10 (b), produces an almost identical plot to the $C_1{-}C_4$ bond distance plot, shown in Fig. 3.10 (a). The $C_1{-}C_5{-}C_4$ angle exhibits the same distinct difference between the BP and CP geometries and, therefore, again two separate bands form, with populations centred at 105° and 60°, respectively. Hence, the branching ratio between the two pathways can be calculated using a central cutoff bond angle of 80°, which results in identical branching ratios to those quoted for the $C_1{-}C_4$ bond distance.

3.3.4 Ground state reactions

The dynamics simulations show that there are two distinct pathways that the trajectories follow: either one that leads to a hydrogen shift, where the molecule is in a CP-like geometry, or one that forms the BP structure *via* an electrocyclic reaction. As shown in Fig. 3.10, there is very little interconversion between these pathways up to 10 ps. In addition, Fuß *et al.* predicted a time constant of 19 ps for the thermal back reaction from BP to recover CP on the hot ground state [123]. As the simulations only span out to 10 ps, RRKM theory is used to estimate this time-constant for the back reaction, which requires that the transition state is identified.

To locate the TS for the thermal back reaction, the ground state geometries of BP and CP were firstly optimised at the PBE0/def2-TZVP level of theory. The MEP between these two geometries was computed using the nudged elastic band approach at the PBE0/def2-SVP level, and the highest-energy geometry was used as an initial guess geometry for the optimisation of the TS. The optimised TS structure, computed at the PBE0/def2-TZVP level, contains one imaginary frequency at $-347.78\ \text{cm}^{-1}$, which corresponds to the opening and closing of the four-membered ring between C_1 and C_4, and is included in Fig. 3.11 (a). An IRC pathway, which follows the reaction coordinate associated with the imaginary frequency in the forward and reverse directions, was computed to confirm the nature of this TS. The reverse direction pathway leads to the BP minimum and the forward direction leads to the CP minimum, confirming that the correct transition state has been located. The reaction profile for this back reaction is shown in Fig. 3.11 (a) and has been constructed by computing MEPs between each minima and the TS. From the BP minimum, there is a relatively large energy barrier of 1.70 eV to overcome for this thermal reaction to occur.

The time constant for this back reaction is estimated using RRKM theory, where the sum and density of states are evaluated classically using the vibrational

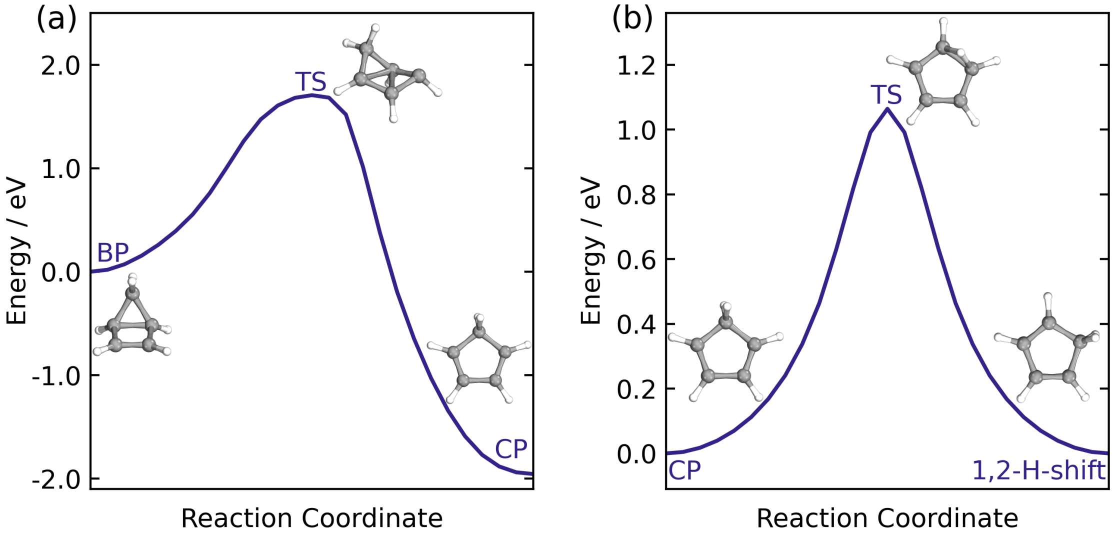

Figure 3.11: Minimum energy pathways (MEPs), computed at the PBE0/def2-TZVP level of theory using the nudged elastic band approach, from the transition states to each of the minima for both of the reactions that occur on the ground state: the back reaction from BP to CP (a) and the 1,2-hydrogen shift (b).

frequencies and ZPEs of the BP and TS structures, calculated using the PBE0/def2-TZVP level of theory. Additionally, the internal energy is approximated as the sum of the ZPE of BP plus the central excitation energy (5.1 eV) used in the dynamics simulations. Using these approximations in the RRKM formula yields a time constant, $\tau_{BP} = 18.76$ ps for the thermal back reaction from BP to CP on the hot ground state. This is almost identical to the 19 ps time constant reported by Fuß *et al.* [123], and is consistent with the five trajectories seen to revert to CP during the 10 ps of simulations. A larger fraction of the trajectories would be expected to revert if the simulations were extended to around 20 ps.

In addition to the pathway that forms BP *via* an electrocyclisation reaction, another pathway involves the molecule in the CP geometry and a hydrogen shift on the hot ground state. Here, Fuß *et al.* infer the presence of a 1,3-sigmatropic hydrogen shift from the deuterium effect [123], however, throughout the dynamics simulations, only 1,2-hydrogen shifts are observed, although sequential 1,2-hydrogen shifts in multiple trajectories are seen, where the hydrogen migrates to the carbon atom equivalent to a 1,3-hydrogen shift. Furthermore, these 1,2-hydrogen shifts occur readily in the ensemble of trajectories that follow this pathway. Therefore, to explain this observation, the TS between CP and the 1,2-hydrogen shift product was optimised at the PBE0/def2-TZVP level of theory. The optimised geometry, shown in Fig. 3.11 (b), contains one imaginary frequency at -1101.48 cm^{-1}, corresponding to the migration of the hydrogen from C_5 to C_1, hence displaying a 1,2-hydrogen shift. Again, the TS was validated by an IRC calculation and the reaction profile was constructed by computing MEPs between each minima and the TS, and can be seen in Fig. 3.11 (b). The energy barrier for the 1,2-hydrogen shift reaction is 1.05 eV, from CP, which is about half of the barrier for the back reaction from BP to CP. The difference in energy barriers between the two ground state processes explains why the hydrogen migration is seen on shorter timescales compared to the back reaction from BP to CP during the simulations.

The time constant for the 1,2-hydrogen shift process on the ground state has also been estimated using RRKM theory. The vibrational frequencies and ZPE of the CP and TS structures, calculated at the PBE0/def2-TZVP level, were used, noting that the actual geometry on the hot ground state will be different from the ground state equilibrium geometry of CP, and that this is an approximation. This calculation yields the time constant $\tau_H = 4.75$ ps. In comparison to τ_{BP}, the τ_H is much shorter, which validates the observation that the hydrogen shift occurs much more readily than the back reaction from BP to CP on the hot ground state. However, the 1,2-hydrogen shift in the simulations occurs even faster, at approximately 1 ps. This discrepancy may be due to multiple factors, including the approximation where the geometry of the molecule on the hot ground state has been used as the ground state minimum energy geometry, making the calculated time constant an upper bound on the correct value.

3.3.5 Ultrafast X-ray scattering

In order to compare theory to UXS experiments, which have now been performed [150], the experimental signals predicted by the theory and simulations have been modelled. Firstly, the dominant signal due structural dynamics is examined, and can be modelled at the level of the IAM. Secondly, the accuracy of the IAM is investigated and what further information can be extracted *via* more detailed analysis.

The results are shown without convolving in time because it was expected that the experiment would be carried out with X-ray pulses that are quite short in comparison with the timescale for nuclear dynamics. Furthermore, the signals are shown for 100% excitation, whereas in actual experiments, one optimises the intensity of the pump in the interaction region to maximise the excitation fraction while retaining single-photon excitation and avoiding multiphoton effects, which typically limits the excitation fraction to 1–5%. Signatures of too-high pump intensities include ionisation of the target, which can be identified *via* a characteristic dip in the small-q signal [152]. Finally, for convenience, the momentum transfer is denoted by q rather than $\tilde{q}$ that acts as a reminder of the Waller–Hartree approximation, as discussed in Section 2.9.1. The calculated signals are represented as percent differences to match the experimental signals [153]. The percent difference has the advantage that many systematic errors not linked to the excitation are cancelled out. Moreover, it also emphasises changes in the target relative to the ground state equilibrium and improves the visualisation of the signal at large q-values. The form of the percent difference signal, $\Delta\%I(q,t)$, is,

$$\Delta\%I(q,t) = 100 \times \frac{I(q,t) - I_{\mathrm{ref}}(q)}{I_{\mathrm{ref}}(q)}, \tag{3.2}$$

where $I(q,t)$ is the signal at time t and $I_{\mathrm{ref}}(q)$ is the reference signal corresponding to the target in its un-pumped equilibrium ground state at $t \ll 0$ [153].

3.3.5.1 Mapping structural dynamics

The time-dependent percent difference signal for the ensemble of trajectories is calculated using the IAM and is shown in Fig. 3.12 (a). On short timescales, $\lesssim 200$ fs, distinct signatures of the coherent vibrational motion can be seen. Based on the analysis of the simulations in Section 3.3.3, the ensemble of trajectories have been separated into those that form BP and those that yield CP-like structures. The scattering for these two pathways, in the form of their time-dependent percent

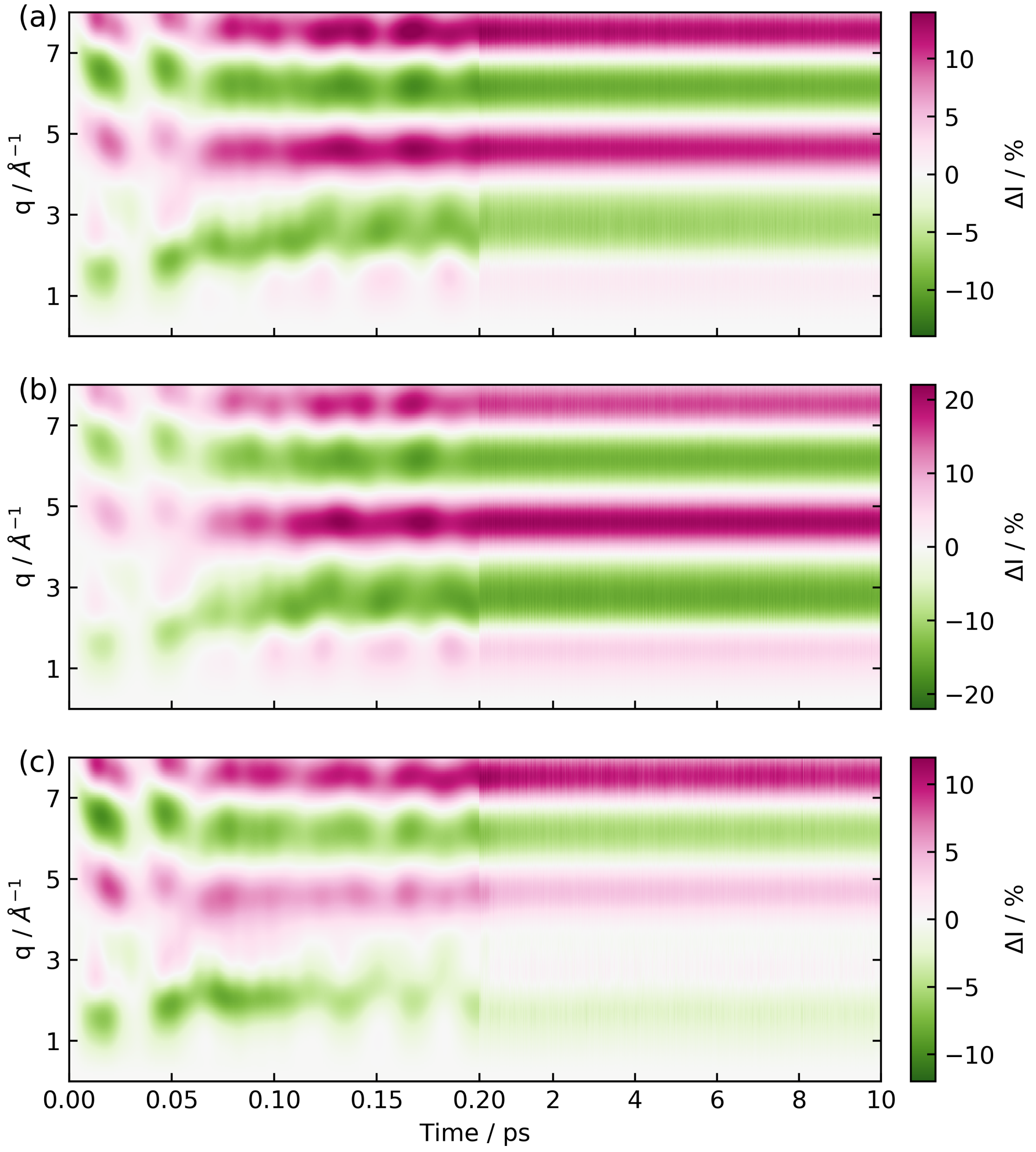

Figure 3.12: Time-dependent percent difference scattering signals during the dynamics simulations, calculated using the independent atom model (IAM), for the total ensemble of trajectories (a), the BP trajectories (b), and the CP trajectories (c). Note that the scale on the axis changes after 0.2 ps, in order to show more of the detail for the early-time dynamics.

differences, is shown in Fig. 3.12 (b) and (c), respectively. Comparing these two plots, it is evident that the dynamics for the two pathways is nearly identical up to $t \approx 50$ fs, at which point the trajectories branch, leading to notable differences in the scattering patterns. From then onward, the two pathways have somewhat similar bands at high q, displaying three bands in the region $5 < q < 8$ Å^{-1}, albeit with sufficient differences to separate them in a careful analysis of the combined scattering pattern. More importantly, the two patterns are quite distinct for $q < 4$ Å^{-1}, indicating that the low q region is particularly sensitive to which photoproduct is formed. Generally, it should be noted that the overall intensities in (b) are greater than in (c), reflecting that the BP photoproduct has a geometry, which differs more from the initial $t < 0$ molecular reference geometry than the hot CP. The information on the structural dynamics contained in the signal can be retrieved for instance *via* either forward optimisation trajectory-fitting [154–158] or million-structure type analysis [32, 159, 160].

At longer times, 2-10 ps, the signatures of the dynamics in the scattering patterns are less distinct due to more subtle changes in intensity indicative of the dispersion of the wave packet [104, 156, 161] and increasingly statistical (thermalised) dynamics. The scattering in this region can be harvested for information on the overall composition and changes in populations *via* kinetic models combined with representative scattering patterns for different products [27, 152, 162]. In fact, the scattering patterns shown in Fig. 3.12, were later used to fit the experimental X-ray scattering signal at longer time delays in Ref. [150], which will be discussed later.

3.3.5.2 Electronic effects

The effects on the scattering due to the electronic structure, which are absent in the IAM approximation, are considered by calculating the total scattering directly from the *ab initio* electronic wave functions using a previously developed computational framework [97, 98, 163, 164]. As these computations are expensive, the *ab initio* scattering has only been computed for two rather select geometries, CP and BP, as well as the LIIC pathway shown in Fig. 3.5, for illustrative purposes. Such representative calculations can be quite useful both for scattering and photoelectron signals [156, 165, 166].

Firstly, the accuracy of the IAM model is investigated by calculating the percent difference between the total IAM scattering and the isotropic ground state scattering as a function of q, which is calculated using the expression,

$$\Delta\%I(q,\mathbf{R}_{\mathrm{x}}) = 100 \times \frac{I_{\mathrm{tot}}^{\mathrm{IAM}}(q,\mathbf{R}_{\mathrm{x}}) - I_{\mathrm{tot}}^{\mathrm{S}_0}(q,\mathbf{R}_{\mathrm{x}})}{I_{\mathrm{tot}}^{\mathrm{S}_0}(q,\mathbf{R}_{\mathrm{x}})}, \tag{3.3}$$

at a specific molecular geometry of $\mathbf{R}_{\mathrm{x}}$. The results for the CP and BP geometries are shown in Fig. 3.13 (a). The largest difference between the IAM and *ab initio* scattering calculated from the molecular wave function occurs in the region of $q \in [2, 4]$ Å^{-1} for both geometries, with the IAM underestimating the signal by ~9% at 3 Å^{-1}. At larger q, in the range $q \in [5, 6]$ Å^{-1}, the IAM overestimates the total scattering by still a noticeable ~4% for CP and ~3% for BP. These discrepancies are on the same order of magnitude as those observed in other molecules [99, 100, 102, 163] and indicate that detailed analysis of high-quality experimental data should involve the usage of *ab initio* methods to predict the scattering.

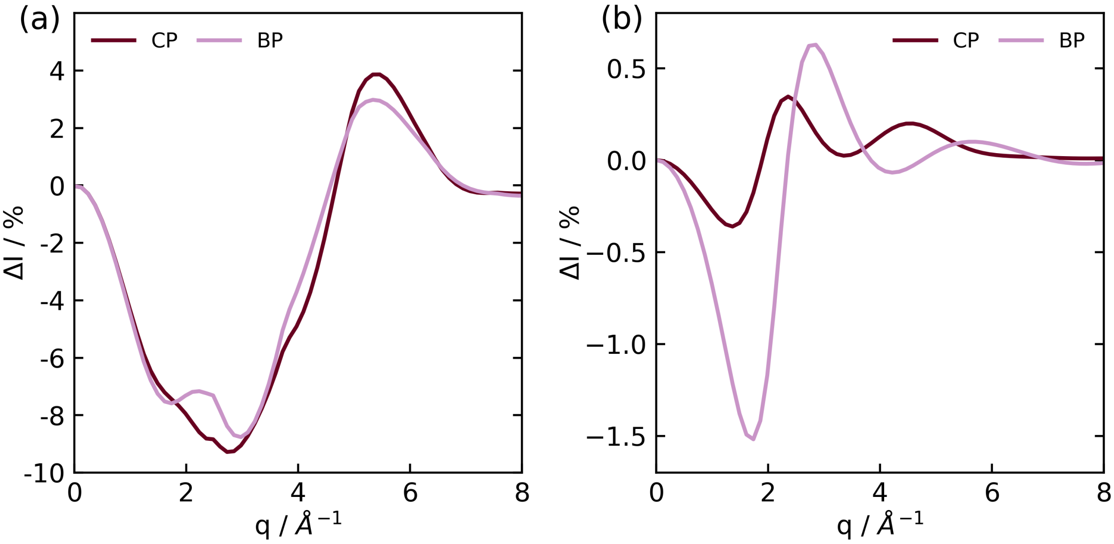

Figure 3.13: The percent difference between the IAM and the *ab initio* scattering signal for the ground electronic state S_0, calculated according to Eq. (3.3) at the CP and BP geometries (a), and the percent difference in the scattering from the first excited electronic state S_1, as compared to the S_0 ground state, calculated using Eq. (3.4), also at the CP and BP geometries (b).

Subsequently, the difference in scattering between the ground electronic state S_0 and the first excited state S_1 is investigated at a fixed geometry for both CP and

BP. The difference in $S_0 \rightarrow S_1$ is of particular interest since these two electronic states dominate the photoexcited dynamics. The percent difference between S_1 and S_0 scattering at a specific molecular geometry $\mathbf{R}_\mathrm{x}$ is calculated using,

$$\Delta\%I(q,\mathbf{R}_\mathrm{x}) = 100 \times \frac{I^{\mathrm{S}_1}_{\mathrm{tot}}(q,\mathbf{R}_\mathrm{x}) - I^{\mathrm{S}_0}_{\mathrm{tot}}(q,\mathbf{R}_\mathrm{x})}{I^{\mathrm{S}_0}_{tot}(q,\mathbf{R}_\mathrm{x})}, \tag{3.4}$$

which is shown in Fig. 3.13 (b) for CP and BP. Although the main contribution to the S_1 state at either geometry is the $\pi\pi^*$ electronic configuration, the effect of scattering from S_1 compared to S_0 is more prominent in the BP geometry at $q < 4$ Å^{-1}. This reflects differences in the configuration interaction vectors for the two molecules, where the S_1 state is composed of 96% of the $\pi\pi^*$ configuration in CP, compared to 94% in BP and hence, demonstrates the effect of the wavefunction on the scattering signal.

As an approximation of the *ab initio* scattering across the entire reaction path, the percent difference signal for the ground state S_0 is calculated along the LIIC pathway from CP to the S_1/S_0 MECI, and then onward to BP, as shown in Fig. 3.14 (a). To emphasise the structural dynamics, albeit now using the *ab initio* S_0 scattering rather than the IAM used in Section 3.3.5.1, this is calculated as,

$$\Delta\%I(q,\mathbf{R}_\mathrm{x}) = 100 \times \frac{I^{\mathrm{S}_0}_{\mathrm{tot}}(q,\mathbf{R}_\mathrm{x}) - I^{\mathrm{S}_0}_{\mathrm{tot}}(q,\mathbf{R}_\mathrm{CP})}{I^{\mathrm{S}_0}_{\mathrm{tot}}(q,\mathbf{R}_\mathrm{CP})}, \tag{3.5}$$

where $\mathbf{R}_\mathrm{x}$ are geometries along the LIIC pathway and the CP geometry $\mathbf{R}_\mathrm{CP}$ is used as the reference. The percent difference signal becomes more intense along the pathway as the molecule distorts away from the CP geometry along the LIIC, emphasising the effect of molecular geometry on the scattering signal. The signal is continuous along the LIIC pathway, however, the bands shift in different directions as the coordinate for the LIIC pathway changes at the MECI.

Finally, the effect of electronic structure on the scattering signal is examined, by comparing the scattering from the S_1 and S_0 electronic states along the LIIC path, using the S_0 ground state of CP as a reference,

$$\Delta\%I(q,\mathbf{R}_\mathrm{x}) = 100 \times \frac{I^{\mathrm{S}_1}_{\mathrm{tot}}(q,\mathbf{R}_\mathrm{x}) - I^{\mathrm{S}_0}_{\mathrm{tot}}(q,\mathbf{R}_\mathrm{x})}{I^{\mathrm{S}_0}_{\mathrm{tot}}(q,\mathbf{R}_\mathrm{CP})}, \tag{3.6}$$

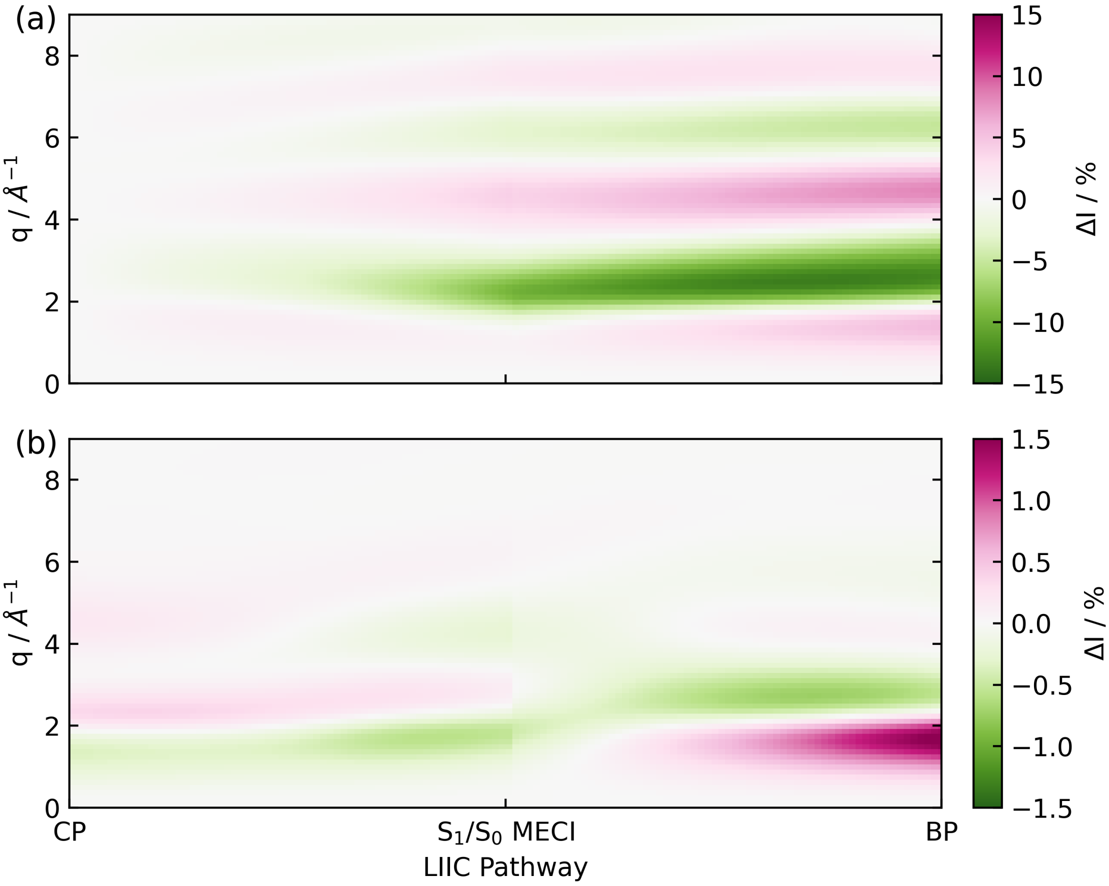

Figure 3.14: The effect of molecular geometry on scattering evaluated using the S_0 ground state *ab initio* scattering and Eq. (3.5), along the entire LIIC pathway (a), and, finally, the difference in scattering from the S_1 excited state as compared to the S_0 ground state along the LIIC pathway, calculated using Eq. (3.6) (b)

to compute the percent difference signal shown in Fig. 3.14 (b). As discussed elsewhere, this is an elegant way to isolate the contribution to the scattering signal due to electronic effects [27]. The signal is larger at low q, especially after the S_1/S_0 MECI, moving towards to the BP geometry. Although the percent difference signal between S_1 and S_0 is small, it may be within the resolution of future experiments and if so, could be used to assign excited state populations directly from the scattering signal [167]. As an aside, it should be noted that the signal appears to be continuous from CP to the S_1/S_0 MECI, and then from the MECI to BP, however, there is an apparent discontinuity that appears at the MECI. This reflects the combined effect of rapid changes in the wavefunction at the conical intersection and the sharp change in the direction of the molecular internal coordinates at the MECI for this LIIC.

3.3.6 Comparison to experiment

From recent UXS experiments of CP, direct evidence of the formation of the BP photoproduct was observed, following optical excitation at 243 nm [150]. For analysis of the experimental scattering signal and determination of the photoproducts, Huang *et al.* used the scattering signals for the BP and CP trajectories, shown in Fig. 3.12 (b) and (c), calculated with the IAM to fit the signals at different time delays. Firstly, from these fits a time constant for the formation of BP was determined to be 88 ± 10 fs, which can be related to the decay of the S_1 state and is in excellent agreement with the findings from the dynamics simulations as S_1 decays by half in around 75 fs.

At a first glance, the IAM scattering for the ensemble of trajectories shown in Fig. 3.12 (a) matches well with the experimental signal, with bands located in similar regions of q. However, from analysis of the individual contributions of the photoproducts to the signal, the experiments predict a larger proportion of BP formation compared to CP, where about 80% BP is seen at 1 ps [150]. This is in contrast to the simulations, in which only 44% of the trajectories form BP on the ground state. Additionally, in the experimental signal, there is a feature at low q ($q \approx 1$) attributed to bond breaking and hence, Huang *et al.* predict that there is a minor channel leading to ring-opened structures on a subpicosecond timescale [150], which is absent in the dynamics simulations. Despite the difference in photoproduct ratios between experiment and theory, the theoretical scattering pattern for the vibrationally hot BP trajectories has been shown to match well with the experimental signal, in the regions where there is 80% BP and, therefore, this gives confidence that the individual pathways are described well in the simulations.

Finally, a time constant of 21 ± 3 ps for the thermal back reaction from BP to CP on the hot ground state is experimentally determined [150]. This is in very good agreement with the calculated time constant of 18.76 ps using PBE0/def2-TZVP and RRKM theory, and validates why only six trajectories are seen to interconvert in the simulations since they were only run for 10 ps.

3.4 Conclusion

The simulations of photoexcited CP reveal details of the mechanism, including the presence of a conical intersection seam which guides the outcome of the short-time dynamics towards either CP or BP depending on how the wave packet enters the conical intersection seam. The simulations also indicate H-atom dissociation as a minor reaction path. At longer times, there appears to be a slower conversion from BP to CP on the electronic ground state, for which a TS has been identified. The rate predicted by RRKM theory for this ground state process appears to be congruent with both simulations and previous experiments. This also demonstrates a progression from short-time coherent dynamics, governed by dynamics through a conical intersection, to statistical long-time behaviour for the reaction.

UXS scattering signals have been predicted to compare to recent experiments. Although the effects due to the electronic structure are subtle throughout, it is sufficiently large that is might be observed in future high-repetition experiments at LCLS-II that are expected to have good resolution and excellent signal to noise. This would provide an opportunity to detect the electronic state and populations alongside the dynamics, in a similar manner to what was done recently in UED [167]. In a broader perspective, one of the advantages of scattering over spectroscopy is that there are no dark states and that these experiments '*see everything*'. However, X-ray scattering is not very sensitive to H-atoms, which scatter weakly. For this specific aspect, electron diffraction has an advantage over X-ray scattering [168], and currently, these simulations are being used to interpret new UED experiments. Overall, it is clear that the electronic and nuclear dynamics in photoinduced processes, such as the one simulated here, is complex, and that experimental mapping of the process would benefit greatly from having a range of observables obtained by complementary techniques, for instance by combining the scattering data with time-resolved photoelectron or X-ray absorption spectra [166, 169].

4
Azanaphthalenes

Sections of this chapter have been reproduced from Ref. [170] with permission from Springer Nature.

4.1 Introduction

Aromatic heterocycles containing nitrogen atoms (aza-aromatics) are common motifs in many biomolecules, for example the purine and pyrimidine DNA bases. In particular, azanaphthalenes are nitrogen containing bicyclic aromatic compounds and have a wide range of potential useful applications such as photosensitisers [171] and photovoltaics [8, 9] due to the fact that bicyclic species provide more potential for systematic variation than their related monocyclic counterparts.

Recently, TAS experiments were performed on the six azanaphthalene systems shown in Fig. 4.1, namely quinoline, isoquinoline, quinazoline, quinoxaline, 1,6-naphthyridine and 1,8-naphthyridine. These experiments were performed in the group of Professor Dave Townsend at Heriot-Watt University. Quinoline and isoquinoline have a single nitrogen atom centre at two different positions in the ring, quinazoline and quinoxaline have two nitrogen atom centres at different positions in the same ring, and finally, 1,6- and 1,8-naphthyridine have two nitrogen atom centres with one per ring. Of particular interest is how the relative position of the nitrogen

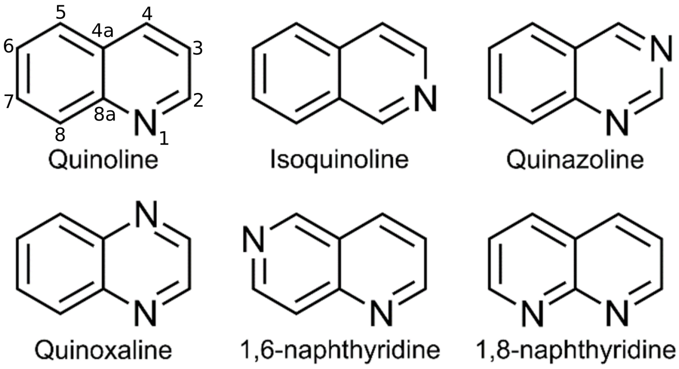

Figure 4.1: Schematic chemical structures of six azanaphthalene molecules considered in this study. Quinoline and isoquinoline have a single nitrogen atom centre at two different positions in the ring, quinazoline and quinoxaline have two nitrogen atom centres at different positions in the same ring, and 1,6- and 1,8-naphthyridine have two nitrogen atom centres with one per ring. The atom numbering in the ring system is also indicated.

atom influences the competing pathways in the dynamics. This study excluded diazanapthalenes with direct N−N bonds since these structures are not typically observed in nature, most likely due to a lack of naturally occurring hydrazine species, which are the common building blocks for their synthesis.

The TAS experiments studied these six molecules in a hexane solution, where the molecules were excited at 267 nm and then probed in the region of 340-750 nm. This probe bandwidth allows for the detection of the low-lying triplet state absorption band present in these bicyclic species. From the experiments, three lifetimes were determined for each of the molecules, where the τ_1 and τ_2 values

Table 4.1: Summary of fitted lifetimes from the TAS experiments for all six molecules using 267 nm excitation under hexane solvation. Also included is a summary of the theoretically determined electronic structure trends and key parameters which help rationalise the τ_1 and τ_2 lifetimes.

	τ_1 / ps	τ_2 / ps	S_3/S_2 min present?	Barrier height to S_1/S_0 MECI / eV	SOC at S_1/T_2 MECP / cm^{-1}
Isoquinoline	2.8	22	No	0.06	0.02
Quinoline	2.8	39	No	0.09	6.92
Quinazoline	11.2	167	Both	0.29 & 0.50	4.93
Quinoxaline	4.8	57	No	0.51	8.68
1,6-Naphthyridine	4.0	37	No	0.1 & 0.16	3.47 & 9.43
1,8-Naphthyridine	5.2	61	No	0.25	6.31

are shown in Table 4.1. The τ_1 lifetimes describe a relatively fast decay of the initially populated excited $\pi\pi^*$ state to the S_1 surface, whereas the τ_2 values are ascribed to the sequential decay of the S_1 state. The τ_3 values, not included in Table 4.1, are determined from the signal in the excited state absorption spectrum around 400 nm, however, this feature persisted past the 1.4 ns observation window, and hence, a lower bound lifetime of 50 ns was quoted for all six molecules. This signal is characteristic of the triplet-triplet absorption band and therefore τ_3 is attributed to the lifetime in the lowest triplet state. Additionally, ISC quantum yields were calculated for isoquinoline, quinoline and quinoxaline and are estimated as 0.02 ± 0.01, 0.11 ± 0.02 and 0.25 ± 0.03, respectively. Thus, it is concluded that IC and ISC are competing processes.

From these experiments and previous experiments, there is no clear correlation between the S_1 lifetime and ISC probability. However, this has been elucidated for isoquinoline and quinoline, in a previous theoretical study, where time-dependent density functional theory was used to rationalise the differences between molecules in terms of the energy barriers for the IC pathways and strength of the SOC interaction [172]. A further study on isoquinoline highlighted the role of the C−N−C angular coordinate in mediating vibronic coupling between the first two excited singlet states [173]. Furthermore, the low-lying excited states and ISC pathways in quinazoline and quinoxaline, have also been investigated using a coupled-cluster approach [174].

Nevertheless, there are no known theoretical studies, which investigate the photorelaxation pathways upon excitation into the second $\pi\pi^*$ state in the Franck-Condon region. Additionally, the pathways in the triplet manifold are unknown. Therefore, in this chapter, quantum chemical calculations are employed to the explain the lifetimes from the recent TAS experiments. The excited electronic states involved in the dynamics are mapped, allowing the experimental observations to be rationalised in a systematic manner across the entire series of six related molecules.

4.2 Computational methods

The ground state equilibrium geometries of all six molecules were optimised using SCS-MP2 and the excited state minima were optimised using SCS-ADC(2) [74, 75], with the cc-pVDZ basis set used throughout apart from the calculations of the vertical excitation energies, which were computed with SCS-ADC(2)/aug-cc-pVQZ from the ground state equilibrium geometry optimised at the SCS-MP2/cc-pVDZ level of theory. Excitation energies are overestimated using the cc-pVDZ basis, and therefore, a larger basis set is used to obtain sufficiently accurate energies, to confirm the state excited at 267 nm. All calculations were performed in Turbomole 7.7 [134], which was interfaced with CIOpt [175] to locate MECIs at the SCS-ADC(2)/SCS-MP2 level of theory and minimum energy crossing points (MECPs) with SCS-ADC(2). TSs between excited state minima were identified by firstly computing a MEP between the two minima of interest. The highest-energy geometry was then used as an initial guess for the optimisation of the TS. The vibrational frequencies were calculated to confirm the optimised structure contained one imaginary frequency and finally, an IRC calculation was performed to validate that this optimised TS led to the correct minima. PE profiles were constructed by LIICs between the relevant points along the PESs. In the case of quinoline, quinazoline, 1,6- and 1,8-naphthyridine, MEPs were computed between the S_1 ($^1n\pi^*$) minima and the TSs connecting the minima to the S_1/S_0 MECIs, in order to eliminate an artificial barrier before the TS, produced by the LIIC.

Since SCS-ADC(2) is a single-reference method, it typically does not describe the regions around the S_1/S_0 MECIs correctly. To validate the SCS-ADC(2) results in these regions, the PESs later presented in Fig. 4.5, were benchmarked using XMS-CASPT2 [70] with the cc-pVDZ basis set. The XMS-CASPT2 calculations were performed in OpenMolcas v22.10 [143, 144] utilising an imaginary shift of 0.2 Hartree. A (12,11) active space is used for the calculations in isoquinoline and quinoline, while a (14,12) active space is used for quinazoline, quinoxaline, 1,6- and 1,8-naphthyridine. This (14,12) active space is depicted in the next chapter. For isoquinoline, quinoline, quinazoline, and quinoxaline, the calculations were state-averaged over the three lowest-lying singlet states. In contrast, for 1,6-naphthrydine, seven states were included, and for 1,8-naphthyridine, the calculations were performed with state averaging over eight states.

4.3 Results and Discussion

4.3.1 Vertical excitation energies

The vertical excitation energies for the first three excited states (S_{1-3}) in isoquinoline are shown in Table 4.2, as an example for the six molecules. The introduction of one or more nitrogen atoms into the naphthalene ring introduces a range of effects on the electronic spectrum. Firstly, it adds a set of $n\pi^*$ states, which typically fall in the same region as the lowest energy $\pi\pi^*$ states. These $n\pi^*$ states are generally dark in the one-photon spectrum, as is commonly observed for such transitions. Additionally, the higher electronegativity of the nitrogen atoms distorts the molecular orbitals of the underlying naphthalene structure, leading to subtler effects, such as shifts in the excitation energies of the electronic states.

The excitation energies have been computed in the gas-phase and using the conductor-like screening model (COSMO) as an implicit solvation model of hexane [176]. As shown below in Table 4.2, there are minimal differences between the

Table 4.2: Vertical excitation energies of isoquinoline obtained at the SCS-ADC(2)/aug-cc-pVQZ level of theory, from the ground state equilibrium geometry optimised at the SCS-MP2/cc-pVDZ level. These are calculated in the gas-phase and using COSMO.

State	Transition	E_{exc} / eV	f_{osc}	λ / nm
Gas-phase				
S_1	$\pi\pi^*$	4.26	0.026	291
S_2	$n\pi^*$	4.81	0.002	258
S_3	$\pi\pi^*$	4.90	0.062	253
COSMO				
S_1	$\pi\pi^*$	4.23	0.038	293
S_2	$n\pi^*$	4.82	0.003	257
S_3	$\pi\pi^*$	4.86	0.076	255

gas-phase and COSMO vertical excitation energies, with a red-shift of ∼2 nm observed, which is slightly smaller than the 5 nm seen experimentally. Furthermore, there is retention in state character between the two methods, and hence, all further calculations are performed in the gas-phase. However, from the COSMO energies, the state populated experimentally at 267 nm, is determined as the second optically bright $\pi\pi^*$ state, corresponding to S_3 in isoquinoline, quinoline, quinazoline and quinoxaline, and to S_4 in 1,6- and 1,8-naphthyridine. In 1,6- and 1,8-naphthyridine, the second $\pi\pi^*$ state lies above the second $n\pi^*$ state because the n orbitals in these molecules are much closer in energy compared to the equivalent orbitals in quinazoline and quinoxaline. As a result, the two $n \rightarrow \pi^*$ transitions are closer in energy in 1,6- and 1,8-naphthyridine. It is also worth noting that the electronic states retain the same character between basis sets and hence, the description with cc-pVDZ is qualitatively similar.

4.3.2 Photorelaxation pathways

In the following, the quantum chemical calculations are used to rationalise the experimental observations, mapping them onto features of the excited states such as MECIs, and energy barriers as well as MECPs and associated SOCs. The calculations explain the systematic variation in singlet lifetimes and the propensity for ISC observed experimentally. Table 4.1 includes a summary of the key features in the electronic structure that are linked to the experimental τ_1 and τ_2 lifetimes observed in the molecules. As discussed in Section 4.3.1, all molecules are excited to the second bright $\pi\pi^*$ state, which corresponds to S_3 in isoquinoline, quinoline, quinazoline and quinoxaline, and to S_4 in 1,6- and 1,8-naphthyridine. Therefore, to interpret the τ_1 lifetimes, the PESs for the S_3 and S_2 states (plus S_4 in 1,6- and 1,8-naphthyridine), shown in Fig. 4.3, were examined. Moreover, the trends in τ_2 lifetimes have been investigated through analysis of the S_1 PESs shown in Fig. 4.5 and the probability of ISC into the triplet manifold as these lifetimes are attributed to a combination of factors, namely barrier heights to the S_1/S_0 MECIs and the SOC values at the S_1/T_2 MECPs. Finally, the triplet state dynamics associated with a long τ_3 lifetime are analysed.

4.3.2.1 Photorelaxation to the S_1 surface (τ_1)

The ground state minimum energy geometries of all six molecules consist of a planar ring structure. Excitation at 267 nm into the bright $\pi\pi^*$ state (S_3 or S_4) induces geometrical changes in the plane of the aromatic ring, which accompanies photorelaxation to the S_1 surface. Moreover, this motion leading to S_1 corresponds to a nitrogen-centred ring in-plane bend, where the C−N−C bond angles change at different points along the overall reaction coordinate. An example of this geometrical change for quinazoline is shown in Fig. 4.2 (a).

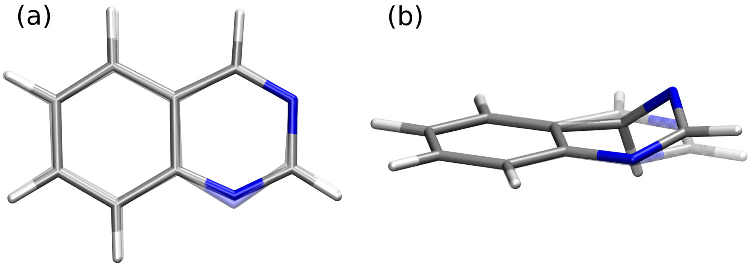

Figure 4.2: Representative geometrical changes in quinazoline, along the PESs, which occur in all six systems. Firstly, (a) shows changes in the C−N−C bond angles, due to the nitrogen-centred ring in-plane bend, that occurs along the PES. Secondly, (b) displays the typical out of-plane distortion, which occurs as the S_1/S_0 MECIs are approached from the S_1 ($^1n\pi^*$) minimum.

The most rapid decay from the initially excited state to the S_1 surface is observed in quinoline and isoquinoline, with a $\tau_1 = 2.8$ ps decay constant that is unaffected by the position of the single nitrogen atom centre. The LIICs in Fig. 4.3 show that both molecules form an effective funnel towards S_1 *via* two consecutive MECIs (S_3/S_2 and S_2/S_1), leading to a barrierless cascade from the initially excited S_3 state to the S_1 surface and the S_1 ($^1n\pi^*$) minimum. In both molecules, the S_3/S_2 MECI lies close to the FC region, with a similar C−N−C bond angle to the ground state equilibrium geometry, whereas the S_2/S_1 MECI has an increased bond angle, with a value between the FC region and the S_1 ($^1n\pi^*$) minimum geometries. Finally, it should be noted that the two S_1 minima ($^1\pi\pi^*$ and $^1n\pi^*$), in isoquinoline and quinoline, are accessible from the S_2/S_1 MECI, although only the $^1n\pi^*$ minimum is shown in Fig. 4.3 for simplicity.

Adding a second nitrogen atom slows down the dynamics. Firstly, 1,6- and 1,8-naphthyridine are considered, which both have one nitrogen atom per ring. These molecules are excited to the bright S_4 state, rather than S_3, but are otherwise similar to quinoline and isoquinoline, forming a barrierless funnel to the S_1 state as shown in Fig. 4.3. The resulting IC cascade is more efficient in 1,6-naphthyridine since only two MECIs are involved, firstly a S_4/S_3 MECI followed by a three-state $S_3/S_2/S_1$ MECI. This pathway requires smaller distortions of the molecular geometry as S_4/S_3 MECI has a very similar geometry to the ground state equilibrium geometry and in the three-state MECI both C−N−C bond angles increase slightly, which yields a shorter lifetime of 4 ps. In 1,8-naphthyridine, the barrierless pathway instead involves three consecutive MECIs: S_4/S_3, S_3/S_2, and finally S_2/S_1. This increases the lifetime to 5.2 ps as quite a significant increase in the C−N−C bond angles are required to reach the S_3/S_2 MECI from the S_4/S_3 MECI, which resembles the ground state geometry, and then a reversal of this geometry change is necessary to find the S_2/S_1 MECI, due to the fact it is located close to the S_4/S_3 MECI.

Finally, the pair of molecules quinoxaline and quinazoline with the nitrogen atom centres located in a single ring are examined. Compared to isoquinoline and quinoline, the dynamics are significantly slower and the topography of the excited PESs are more complicated, with two or more distinct decay pathways emerging in both molecules. Quinazoline has the largest τ_1 lifetime out of all six molecules at 11.2 ps, while quinoxaline is closer to 1,6- and 1,8-naphthyridine with $\tau_1 = 4.8$ ps, despite the more complex photorelaxation channel on the right-hand side (RHS) of the panel in Fig. 4.3, which proceeds over a small 0.1 eV barrier (an upper limit) and through a S_3/S_2 MECI, with significantly larger C−N−C bond angles, followed by the passage through a three state $S_3/S_2/S_1$ MECI accessed *via* a relatively large change in geometry as this three-state MECI has a geometry similar to the FC region. However, the second pathway, shown on the left-hand side (LHS) of the same panel, directly accesses the three-state MECI, and opens up a more immediate

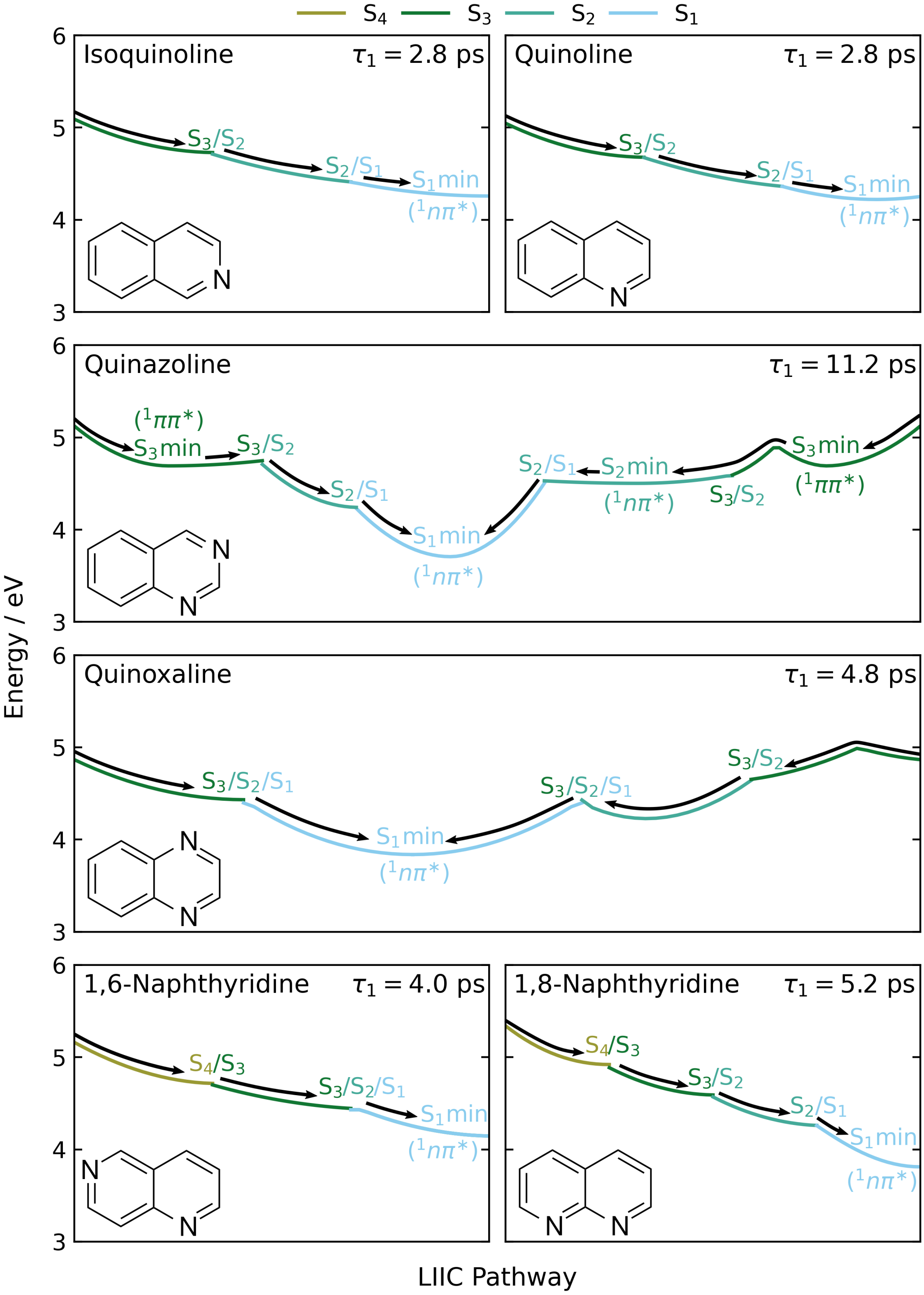

Figure 4.3: PE profiles of the photorelaxation pathways from S_3 (S_4 for 1,6- and 1,8-naphthyridine) onto the S_1 surface, for all six molecules, computed with SCS-ADC(2)/cc-pVDZ. The profiles have been linearly interpolated between MECIs and excited state minima. For clarity, only the active state involved along the pathway to the S_1 $(n\pi^*)$ minimum is shown and the ground state has been omitted. A figure including all excited states can be found in Appendix B.

route to the S_1 state, reminiscent of the funnels in 1,6- and 1,8-naphthyridine, and explains the faster dynamics in quinoxaline compared to quinazoline.

The slower dynamics in quinazoline may be attributed to the presence of distinct minima separated by small barriers on both the S_3 and S_2 PESs, which is in contrast to the other five molecules, where the minima coincide with the MECIs. The S_3 minimum is located close to the FC region, with a similar geometry, whereas the S_2 minimum contains a significantly larger $C_{8a}{-}N_1{-}C_2$ bond angle. Figure 4.3 shows the two main photorelaxation channels in quinazoline upon excitation into the S_3 state. The first channel, starting on the LHS, passes through the S_3 minimum and undergoes IC through a S_3/S_2 MECI onto the S_2 surface. From here, a barrierless transition onto S_1 through a S_2/S_1 MECI bypasses the S_2 minimum, with minimal geometrical distortions required. The second pathway, on the RHS of the panel, passes through the same S_3 minimum and then over a 0.2 eV energy barrier, noting that the barrier height is an upper bound as this pathway is constructed by linear interpolation. The molecule then reaches the S_2 minimum *via* a second S_3/S_2 MECI, with an increased $C_{8a}{-}N_1{-}C_2$ bond angle. This minimum is located near the S_2/S_1 MECI, which allows for subsequent decay to the S_1 state. Additionally, a third pathway is present and is accessed *via* a TS located 0.03 eV above the S_2 minimum and proceeds through the same S_2/S_1 MECI as the pathway on the LHS of Fig. 4.3, where the imaginary frequency of the TS is associated with the nitrogen-centred ring

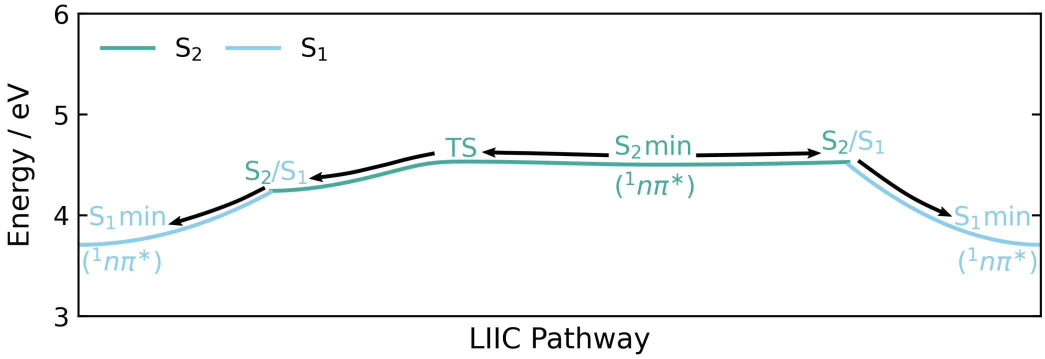

Figure 4.4: PE profile of the S_2 surface in quinazoline, which leads to the S_1 ($^1n\pi^*$) minimum, calculated with SCS-ADC(2)/cc-pVDZ. The PE profile has been interpolated between minima, the TS, and MECIs. For clarity, only the active state involved along the pathway to the S_1 ($n\pi^*$) minimum is shown and the ground state has been omitted.

in-plane bend. Both pathways from the S_2 minimum to the S_1 surface are shown Fig. 4.4. It is worth noting that the barrier height of the TS is almost identical to the energy required to access the S_2/S_1 MECI on the RHS, from the S_2 minimum, and hence, these routes are expected to be competing processes. Overall, in quinazoline the photorelaxation pathways are more complex due to the multiple MECIs, minima, and PE barriers, which all contribute to notably slower τ_1 dynamics.

In general, the molecules with one nitrogen atom in the naphthalene system and one nitrogen atom per ring exhibit notably similar PESs, as shown in Fig. 4.3. The primary difference between these sets of molecules is that 1,6- and 1,8-naphthyridine start on the S_4 state, compared to S_3 in isoquinoline and quinoline, as discussed in Section 4.3.1. These PESs are significantly simpler compared to those of quinazoline and quinoxaline, where both atoms reside in the same ring. The increased complexity and multiple pathways observed in these systems are likely due to stronger interactions between the two nitrogen atoms. Additionally, the reduced symmetry of quinazoline relative to quinoxaline allows for greater variations in the C−N−C angular coordinates, resulting in multiple minima and reaction pathways.

4.3.2.2 Photorelaxation of the S_1 state (τ_2)

Once the six molecules undergo photorelaxation to the S_1 state, the S_1 surface is then explored. Therefore, the trends in the τ_2 lifetimes are investigated by examining the features on the S_1 PESs. For IC, minima, TSs, and S_1/S_0 MECIs on the S_1 surfaces are located for all six molecules. The relevant LIICs are shown in Fig. 4.5 and are calculated between minima, TSs and MECIs, except that between the S_1 minimum and TS5, TS6, TS10 and TS11 in quinoline, 1,6-naphthyridine and 1,8-naphthyridine, where MEP calculations are performed instead, since the LIICs yield artificial maxima before the true TSs in those cases. The calculations show that all singlet photorelaxation pathways to the ground state proceed *via* the S_1 ($n\pi^*$) minimum. Interestingly, the motion on the S_1 surface corresponds to the same nitrogen-centred ring in-plane bend that accompanies decay from the S_3 (and S_4) to the S_1 surface, but with additional distortion out of the plane of the aromatic rings when approaching the S_1/S_0 MECIs. It is most likely that these out of plane distortions, shown in Fig. 4.2 (b) for quinazoline, are responsible for τ_2 being significantly slower compared to τ_1.

Competing with IC is ISC to the triplet manifold, where the propensity for ISC is investigated by locating MECPs between singlet and triplet states and by calculating the SOC at these geometries. From the computations, ISC is predicted to occur *via* a S_1/T_2 MECP for all six molecules and these MECPs are accessed without the molecules having to cross any specific barriers. Thus, the τ_2 lifetimes are attributed to a combination of PE barriers for reaching the S_1/S_0 MECIs and the SOC at the S_1/T_2 MECPs, which are summarised in Table 4.1.

As seen in Table 4.1, isoquinoline has the shortest τ_2 lifetime (22 ps) and displays a very small propensity to undergo ISC into the triplet state. The data presented in Fig. 4.5 indicates that isoquinoline has two S_1 minima, where one has $\pi\pi^*$ character and the other one has $n\pi^*$ character, which are likely populated equally after IC onto the S_1 surface. The $^1\pi\pi^*$ minimum is associated with a similar geometry to the FC region, while the $^1n\pi^*$ minimum is characterised by an increased C−N−C bond angle. An energy barrier of 0.14 eV from the $^1\pi\pi^*$ minimum must be overcome to access the $^1n\pi^*$ minimum, while the reverse process has a barrier of 0.05 eV. Once, in the $^1n\pi^*$ minimum, there is a small barrier of 0.06 eV to access the S_1/S_0 MECI, where atoms C_1 and N_2 distort out of the plane of the ring in opposite directions. Since the heights of both barriers from the $^1n\pi^*$ minimum are comparable, ground state relaxation and exploration of the S_1 surface are likely to compete, slowing the dynamics down. Furthermore, the S_1/T_2 MECP is located at the $^1\pi\pi^*$ minimum, but the SOC has a magnitude of only 0.02 cm^{-1} due to both the S_1 and T_2 states having dominant $\pi\pi^*$ character at this geometry. Given the absence of ISC and the known lack of fluorescence in this system, the decay of the S_1 state is therefore, predominantly *via* ground state re-population by IC.

Quinoline and 1,6-naphthyridine have similar τ_2 lifetimes of 39 and 37 ps, respectively, which are significantly longer than isoquinoline. As in isoquinoline, two minima exist on the S_1 surface in quinoline, and there is one accessible S_1/S_0

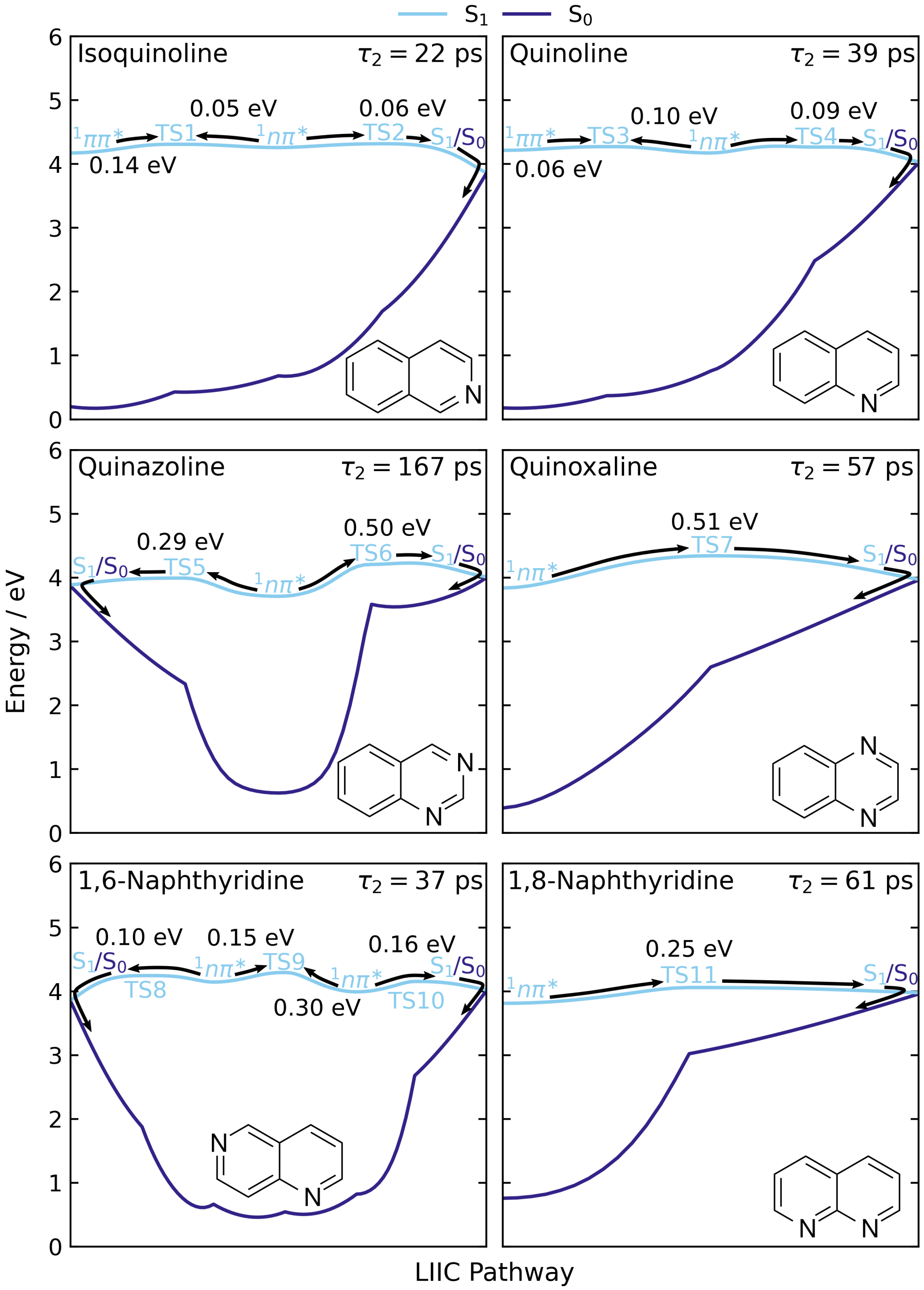

Figure 4.5: PE profiles along the S_1 surface leading to the S_1/S_0 MECIs, performed at the SCS-MP2/SCS-ADC(2)/cc-pVDZ level. These profiles have been computed using LIICs between excited state minima, the connecting TSs, and S_1/S_0 MECIs except between the S_1 ($n\pi^*$) minimum and TSs in quinazoline, 1,6- and 1,8-naphthyridine, where MEP calculations were performed. The S_1 minima are denoted by their dominant electronic character.

MECI, associated with distortion of the N_1 and C_2 atoms, from the $^1n\pi^*$ minimum. From this minimum, there is a barrier of 0.09 eV to access this MECI in addition to a barrier of 0.10 eV leading to the $^1\pi\pi^*$ minimum, which is shown in Fig. 4.5. The S_1/T_2 MECP lies 0.02 eV above the $^1n\pi^*$ minimum and has a SOC magnitude of 6.92 cm^{-1}. At this geometry, S_1 has $n\pi^*$ character and T_2 has mixed $\pi\pi^*/n\pi^*$ character, which gives rise to a sizeable SOC magnitude. The differences in energy barriers to access the ground state and in the SOC values rationalise the increase in τ_2 lifetime compared to isoquinoline. It should be noted that the S_1/T_2 MECP in quinoline lies along the pathway to the easily accessible S_1/S_0 MECI, and hence, population transfer to the ground state may affect the amount of ISC that occurs.

In contrast to isoquinoline and quinoline, three minima are located on the S_1 surface in 1,6-naphthyridine, one $^1\pi\pi^*$ minimum and two $^1n\pi^*$ minima. The latter connect to the S_1/S_0 MECIs, which both exhibit out of plane distortions, where either the N_1 and C_2 atoms or the C_5 and N_6 atoms distort. For clarity, only the two $^1n\pi^*$ minima are shown in Fig. 4.5, however, all three minima are accessible from the S_2/S_1 MECI. From the $^1n\pi^*$ minimum with an increased $C_5{-}N_6{-}C_7$ bond angle, there is a barrier of 0.10 eV *via* TS8 to access the respective S_1/S_0 MECI, which is akin to the barrier in quinoline. In addition, from the $^1n\pi^*$ minimum with an increased $C_{8a}{-}N_1{-}C_2$ bond angle, there is a barrier of 0.16 eV to the S_1/S_0 MECI, *via* TS10. Interconversion between the two $^1n\pi^*$ minima is unlikely as the barrier between them is larger from each direction than the barriers to the MECIs. For ISC, two S_1/T_2 MECPs were located, where the MECP near the $^1n\pi^*$ minimum with the larger barrier to the S_1/S_0 MECI has a large SOC value of 9.43 cm^{-1} due to the S_1 state having $n\pi^*$ character whereas the T_2 state has $\pi\pi^*$ character, likely leading to preferential ISC into the triplet manifold over relaxation to the ground state. A second S_1/T_2 MECP with a smaller SOC value of 3.47 cm^{-1} is located near the $^1n\pi^*$ minimum with a smaller barrier to the S_1/S_0 MECI. Hence, at this S_1 minimum, ground state relaxation is favourable over ISC. These two different photorelaxation pathways lead to a lifetime comparable to quinoline.

Quinoxaline has a τ_2 lifetime of 57 ps, which is similar to the lifetime in 1,8-naphthyridine (61 ps) and shorter than the lifetime in quinazoline (167 ps), despite having a significantly larger energy barrier of 0.51 eV from the S_1 ($^1n\pi^*$) minimum to the only accessible S_1/S_0 MECI. Quinoxaline only contains one S_1 minimum, as a consequence of symmetry and is characterised by two equally increased C−N−C bond angles compared to the FC region, while the S_1/S_0 MECI is associated with distortion of the N_1 and C_2 atoms. Although the barrier to the S_1/S_0 MECI is notably larger, the S_1/T_2 MECP lies only 0.07 eV above the S_1 minimum and has a large SOC value of 8.68 cm^{-1}, attributed to a change in character from S_1 ($n\pi^*$) to T_2 ($\pi\pi^*$). Thus, it is proposed that ISC into the triplet manifold is likely dominant over relaxation to the ground state, which is in broad agreement with previously reported literature at longer excitation wavelengths [177–179].

The similar τ_2 lifetime in 1,8-naphthyridine of 61 ps is attributed to a combination of factors. Firstly, from the S_1 ($^1n\pi^*$) minimum, there is a barrier of 0.25 eV to the only accessible S_1/S_0 MECI. This S_1 minimum is associated with an increase of only one of the C−N−C bond angles. Interestingly, the geometry where both C−N−C bond angles increase, corresponds to a TS. Furthermore, at the S_1/S_0 MECI, distortion occurs in the same two atoms as quinoxaline. As discussed above, the impact of this lower barrier height compared to quinoxaline is compensated by the stronger SOC in quinoxaline. The S_1/T_2 MECP located at the S_1 minimum in 1,8-naphthyridine has a SOC value of 6.31 cm^{-1}, again assigned to the change in character from S_1 ($n\pi^*$) to T_2 ($\pi\pi^*$). Therefore, as ISC into the triplet manifold is slower and the ground state is more accessible, this leads to a lifetime comparable to quinoxaline.

Finally, quinazoline displays by far the longest τ_2 lifetime (167 ps) amongst all six systems considered in this study. Although the molecule has two S_1/S_0 MECIs accessible from the only S_1 minimum of $n\pi^*$ character, with two increased unequal C−N−C bond angles, both are associated with large energy barriers. The first involves distortion of the molecular geometry at the N_1 and C_2 atoms and has a larger energy barrier of 0.50 eV. The second involves distortion at the N_3 and C_4

atoms with a barrier of 0.29 eV, which is larger than the barriers for all molecules except quinoxaline. At the same time, the SOC value at the S_1/T_2 MECP is 4.93 cm^{-1}, which is significantly smaller than both 1,8-naphthyridine (6.31 cm^{-1}) and quinoxaline (8.68 cm^{-1}) despite S_1 having dominant $n\pi^*$ character and the T_2 having dominant $\pi\pi^*$ character at this geometry. The result is a slow rate of ISC, in agreement with previous literature findings [177]. The net outcome of the slow rates of ISC and IC is a significantly longer lifetime in the S_1 state.

Overall, all the deactivation pathways from S_1 to the ground state involve out of plane motion around the nitrogen atom within the ring. From Fig. 4.5, it is evident that the position of the nitrogen atom influences the barrier heights. A clear trend is seen, where the energy barriers are higher when the nitrogen atom is adjacent to the bridgehead carbon atom. Considering the simplest case with a single nitrogen in the system, quinoline exhibits a higher barrier than isoquinoline due to its slightly more pyramidalised bridgehead carbon, which is an aromatic sp^2 carbon. This disrupts the aromatic bonding in the second ring, increasing the relative energy of the TS by 0.04 eV. This trend is also observed in 1,6- and 1,8-naphthyridine, where there is one nitrogen atom per ring.

Nevertheless, this explanation does not fully account for the observed patterns in quinazoline and quinoxaline, where both nitrogen atoms are located within the same ring. Notably, quinoxaline exhibits a level of planarity at the TS geometry comparable to the lowest TS in quinazoline, TS5. This discrepancy is likely due to complex interactions between the nitrogen atoms, which influence the positioning and energy of the TSs.

4.3.2.3 Dynamics in the triplet state (τ_3)

The time constant τ_3 is nominally ascribed to the lifetime of the T_1 state, however, as discussed in Section 4.3.2.2, the triplet manifold is entered *via* a S_1/T_2 MECP. A single time constant for the triplet manifold exists due to the fact that the molecules transition rapidly through the T_2 state onto the T_1 surface. These photorelaxation pathways from the S_1/T_2 MECPs to the T_1 minima in all six

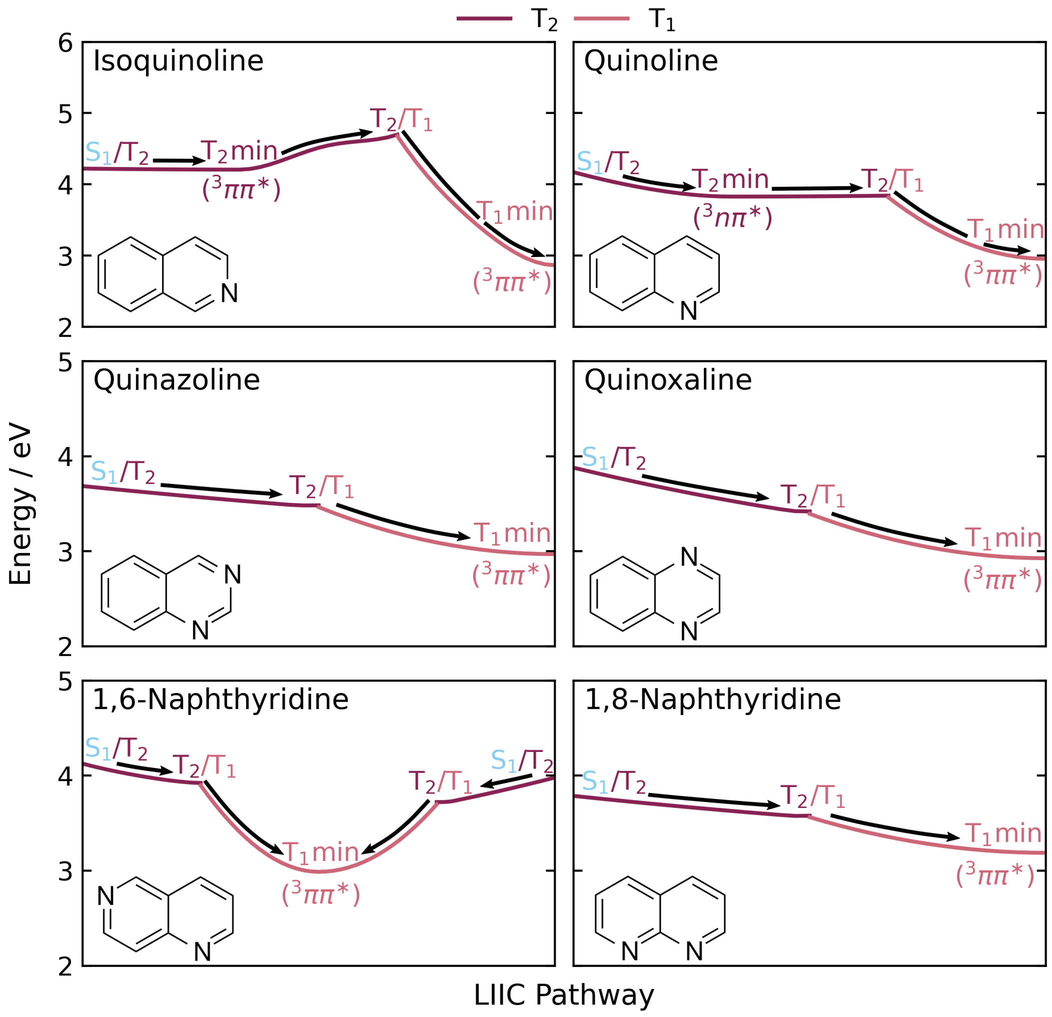

Figure 4.6: PE profiles, constructed by LIICs from the S_1/T_2 MECPs to the T_1 minima, in all six molecules, computed at the SCS-ADC(2)/cc-pVDZ level. For clarity, only the active state involved along the pathway to the S_1 $(n\pi^*)$ minimum is shown and the ground state has been omitted.

molecules are shown in Fig. 4.6. Only isoquinoline, quinoline and quinoxaline have T_2 minima, with $\pi\pi^*$ character in isoquinoline and $n\pi^*$ character in quinoline and quinoxaline. In quinoline the PES from the S_1/T_2 MECP to the T_2/T_1 is relatively flat, where the molecule firstly undergoes planarisation from the S_1/T_2 MECP to the T_2 minimum, followed by a decrease in the C−N−C bond angle as the relaxation to the T_1 minimum occurs. In the case of quinoxaline, the molecule will pass through the T_2/T_1 MECI before reaching this minimum, and hence, has been excluded in the pathway shown in Fig. 4.6. Therefore, both molecules are expected to transition rapidly to the T_1 state. In isoquinoline, the T_2/T_1 MECI is located at higher energy than the S_1/T_2 MECP, however, the molecule is unlikely to enter the triplet manifold at this geometry given the very small SOC value, dictated by the symmetry of S_1 and T_2 states close to the FC region. Moreover, in quinazoline, 1,6- and 1,8-naphthyridine the T_2 minimum coincides with the T_2/T_1 MECI, as shown in Fig. 4.6, and hence, these systems are likely to move rapidly to T_1. The changes in molecular geometry along these photorelaxation coordinates corresponds to a decrease in one or both C$-$N$-$C bond angle(s) leading

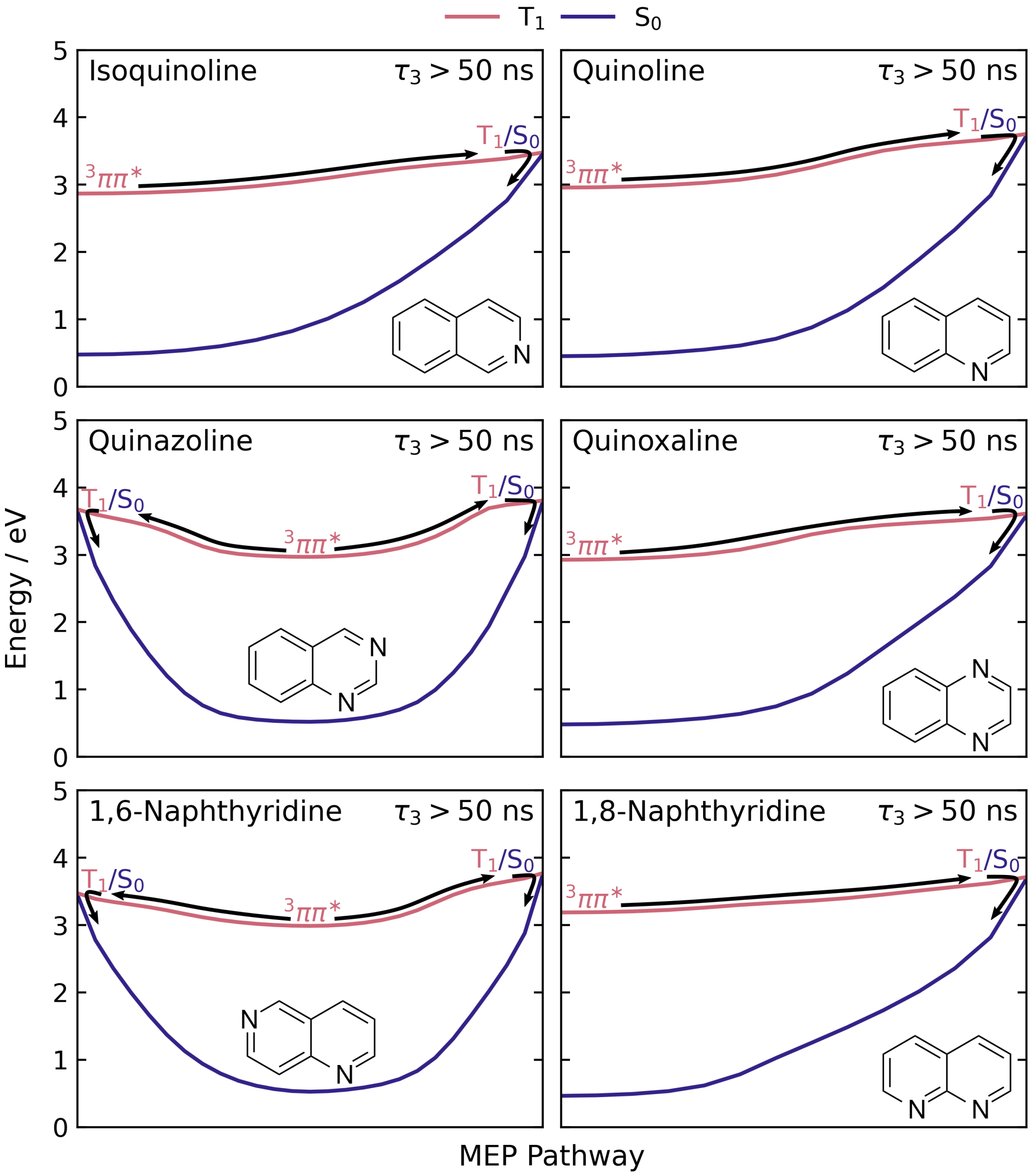

Figure 4.7: MEPs from the T_1 minima to the T_1/S_0 MECPs, for all six molecules computed at the SCS-MP2/SCS-ADC(2) level of theory with the cc-pVDZ basis set.

to a geometry resembling the FC region on the T_1 surface.

All six molecules have one T_1 minimum, which is comprised of $\pi\pi^*$ character, leading to the characteristic signal at 380-460 nm in the TAS spectrum. There is a barrierless transition from each T_2/T_1 MECI to the T_1 minimum. Once the T_1 surface is accessed, the molecules are expected to stay around the T_1 minima, as the T_1/S_0 MECPs are much higher in energy than the minima, with values ranging from 0.48-0.83 eV dependent on the molecule, which is shown in Fig. 4.7. The T_1/S_0 MECPs all resemble the same geometries as the S_1/S_0 MECIs, where motion out of the plane occurs. Although the SOC between the T_1 state and the ground state cannot be calculated at the SCS-ADC(2)/SCS-MP2 level, the lifetime in the triplet manifold is proposed to be much longer than the singlet manifold, due to the fact the T_1/S_0 MECPs are less accessible compared to the S_1/S_0 MECIs, which rationalises the longer than 50 ns lifetime.

4.3.3 Comparison with multireference methods

The results presented in this chapter are obtained using the SCS-ADC(2) electronic structure method. However, as SCS-ADC(2) is a single-reference method, it often fails to accurately describe the region around S_1/S_0 MECIs. Therefore, the plots along the S_1 surface, leading to the S_1/S_0 MECIs, shown in Fig. 4.5 for all six molecules, have been compared with XMS-CASPT2. The resulting plots, shown in Fig. 4.8, demonstrate that the overall shapes of the potentials remain relatively similar between the methods, despite the relative energy shift in the S_1 state. However, closer to the S_1/S_0 MECIs, the potentials show slightly greater deviations. Nevertheless, the plots reveal that the optimised S_1/S_0 MECIs at the SCS-ADC(2)/SCS-MP2 level of theory are geometrically close to those obtained with XMS-CASPT2. These similarities between the two methods provides confidence in the qualitative accuracy of the SCS-ADC(2) results around the S_1/S_0 MECI regions.

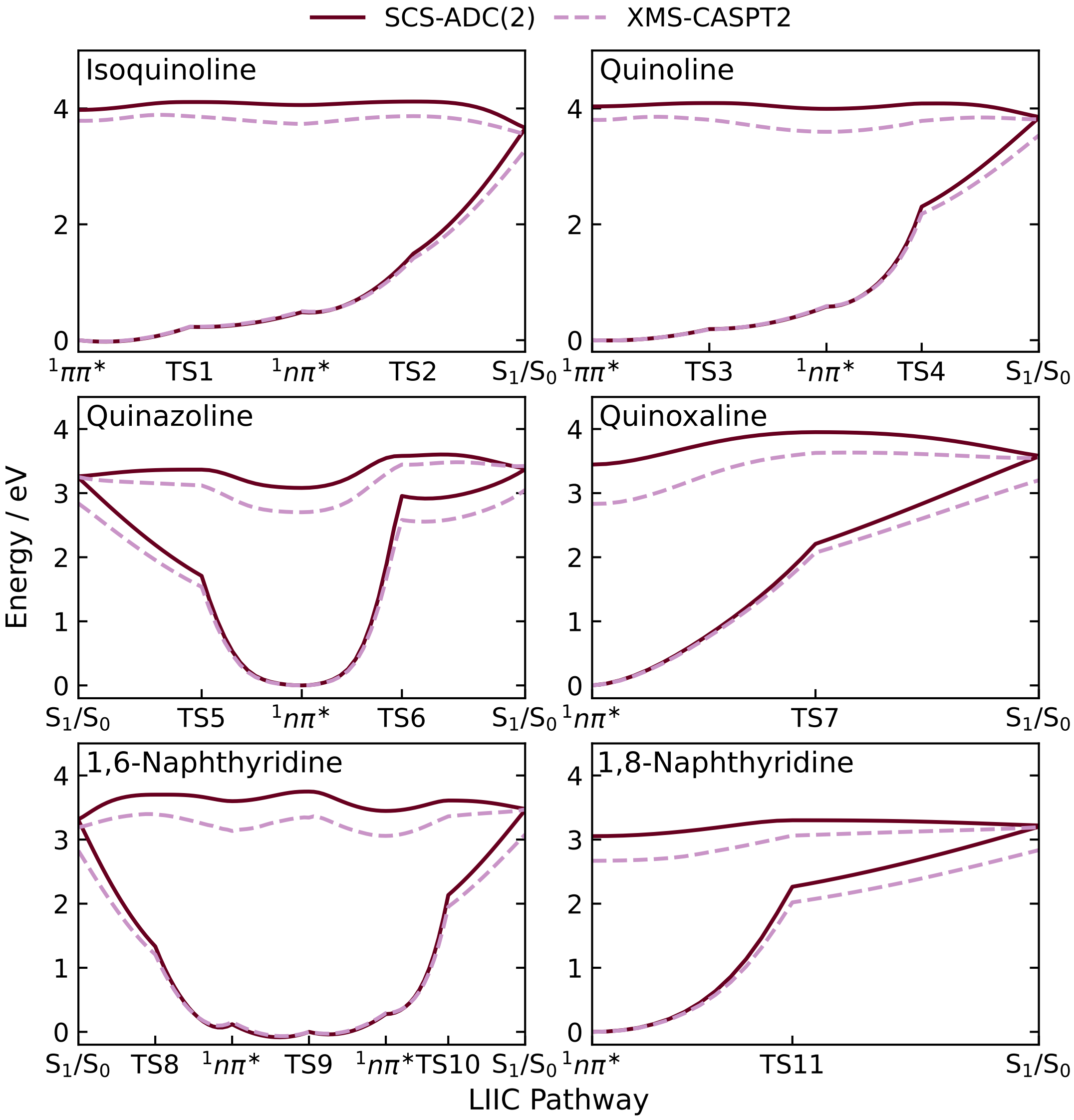

Figure 4.8: A comparison of the S_1 and S_0 states between SCS-ADC(2)/cc-pVDZ (burgundy solid line) and XMS-CASPT2/cc-pVDZ (lilac dashed line) along the SCS-ADC(2) photorelaxation pathways shown in Fig. 4.5. A (12,11) active space was used for the XMS-CASPT2 calculations in isoquinoline and quinoline, whilst a (14,12) active space was used for quinazoline, quinoxaline, 1,6- and 1,8-naphthyridine.

4.4 Conclusion

The quantum chemical calculations rationalise the dynamics observed in ultrafast TAS experiments in terms of MECIs, SOC values at MECPs and energy barriers. Trends in the photophysics have been identified in a sequence of six molecules formed by substituting nitrogen atoms(s) into varying positions in naphthalene. Although closely related, these six molecules exhibit large variations in their photochemistry.

The experiments identified three distinct lifetimes in the photoexcited molecules, which have been elucidated as rapid IC to the S_1 state (τ_1), competition between IC to the ground state and ISC into the triplet manifold (τ_2), and slow evolution in the T_1 state (τ_3). The first lifetime (τ_1) is characterised by a cascade through a sequence of MECIs and is especially efficient in the two molecules with only one nitrogen atom (isoquinoline and quinoline). Adding a second nitrogen atom slows down the dynamics, particularly in the same ring, where more complex excited state PESs are observed. In all molecules, τ_1 is correlated to the number of MECIs along the photorelaxation pathways to the S_1 surface and whether minima or PE barriers are present along these pathways. The second lifetime (τ_2) is associated with the competition between IC to the ground state and ISC into the T_2 state, from S_1. The rate of IC relates closely to the height of the PE barriers, which are lowest for isoquinoline and quinoline, higher in molecules with one nitrogen atom per ring (1,6- and 1,8-naphthyridine), and highest for quinoxaline and quinazoline, where the two nitrogen atoms are in the same ring. Additionally, the speed of ISC is closely related to the SOC at the S_1/T_2 MECP, with all target molecules decaying rapidly to the T_1 state once they enter the triplet manifold. Finally, the much longer τ_3 lifetimes are attributed to the fact that the T_1/S_0 MECPs lie much higher in energy than the T_1 minima.

A natural extension of this study would be to carry out simulations to determine more closely how the characteristic features identified in the electronic structure relate to the actual dynamics. Therefore, in the following chapter, the dynamics in a subset of these molecules will be discussed.

5

Dynamics of three azanaphthalenes

5.1 Introduction

Quantum chemical calculations were employed in the previous chapter to rationalise the dynamics observed in recent TAS experiments, by identifying characteristic features on the PESs for the six azanaphthalene molecules shown in Fig. 4.1. A logical next step is to simulate the nonadiabatic molecular dynamics across the whole molecular series in order to determine how closely these characteristic features *actually* correlate with the dynamics. Ideally, the dynamics in all six molecules would be simulated, however, this is computationally too expensive, at least in the first instance. Instead, a subset of three representative and interesting cases have been selected, specifically the molecules isoquinoline, quinoline and quinazoline.

The TAS experiments revealed that isoquinoline has the shortest τ_2 lifetime and also appears reluctant to undergo ISC into the triplet manifold, which was attributed to the small barrier on the S_1 surface to the S_1/S_0 MECI and the lack of SOC at the S_1/T_2 MECP, as discussed in Chapter 4. In contrast, quinoline has a longer τ_2 lifetime and displays a larger propensity for ISC into the triplet state, ascribed to the larger energy barrier on the path to the S_1/S_0 MECI and significant SOC at the S_1/T_2 MECP. Lastly, the τ_1 and τ_2 lifetimes in quinazoline are significantly longer than any of the other five molecules and, although the quantum yield for ISC in quinazoline was not determined, a large triplet-triplet absorption peak exists at long time delays in the excited state absorption spectrum, indicating an appreciable population in the triplet manifold. The longer τ_1 lifetime is likely related to the presence of minima on the S_3 and S_2 PESs and the more complex photorelaxation pathways from $S_3 \rightarrow S_1$, whereas the τ_2 lifetime is due to the large barrier blocking re-population of the ground state as well as the smaller SOC values at the S_1/T_2 MECP. The span of lifetimes and the different propensities for ISC into the triplet manifold makes these three molecules interesting targets for dynamics.

In the present chapter, TSH simulations are propagated for 2 ps to investigate the ultrafast dynamics in isoquinoline, quinoline and quinazoline. Internal coordinates relating to the photorelaxation mechanisms are monitored throughout to connect the key features identified in the electronic structure calculations to the simulations. Finally, an apparent discrepancy in overall timescales between the simulations and the experiments is discussed.

5.2 Computational methods

5.2.1 Absorption spectrum and nonadiabatic dynamics

The UV-vis absorption spectra and TSH dynamics simulations were performed using the SCS-ADC(2) electronic structure method [74, 75] with the def2-SV(P) basis set. This basis reproduces the PE profiles calculated using the cc-pVDZ basis in Chapter 4, thus maintaining the accuracy, while decreasing the computational time required for the dynamics simulations.

The UV-vis absorption spectra were calculated using the SHARC 2.1 software package [50, 58] using 4000 initial geometries for isoquinoline and 8000 for quinoline and quinazoline. The geometries are generated by sampling the Wigner distribution of the ground state harmonic oscillator at 0 K for all vibrational normal modes, based on SCS-MP2/def2-SV(P) level of theory. Initial conditions for the dynamics were selected using excitation windows shifted from the experimental wavelength of 267 nm (4.64 eV), which takes into account the difference in energy between the computed and experimental absorption spectra. This ensures that excitation occurs in the same region as in the experiment and hence, that the correct electronic state is excited. Consequently, excitation windows of 4.84–4.91 eV, 4.92–4.97 eV and 4.82–4.93 eV for isoquinoline, quinoline and quinazoline, respectively, were applied. These widths are based on the experimental laser pulse with a full width at half maximum (FWHM) of 1 nm, with a slight broadening to increase the ensemble of trajectories. The variation in excitation windows among the three molecules arises from a situation where one particularly bright initial geometry dominates within the excitation region. Since all other geometries are normalised against this dominant geometry, as discussed in Chapter 2, either more initial geometries or a slightly broader excitation window is required to ensure a sufficient number of initial conditions for the simulations, thereby achieving an adequate trajectory sample size. In this case, the broadening widths were slightly adjusted to achieve a trajectory count within the range of 170–190.

The nonadiabatic molecular dynamics simulations were performed using Tully's fewest switches surface hopping algorithm [53] with the energy based decoherence scheme of Granucci and Persico, using a decoherence parameter of 0.1 Hartree. The simulations were performed using SHARC 2.1 [50, 58] interfaced with Turbomole 7.7 [134] for the electronic structure calculations, and were propagated with a 0.5 fs time step for the nuclei and a 0.02 fs electronic time step. All trajectories were propagated for a total time duration of 2 ps and were included in the analysis up to this point, unless they had entered a region where the energy gap between the ground state and first populated excited state (S_1 or T_1) would fall below 0.15 eV. The reason for this is that SCS-ADC(2) is unreliable in areas near to crossings with the ground electronic state [76], as discussed earlier in Chapter 2. When this situation occurred, for trajectories in the S_1 state, a hop to the ground state was induced, and the trajectory was terminated, with the system assumed to remain in the ground state for the remainder of the simulation. However, for trajectories in the T_1 state, the trajectory was terminated, with the assumption that the molecule remained in this state. This approximation was made because the SOC cannot be calculated between T_1 and S_0 using the SCS-ADC(2)/SCS-MP2 method employed for the simulations, and the rate of ISC is strongly dependent on the SOC values.

5.2.2 Electronic structure benchmarking

As discussed later, there is a discrepancy between the overall timescales of the simulations and those observed in the experiments. To investigate this further, extensive additional benchmarking of the electronic structure calculations was undertaken. Specifically, the PESs in Figs. 4.3 and 4.5, shown in Chapter 4, were benchmarked with XMS-CASPT2 [70] using the cc-pVDZ basis set. All XMS-CASPT2 calculations were performed in OpenMolcas v22.10 [143, 144] employing an imaginary shift of 0.2 Hartree. A (12,11) active space is used for the calculations of isoquinoline and quinoline, whereas a (14,12) active space is used for quinazoline, with the latter depicted in Fig. 5.1. The (12,11) active space consists of five sets of π and π^* orbitals as well as one nitrogen lone pair orbital. In the (14,12) active space there is one extra lone pair orbital, since quinazoline contains two nitrogen atom centres in the naphthalene ring. To ensure convergence, the calculations for the S_3

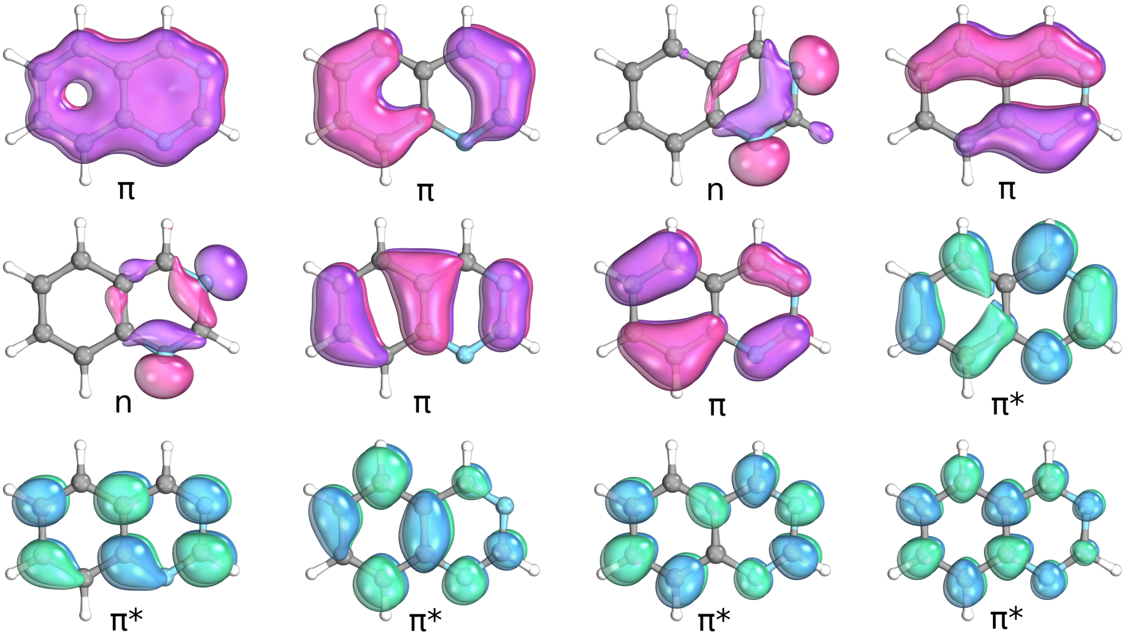

Figure 5.1: The (14,12) active space used in the XMS-CASPT2 calculations of quinazoline. This active space includes five π bonds, the two lone pair orbitals and five π^* orbitals. Note that the (12,11) active space used in isoquinoline and quinoline, contains one less orbital as these molecules only contain one nitrogen atom centre.

→ S_1 PE pathways were state-averaged over the eight lowest-lying singlet states, while the S_1 PESs were state-averaged over the three lowest-lying singlet states.

Furthermore, solvation effects of bulk hexane on the SCS-ADC(2) PE profiles in Figs. 4.3 and 4.5 were modelled using the COSMO implicit solvation model [176], with an ϵ value of 1.88, appropriate for hexane. For the calculations along the pathways shown in Fig. 4.3, the active state displayed in the figure was selected for solvent charge equilibration. For example, along the PES between the S_3/S_2 MECI and the S_2/S_1 MECI, the S_2 state was chosen. Moreover, for the S_1 PESs shown in Fig. 4.5, the S_1 state was used. These computations as well as the XMS-CASPT2 calculations are detailed in Section 5.3.3, which includes an in-depth discussion of the discrepancy between the timescales observed in the simulations compared to the experiments.

5.3 Results and discussion

5.3.1 Absorption spectra

The UV-vis absorption spectra for isoquinoline, quinoline and quinazoline were calculated with the four lowest-lying singlet states and are shown in Fig. 5.2. As discussed in Chapter 4, SCS-ADC(2)/cc-pVDZ overestimates the excitation energies compared to the experiment and the same trend holds true when using the def2-SV(P) basis. Therefore, the calculated energies have been shifted down in energy by 0.23 eV in isoquinoline and quinazoline, and by 0.3 eV in quinoline to align the theoretical and the experimental spectra.

In isoquinoline, there are two absorption bands, where the main band has a peak maximum around 4.77 eV. The dominant contribution to this absorption band is the S_3 state, ascribed to the optically bright second $\pi\pi^*$ state, however, there is also a small contribution from S_2. This spectrum is shown in comparison to a section of the gas-phase absorption spectrum reported by Leach *et al.*, which is associated with the same $3A' \leftarrow 1A'$ transition [180]. The shapes of the peaks are relatively similar, and in the lilac shaded region, which is the excitation region

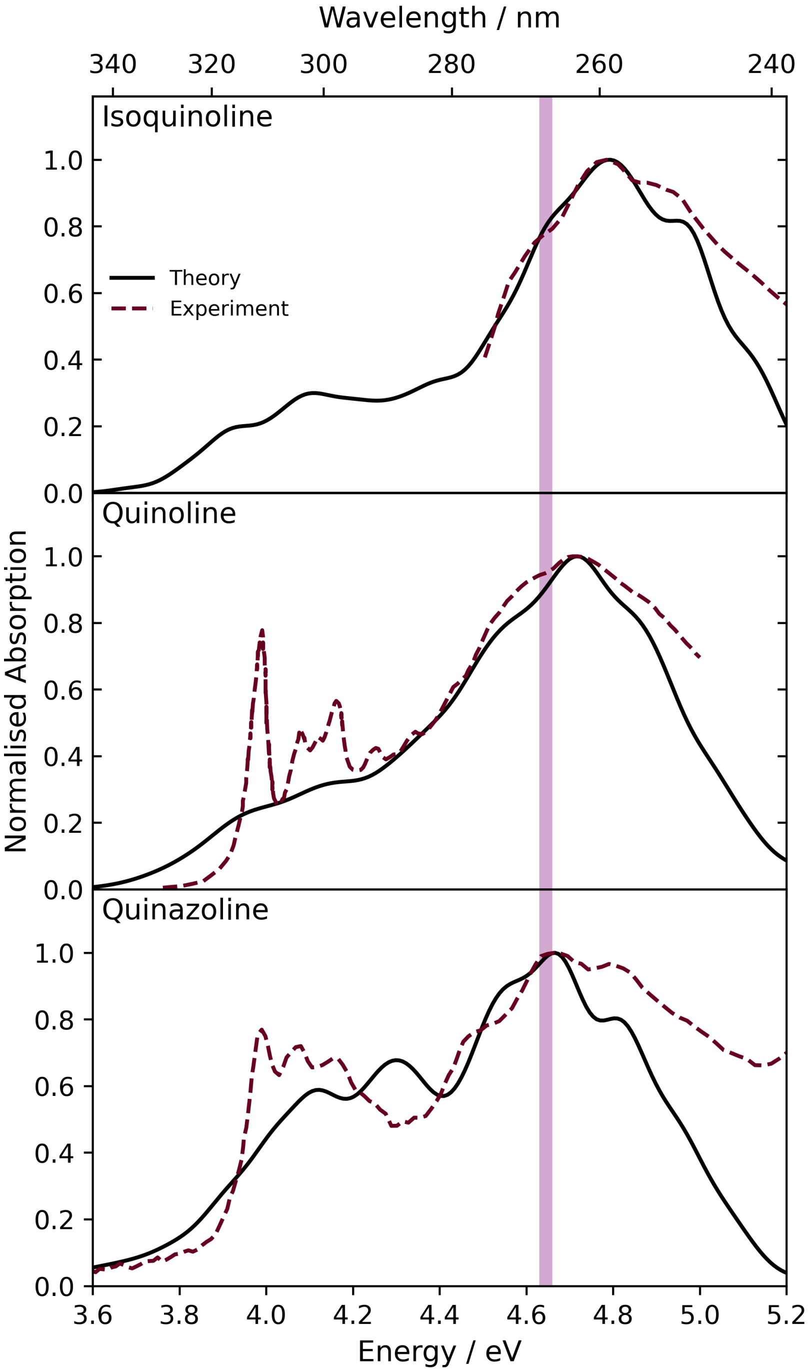

Figure 5.2: UV-vis absorption spectra of isoquinoline, quinoline and quinazoline computed at the SCS-ADC(2)/def2-SV(P) level of theory (black solid line) compared to the experimental spectra (burgundy dashed line). The isoquinoline [180] and quinoline [181] experimental spectra used are reported in the gas-phase, whereas in quinazoline the spectrum in hexane is used for comparison. A shift of 0.23 eV has been applied to the theory spectra in isoquinoline and quinazoline, and a shift of 0.3 eV is applied to quinoline, to align the theory and experimental spectra. The excitation window, centred at 267 nm (4.64 eV) is shown by the lilac shaded region.

that will be employed for the simulations, there is good agreement and hence, it is concluded that a sufficiently accurate excitation region is obtained.

The absorption spectrum in quinoline shows similar features to isoquinoline, although the peak maximum is redshifted slightly to 4.72 eV. This small shift in energy can be attributed to the S_3 state in quinoline having a greater proportion of HOMO to LUMO character transitions due to the location of the heteroatom. In contrast, isoquinoline features additional transitions, which may slightly increase the excitation of the S_3 state. The gas-phase spectrum published by Leach *et al.* is also shown in the quinoline panel in Fig. 5.2, in the region which includes the $2A' \leftarrow 1A'$, $1A'' \leftarrow 1A'$ and $3A' \leftarrow 1A'$ transitions. Again, the main peak is attributed to absorption of the S_3 state matches well with experiment, although there is slight variation in the excitation region.

Lastly, quinazoline also displays two absorption bands, however, they lie closer in proximity compared to isoquinoline and quinoline, reflecting the reversal of state ordering, where S_1 has $n\pi^*$ character and S_2 has $\pi\pi^*$ character in quinazoline. This spectrum is shown in comparison to the experimental spectrum recorded from the TAS experiments in hexane solution, as a gas-phase spectrum was unavailable. It should be noted that comparing spectra in the gas-phase vs hexane solvation will not affect the simulations, as only a small red shift of 5 nm is seen, and hence, the *same* electronic state is excited in both cases. The agreement between theory and experiment is slightly worse compared to the other two molecules, however, within the excitation region, there is congruence.

As a final comment, the experimental absorption spectra all show vibrational structure in the lowest energy absorption band, which is not replicated in the theory spectra. This is due to the fact that the nuclear ensemble approach [149] is used to compute the spectra and this method does not contain any information about vibrational transitions. However, from initial tests in quinoline, this vibrational structure was resolved using adiabatic hessian Franck-Condon calculations (see Section 3.2.2) [132] at the SCS-ADC(2)/cc-pVDZ level of theory. Nevertheless, for the purpose of these simulations, the S_3 state is initially excited, and hence no further detail will be provided with regards to the vibrational structure in S_1.

5.3.2 Nonadiabatic molecular dynamics

Surface hopping simulations were employed to calculate 2 ps of excited state dynamics using SCS-ADC(2)/def2-SV(P). The excitation windows were shifted from 267 nm (4.64 eV) to take into account the difference in energies between the calculated absorption spectra and the experimental spectra, as discussed in Section 5.3.1, which ensures excitation into the correct state. Consequently, the simulations were performed using excitation windows of 4.84–4.91 eV, 4.92–4.97 eV and 4.82–4.93 eV for isoquinoline, quinoline and quinazoline, respectively, which leads to 184 trajectories in isoquinoline, 172 in quinoline and 190 in quinazoline, with the majority starting in the optically bright S_3 state and a small proportion in the S_2 state.

5.3.2.1 Populations

The short-time ($t \leq 200$ fs) classical adiabatic populations, with multiplets summed up, are shown in Fig. 5.3 for all three molecules. Isoquinoline and quinoline exhibit comparatively similar populations during the first 200 fs, with the excited state populations quickly transferred to S_1, as the majority of trajectories are in S_1 by $t \approx 60$ fs. This agrees with the predictions from the electronic structure calculations, as the minima on S_3 and S_2 coincide with the S_3/S_2 and S_2/S_1 MECIs, leading to efficient relaxation into S_1, as shown in Fig. 4.3. In contrast, quinazoline displays different dynamics, with the populations in S_3 and S_2 decaying more slowly. Additionally, the increase in S_1 population is slower as the maximum population is not reached until $t \approx 180$ fs. According to the analysis in the previous chapter, this can be attributed to the presence of a S_3 and S_2 minimum in quinazoline, as well as the more complex PESs, shown in Figs. 4.3 and 4.4. Finally, in the short-time dynamics of isoquinoline, there is a small amount of population in the ground state. This is due to the direct population of the S_1 ($^1n\pi^*$) minimum from the S_2/S_1 MECI. Once in this minimum, the very small energy barrier to the S_1/S_0 MECI allows for efficient IC to the ground state. Overall, these trends in the dynamics agree with the qualitative predictions in Chapter 4. However, it is important to note that during the first 25 fs, the S_3 population decay is similar across all three molecules, suggesting that the S_2 state may play a larger role in the varying lifetimes.

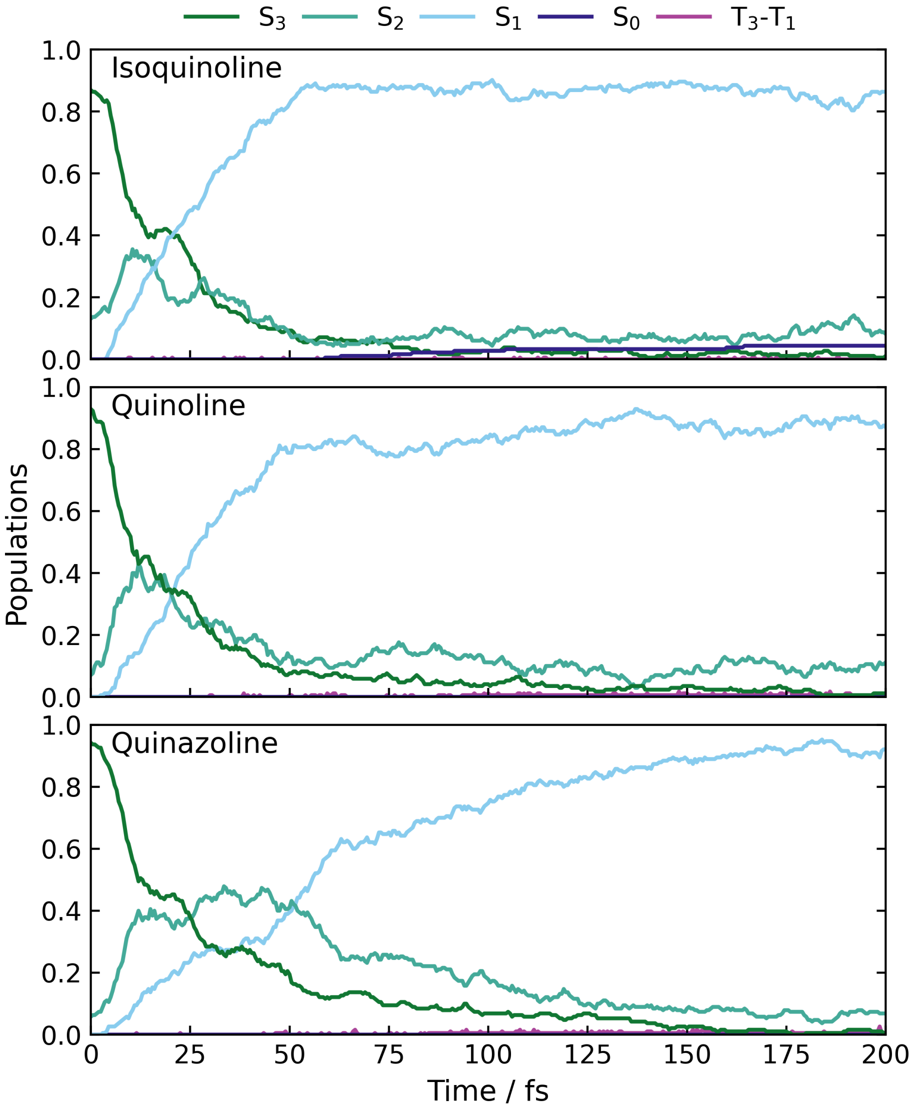

Figure 5.3: The short-time ($t \leq 200$ fs) classical adiabatic populations of isoquinoline, quinoline and quinazoline, with the multiplet components summed up for the triplet states. The triplet state populations remain very small throughout this initial period of dynamics.

Subsequently, after 200 fs, the molecules begin to undergo photorelaxation to S_0 at different rates, as shown in Fig. 5.4. On these longer timescales, the population plots show clear trends in the rate of S_1 decay and rise in S_0 population across the three molecules. In isoquinoline, the S_1 population decreases to 50% in ~1.25 ps and after 2 ps, 70% of the trajectories have undergone photorelaxation to the ground state, while 29% remain in a singlet excited state. The S_1 decay rate in quinoline is slightly slower compared to isoquinoline, where the S_1 population decreases to 50% in ~1.38 ps, and by the end of the simulations 65% of trajectories are on the ground state and 33% are still in a singlet excited state. On the contrary, the S_1 decay in quinazoline is much slower, as the S_1 population does not reach 50% by the end of the simulations with only 21% of the trajectories undergoing photorelaxation to S_0,

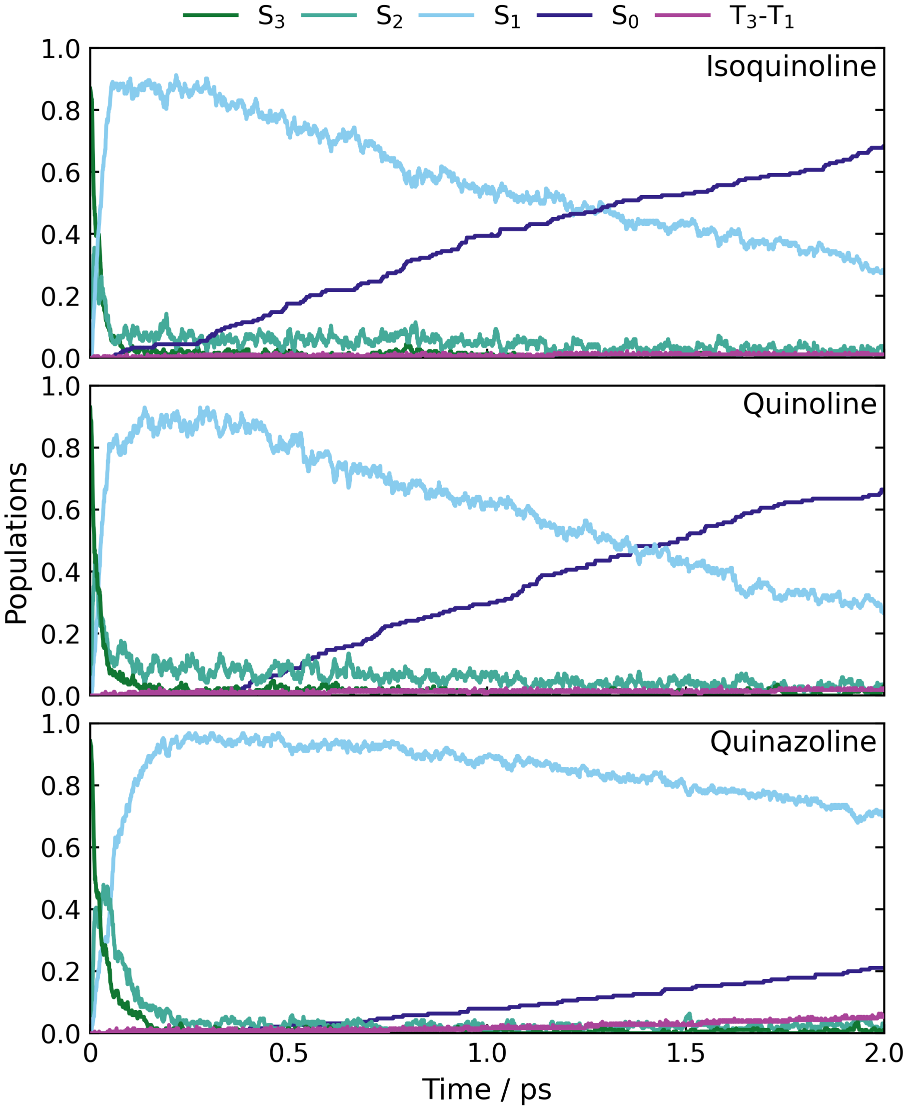

Figure 5.4: The long-time classical adiabatic populations of isoquinoline, quinoline and quinazoline, where the multiplet components are summed up for the triplet states.

leaving 74% remaining in a singlet excited state. These trends reflect the calculated barrier heights from the S_1 ($^1n\pi^*$) minima to the S_1/S_0 MECIs, shown in Fig. 4.5, where isoquinoline has the smallest barrier of 0.06 eV, followed by quinoline, which lies 0.03 eV higher in energy than the barrier in isoquinoline and finally, quinazoline has the largest barriers of 0.29 eV and 0.50 eV to the two accessible S_1/S_0 MECIs.

By the end of the simulations, there is a small proportion of trajectories that enter the triplet manifold: 1% in isoquinoline, 2% in quinoline and 5% in quinazoline. These transitions into the triplet state occur predominantly through the $S_1 \rightarrow T_2$ pathway, in all three molecules, which was determined by assessing the point where each trajectory hops to the triplet state. In these three systems, the triplet population is inversely proportional to the rate of S_1 decay, with quinazoline exhibiting the slowest decay and the largest triplet state population, while isoquinoline shows the fastest decay and the smallest triplet population. Therefore, the simulations demonstrate that ISC is a competing process with photorelaxation to the ground state, validating the electronic structure predictions.

5.3.2.2 Geometry analysis

To correlate the characteristic features identified in the previous static analysis with the dynamics observed in the simulations, the hopping geometries from $S_3 \rightarrow S_2$, $S_2 \rightarrow S_1$ and $S_1 \rightarrow S_0$, have been analysed to gain insight into the regions where IC occurs. The electronic structure calculations in Chapter 4 showed that there are two key geometry changes involved in the photorelaxation pathways: firstly, varying C−N−C bond angle(s), where the planarity of the ring is preserved, and secondly out of plane distortions. The former is associated with motion on the excited state surface before the S_1/S_0 MECI is approached, and the latter takes place in regions around the S_1/S_0 MECI. Therefore, in isoquinoline and quinoline, the C−N−C bond angle has been monitored at the $S_3 \rightarrow S_2$ and $S_2 \rightarrow S_1$ hopping geometries, whereas the dihedral angle around atoms 8a, 1, 2 and 3 (see Fig. 4.1 for numbering) has been tracked at geometries where a $S_1 \rightarrow S_0$ hop occurs, measuring the distortion out of the plane of the aromatic ring.

From Fig. 5.5 (a), in both molecules, the majority of trajectories hop onto the S_2 state with a C−N−C bond angle in the range of 115-120°. Most of these hops occur soon after excitation and hence, in both molecules, the geometries resemble the ground state equilibrium, with a bond angle of 116°. However, it should be noted that a small proportion of hops occur at larger bond angles (120-135°) in quinoline, which is absent in isoquinoline. Nevertheless, this does not seem to impact the population decay of the S_3 state, as both molecules undergo rapid decay from this state, which is shown in Fig. 5.3.

As discussed in the previous chapter in Section 4.3.2.1, the electronic structure calculations show that the two S_1 minima in isoquinoline and quinoline are accessible from the S_2/S_1 MECI. Moreover, the MECI geometries have a C−N−C bond angle of 124°, which lies in between the values for the $^1\pi\pi^*$ and $^1n\pi^*$ minima on the S_1 surface. Therefore, the hopping geometry from $S_2 \rightarrow S_1$ may influence which minimum is accessed through IC during the simulations. From Fig. 5.5 (b), there is a relatively equal split before and after 122.5°, indicating a similar proportion of trajectories fall into both the $^1\pi\pi^*$ and $^1n\pi^*$ minima on S_1.

Additionally, in Fig. 5.5 (c), the absolute value of the dihedral angles around atoms 8a, 1, 2 and 3 have been monitored at geometries where hops to the ground state occur, as this dihedral angle increases in regions near to the S_1/S_0 MECI due to the out of plane motion. The S_1/S_0 MECI in isoquinoline has an absolute dihedral angle of 64.6°, whereas the absolute value in quinoline is 68.3°. In isoquinoline, a geometry resembling the S_1/S_0 MECI is seen in all trajectories where a hop to the ground state occurs, however, they have varying dihedral angles in the region of 50–85°. Furthermore, the majority of hops occur in geometries with dihedral angles around 62.5–72.5°, which is in the region where the MECI lies. The range in dihedral angles between 50–85°, suggests the CI seam is invariant to small changes in the dihedral angle between this range. The same pattern is observed in quinoline, although the largest number of hops take place in a smaller range between 65–70°.

Quinazoline contains two nitrogen atoms and therefore, has two important C−N−C bond angles: the $C_2{-}N_3{-}C_4$ (θ_1) and $C_{8a}{-}N_1{-}C_2$ (θ_2) angles. Thus,

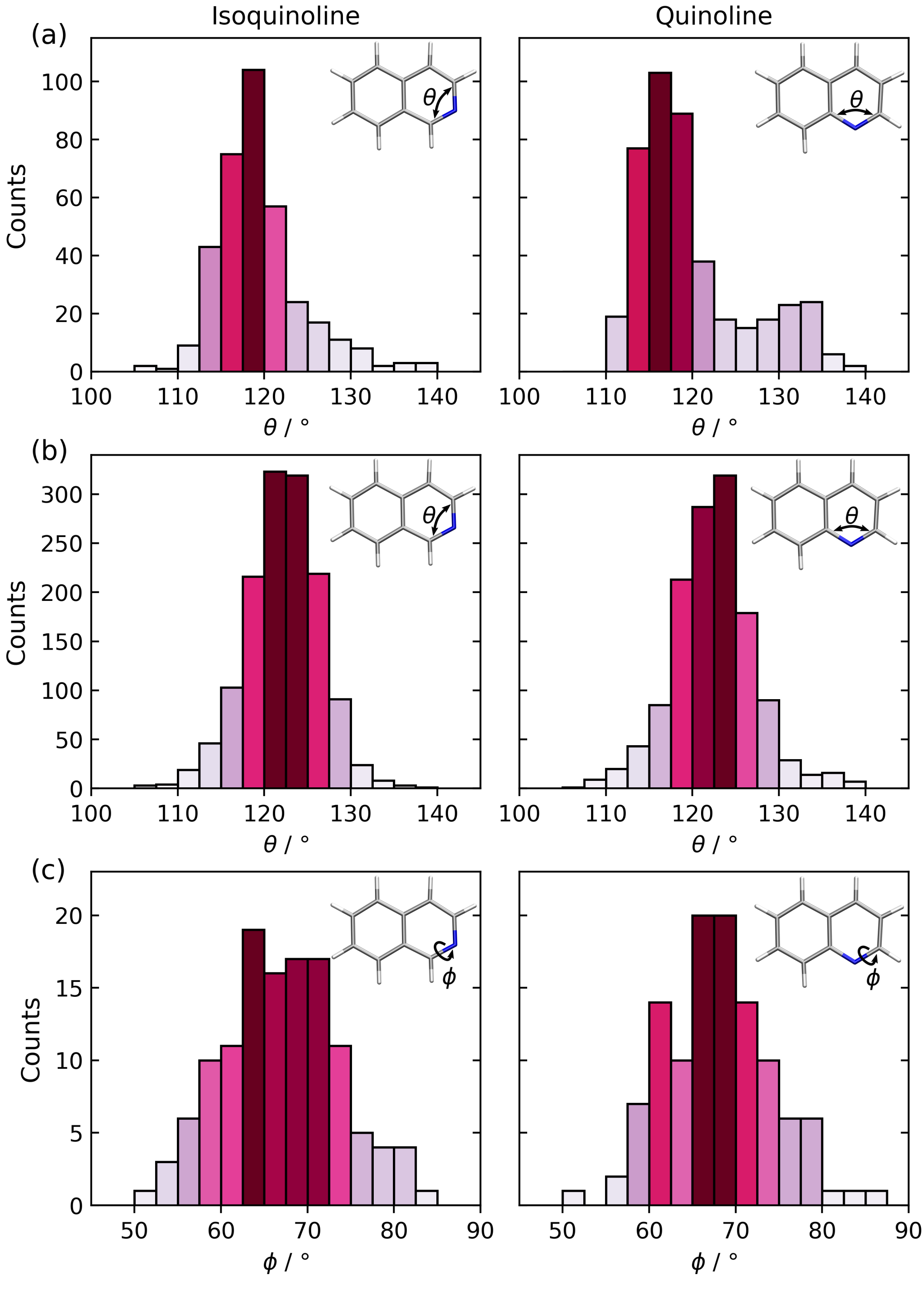

Figure 5.5: Histograms of the C−N−C bond angle during hops from $S_3 \rightarrow S_2$ (a) and $S_2 \rightarrow S_1$ (b), as well as the absolute value of the dihedral angle around atoms 8a, 1, 2 and 3 ($C_{8a}-C_1-N_2-C_3$ in isoquinoline and $C_{8a}-N_1-C_2-C_3$ in quinoline) during hops from $S_1 \rightarrow S_0$ (c), in both isoquinoline and quinoline.

both angles can be tracked at the geometries where $S_3 \rightarrow S_2$ and $S_2 \rightarrow S_1$ hops occur, which is shown in Fig. 5.6 (a) and (b), respectively. Firstly, in Fig. 5.6 (a), the majority of hops occur where θ_1 has a value between 115–120°, and θ_2 varies more with a range from 110–125°. This is in agreement with the electronic structure calculations, discussed in Section 4.3.2, where there are two S_3/S_2 MECIs, one which corresponds to a $^1\pi\pi^* \rightarrow {}^1\pi\pi^*$ transition, shown on the left-hand side (LHS) of Fig. 4.3, and the other corresponds to a $^1\pi\pi^* \rightarrow {}^1n\pi^*$ transition, included on the right-hand side (RHS) of Fig. 4.3. The difference between these two geometries is the change in θ_2, where the MECI which leads to retention in state character has an angle of 114°, whereas the MECI, which leads to a change in state character has an angle of 125°. Therefore, in the dynamics simulations, IC occurs onto the S_2 surface *via* geometries that resemble both MECIs.

Interestingly, the largest number of hops that occur from $S_2 \rightarrow S_1$ have a θ_2 angle in the range of 115–120°, which suggests that the S_1 state is accessed through geometries similar to the S_2/S_1 MECI that lies closer to the FC region. This observation is supported by the fact that there are two photorelaxation pathways on the S_2 surface, to the S_2/S_1 MECI near the FC region. Firstly, there is the barrierless pathway from the S_3/S_2 MECI on the LHS of Fig. 4.3 and secondly, there is another pathway, which is shown on the LHS in Fig. 4.4, and proceeds *via* an easily accessible TS from the S_2 minimum.

Finally, quinazoline has two energetically accessible S_1/S_0 MECIs, shown in Fig. 4.5, where the MECI on the LHS can be followed by measuring the $C_2{-}N_3{-}C_4{-}C_{4a}$ (ϕ_1) dihedral angle, whereas the MECI on the RHS can be monitored by measuring the $C_{8a}{-}N_1{-}C_2{-}C_3$ (ϕ_2) dihedral angle. Although not many trajectories reach this region of the PES by 2 ps, the trajectories that hop to the ground state have been assessed by following these two dihedral angles and this can be seen in Fig. 5.6 (c). The majority of trajectories hop to the ground state *via* geometries that resemble the S_1/S_0 MECI, where ϕ_1 is much larger ϕ_2. However, a few pass through regions that resemble the S_1/S_0 MECI associated with an increased ϕ_2 dihedral angle. These statistics reflect the barrier heights shown in Fig. 4.5 as fewer trajectories access

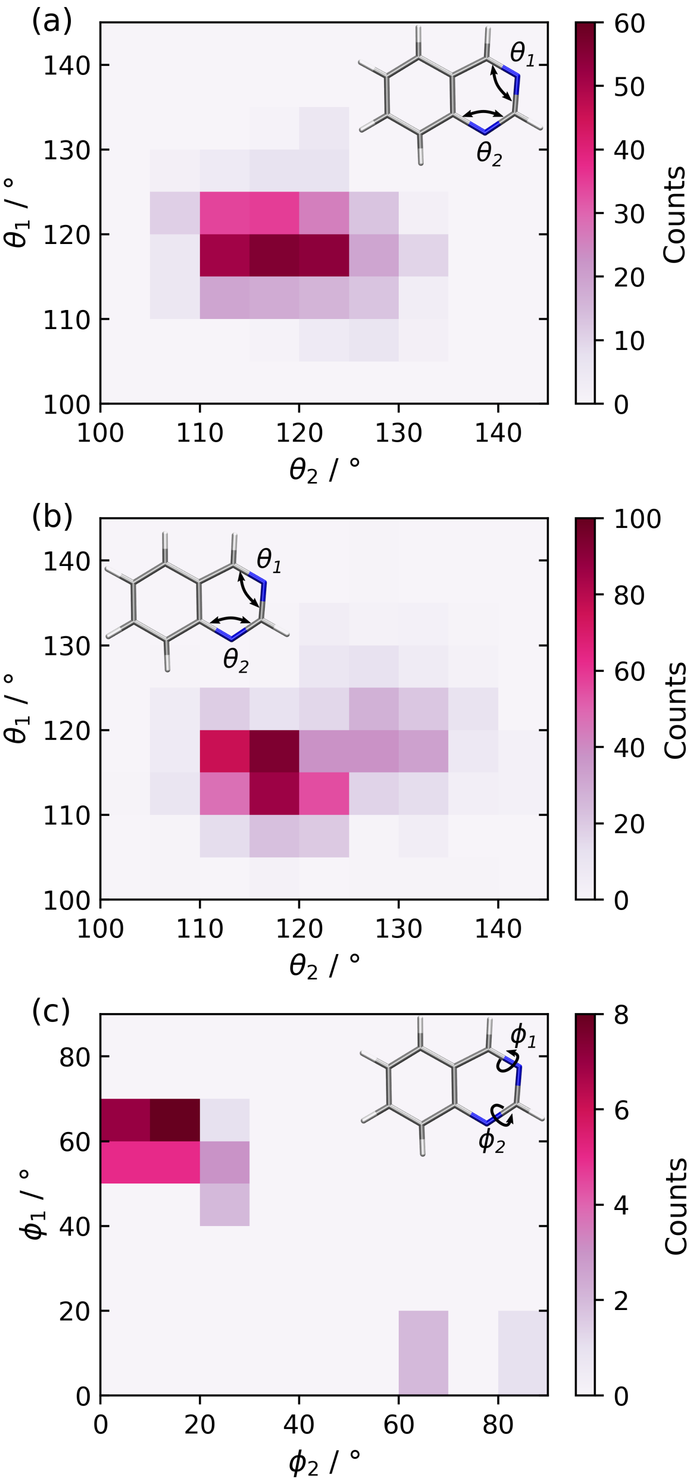

Figure 5.6: Two-dimensional histograms of the C_2−N_3−C_4 bond angle (θ_1) vs the C_{8a}−N_1−C_2 bond angle (θ_2) during hops from $S_3 \rightarrow S_2$ (a) and $S_2 \rightarrow S_1$ (b), as well as the C_2−N_3−C_4−C_{4a} dihedral angle (ϕ_1) vs the C_{8a}−N_1−C_2−C_3 dihedral angle (ϕ_2) during hops from $S_1 \rightarrow S_0$ (c), in quinazoline.

the ground state, compared to both isoquinoline and quinoline, and the ones that do, pass through regions resembling the S_1/S_0 MECI with the lower energy barrier.

5.3.3 Discrepancy in timescales between theory and experiment

From comparison of the simulated dynamics and the experimental lifetimes, summarised in Table 4.1, similar relative trends between molecules are obtained. Firstly, the decay from the initially excited S_3 state to S_1 (τ_1) is fastest in isoquinoline and quinoline, compared to quinazoline, and secondly, the sequential decay of the S_1 state (τ_2) is consistent with the ordering seen experimentally. However, there is a striking disparity in the magnitude of the timescales when comparing the simulations and the experiments. To quantify these differences, the population lifetimes for the three molecules were fitted using the procedure implemented in SHARC [50]. Only the τ_1 and τ_2 lifetimes were fitted, as the $T_1 \rightarrow S_0$ transition was not modelled in the simulations due to the limitations of SCS-ADC(2). Additionally, the ISC pathway from S_1 into the triplet manifold was not included due to the poor statistics and hence, τ_2 is assigned only to the $S_1 \rightarrow S_0$ pathway in the fitting procedure. The resulting fits and associated errors are presented in Table 5.1.

Table 5.1: Fitted population lifetimes from the trajectory surface hopping (TSH) simulations. The decay from $S_3 \rightarrow S_1$ *via* S_2 is ascribed to τ_1, whereas the subsequent pathway from $S_1 \rightarrow S_0$ is assigned to τ_2. The triplet states were omitted from the fitting procedure due to their small populations.

	τ_1 / fs	τ_2 / ps
Isoquinoline	35.4 ± 2.4	1.69 ± 0.13
Quinoline	46.8 ± 3.8	2.01 ± 0.16
Quinazoline	75.1 ± 4.1	8.64 ± 1.53

Although the lifetimes from the simulations in Table 5.1 follow a similar ordering to the experimental lifetimes in Table 4.1, it is evident that the lifetimes obtained in the simulations are significantly shorter. The τ_1 lifetimes are almost two orders of magnitude faster, while the τ_2 lifetimes are approximately an order of magnitude shorter. Therefore, to address these discrepancies, the SCS-ADC(2) method was benchmarked to attempt to identify any apparent issues with this electronic structure method, as previously it has been shown to give incorrect lifetimes [59]. Additionally, solvent effects were examined to determine if they might significantly influence the PESs.

5.3.3.1 Effect of the electronic structure

To investigate the effect of the electronic structure on the τ_1 lifetimes, the PE profiles shown in Fig. 4.3 that lead from the initially excited S_3 state in the FC region onto the S_1 surface have been benchmarked with XMS-CASPT2/cc-pVDZ. A (12,11) active space was used for isoquinoline and quinoline, whereas a (14,12) active space was utilised for quinazoline, due to the extra lone pair. The overall shape of the

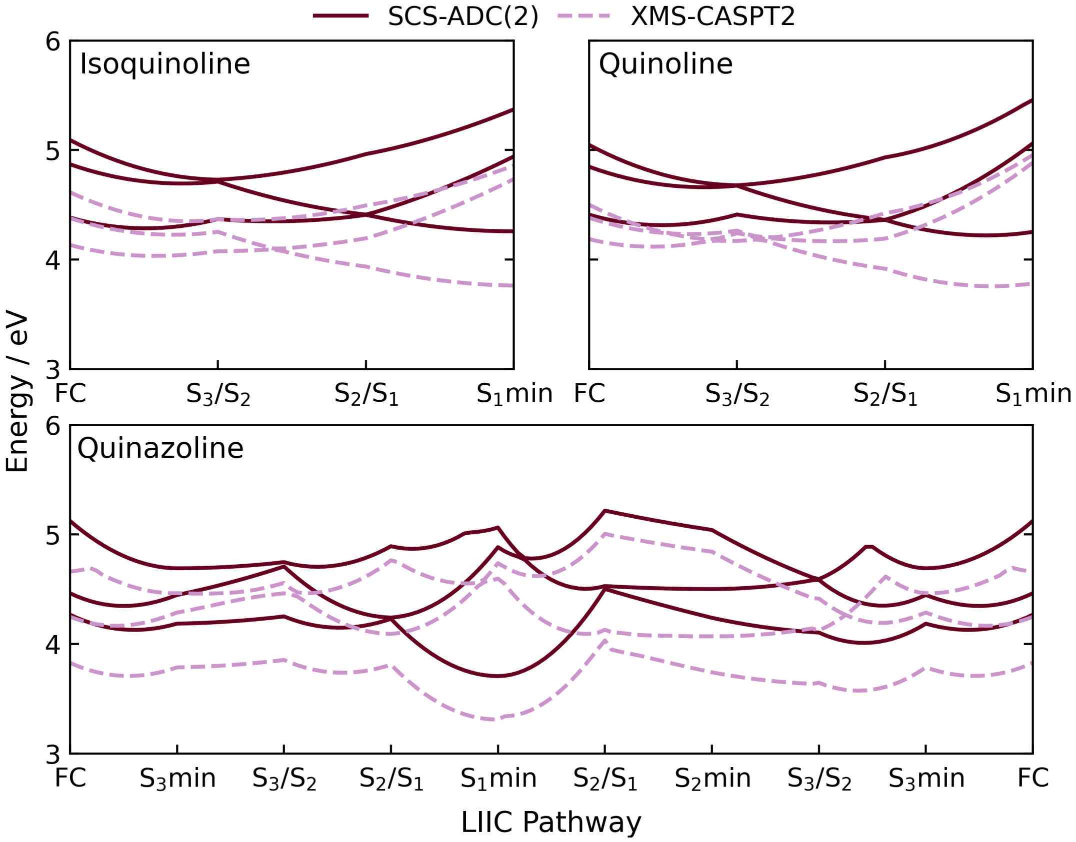

Figure 5.7: A comparison of the excited singlet states (S_{1-3}) between SCS-ADC(2)/cc-pVDZ (burgundy solid line) and XMS(8)-CASPT2/cc-pVDZ (lilac dashed line) along the SCS-ADC(2) photorelaxation pathways shown in Fig. 4.3, which lead to the S_1 surface, from the initially excited S_3 state in the FC region for isoquinoline, quinoline and quinazoline. A (12,11) active space was used for the XMS-CASPT2 calculations in isoquinoline and quinoline, whilst a (14,12) active space was necessary for quinazoline.

resulting XMS-CASPT2 PE profiles are qualitatively similar to the SCS-ADC(2) profiles, which can be seen in Fig. 5.7, however, the potentials are shifted down in energy, closer to the experimentally observed values. However, although the shapes of the PESs are similar, the gradients do differ subtly, resulting in crossings which occur at slightly different positions. This could influence the dynamics, but it does not satisfactorily explain why the τ_1 lifetimes from the simulations would be two orders of magnitude faster than those observed in the experiments.

Furthermore, the S_1 PESs in Fig. 4.5 have also been benchmarked using the same XMS-CASPT2 methods as above to determine whether the electronic structure accounts for the discrepancy in τ_2 lifetimes. As shown in Fig. 5.8, the S_1 potentials are qualitatively similar between XMS-CASPT2 and SCS-ADC(2), although SCS-ADC(2) seems to underestimate the barrier height to the S_1/S_0 MECIs from the S_1 ($^1n\pi^*$) minima in all three systems. The XMS-CASPT2 barrier heights on the SCS-ADC(2) pathways are 0.14 (0.06) and 0.19 (0.09) eV in isoquinoline and quinoline, respectively, and in quinazoline they are 0.42 (0.29) and 0.75 (0.50) eV, which is much larger in comparison to the SCS-ADC(2) values given in the brackets and shown in Table 4.1. These differences can be anticipated to have strong impact on the rates of decay from S_1, and so are good candidates for an explanation of the differences in magnitudes of τ_2 when comparing simulations and experiments.

The *relative* differences in barrier heights between the molecules are similar in both electronic structure methods, apart from the largest barrier in quinazoline. Hence, the *relative* rates of singlet decay to the ground state should be qualitatively correct across the three molecules, explaining why the correct overall pattern of timescales is seen. However, it is worth noting that the lower energy barriers in SCS-ADC(2) may affect the amount of triplet population seen in the simulations, especially in quinoline, where there is substantial SOC along the reaction coordinate that leads to ground state population. The reason for this is that the lower barrier to the S_1/S_0 MECI will lead to preferential population of the ground state, thus effectively reducing the triplet population. This is a possible explanation to why more triplet population is observed in the experiment compared to the simulations.

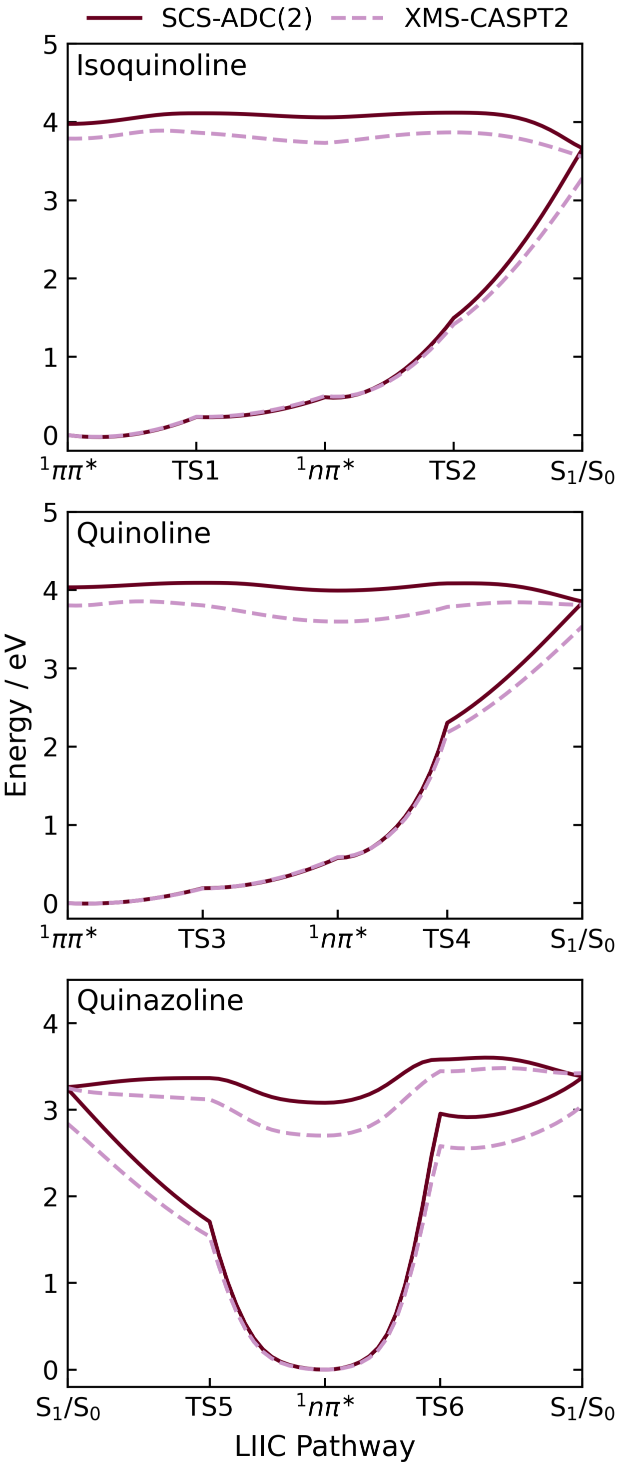

Figure 5.8: A comparison of the S_1 and S_0 states between SCS-ADC(2)/cc-pVDZ (burgundy solid line) and XMS(3)-CASPT2/cc-pVDZ (lilac dashed line) on the SCS-ADC(2) S_1 photorelaxation pathways shown in Fig. 4.5, for isoquinoline, quinoline and quinazoline. A (12,11) active space was used for the XMS-CASPT2 calculations in isoquinoline and quinoline, whilst a (14,12) active space was used for quinazoline.

While benchmarking with XMS-CASPT2 suggests that an underestimation of the barrier height may contribute to the faster τ_2 lifetimes, it does not account for the significant discrepancy between theory and experiment regarding the τ_1 lifetimes. Therefore, to explain this discrepancy, the effects of solvation are considered next, as these could possibly alter the shape of the PESs.

5.3.3.2 Solvent effects

It is important to highlight that the TAS experiments were performed in hexane solution, whereas the electronic structure calculations and nonadiabatic molecular dynamics simulations were carried out in the gas-phase. Although hexane is a non-polar solvent, it would be expected to have some effect on the dynamics and the lifetimes. Therefore, to examine the potential cause of the surprisingly fast τ_1

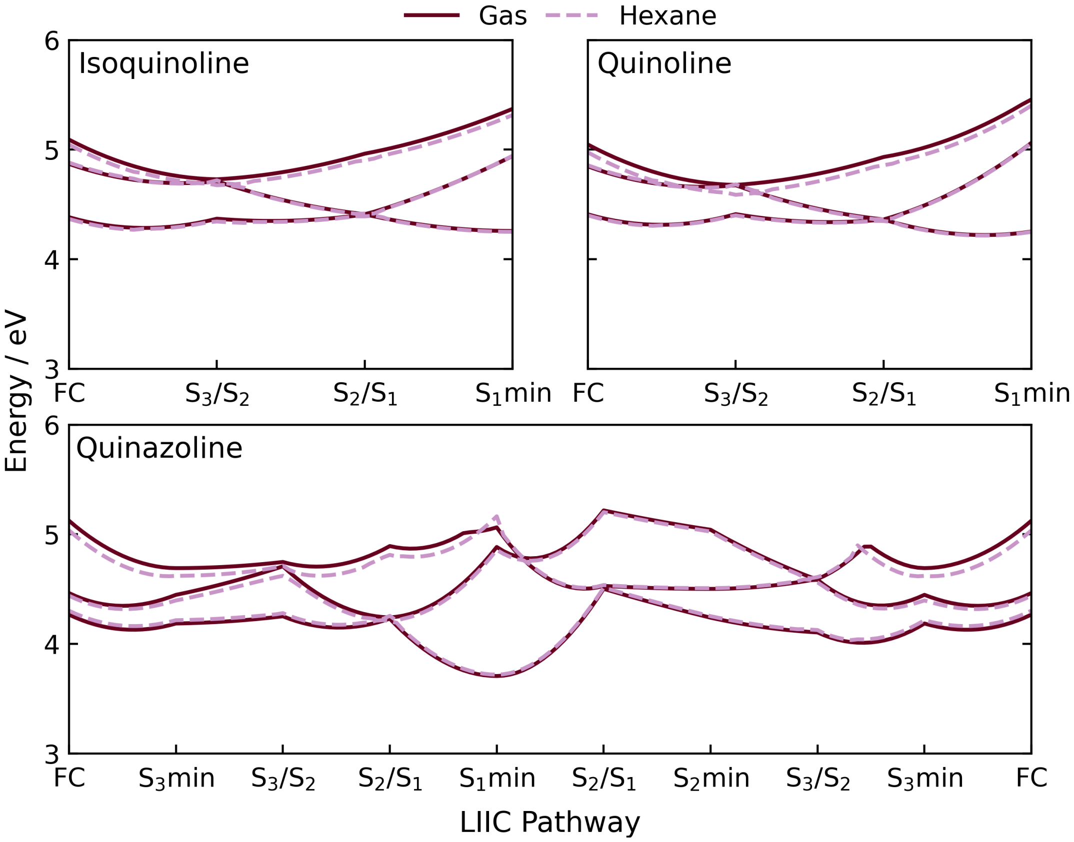

Figure 5.9: A comparison of the excited singlet states (S_{1-3}) between SCS-ADC(2)/cc-pVDZ in the gas-phase (burgundy solid line) and using COSMO to model hexane solvation (lilac dashed line) along the photorelaxation pathways shown in Fig. 4.3, for isoquinoline, quinoline and quinazoline.

lifetimes in the simulations, the effect of solvation on the SCS-ADC(2) pathways in Fig. 4.3 was explored using COSMO as an implicit solvation model for hexane [176]. The resulting PE profiles, shown in Fig. 5.9, closely resemble the gas-phase calculations, with the most noticeable differences being slight shifts in the S_3 states. However, these shifts alone are insufficient to explain the quite dramatically shorter τ_1 lifetimes. At the time of writing this thesis, explicit solvation modelling has not been explored in this project and hence, the full effect of hexane solvation remains somewhat uncertain at this stage.

For the τ_2 lifetimes, the S_1 PESs in Fig. 4.5 were re-calculated with implicit solvation, resulting in PE profiles that were very similar to the gas-phase calculations. These profiles are included in Fig. B.3, in an appendix, due to the limited insights they offer; although, it is interesting to note that the barriers decrease slightly with the inclusion of solvation effects. Overall, it is therefore suggested that the discrepancy in S_1 decay lifetimes could arise, at least in part, from an underestimation of the barrier heights with the SCS-ADC(2) method.

5.3.3.3 Possible solutions

Although there are no clear indications that the electronic structure method or solvation effects account for the significant discrepancy in τ_1 lifetimes between theory and experiment, several potential factors have been identified for future investigation to resolve this issue. Firstly, it is important to investigate whether an excess of kinetic energy is being introduced into the system, which could influence these lifetimes and the decay from the initially excited S_3 state to the S_1 state. A possible cause for this may be an inaccurate description of the excited state relative to the ground state or an issue related to the Wigner sampling method. To test this, dynamics without initial kinetic energy could be performed in order to determine if this adjustment slows the dynamics sufficiently to match the experimental lifetimes.

If this adjustment does not influence the lifetimes, a second approach involves using a linear vibronic coupling model to perform TSH simulations [182]. This would allow the use of a better electronic structure method, such as XMS-CASPT2, to parameterise the potentials, potentially resulting in more realistic surfaces and slower dynamics. Therefore, this approach could help determine whether subtle changes in the electronic structure contribute to the significantly shorter τ_1 lifetimes. Additionally, it would enable longer dynamics simulations, possibly with explicit solvation, allowing for a more thorough exploration of solvation effects [183].

5.4 Conclusion

The TSH simulations confirm the predictions from the electronic structure calculations in Chapter 4 that explain the results from the TAS experiments for three azanaphthalene systems. In terms of the timescale for decay to the S_1 state, the simulations reveal that isoquinoline and quinoline are faster compared to quinazoline, which is in agreement with the electronic structure calculations and the lifetimes from the TAS experiments. Particularly, quinazoline remains in the S_2 state longer than the other two molecules, attributed to the more complex S_2 PES observed in quinazoline. In addition, the trend in decay rates from the S_1 electronic state is also in accord with the TAS experiments, where isoquinoline is fastest followed by quinoline and finally, the rate in quinazoline which is much slower.

Geometry analysis at hopping points during the simulations identified the key features observed in the quantum chemical calculations. Monitoring the C−N−C bond angle in isoquinoline and quinoline at the $S_3 \rightarrow S_2$ geometries revealed that IC occurs at geometries located near the FC region, while IC to the S_1 state occurs at geometries with a larger bond angle, which falls in between the values for the $^1\pi\pi^*$ and $^1n\pi^*$ minima on the S_1 surface. Meanwhile, analysis of the dihedral angle at geometries where a $S_1 \rightarrow S_0$ hop occurs, shows that the CI seam is invariant to small changes in the magnitude of distortion out of the plane of the ring.

Additionally, quinazoline also displays similar features in the dynamics simulations compared to the electronic structure calculations, where IC from $S_3 \rightarrow S_2$ takes place at a wide range of θ_2 angles, consistent with the presence of two different S_3/S_2 MECIs. In contrast, IC onto the S_1 surface occurs near the FC region as a result of two pathways leading to the S_2/S_1 MECI with a geometry similar to the

FC region. Finally, the majority of trajectories that hop to the ground state pass through a geometry similar to the S_1/S_0 MECI with a lower energy barrier and again this CI seam is invariant to small changes in the dihedral angle.

Lastly, while the simulations and TAS experiments display similar relative trends between the three molecules, there are distinct differences in the lifetimes, with the simulations yielding significantly shorter lifetimes. The discrepancies in τ_2 lifetimes may stem from an underestimation of the barrier heights at the SCS-ADC(2) level. However, no definitive conclusion can be reached regarding the τ_1 lifetimes based on the current investigation of the effects of implicit solvation and the level of electronic structure theory employed. Therefore, further investigations are required, including exploring the impact of kinetic energy on the initial population decay by performing dynamics without initial kinetic energy. If this approach does not resolve the issue, a second method using a linear vibronic coupling model to perform TSH simulations with the electronic structure calculated at the XMS-CASPT2 level may be tested. This would help determine whether subtle changes in the electronic structure contribute to the significant differences in lifetimes. Additionally, explicit solvation effects may also be incorporated to further investigate the impact of the solvent on the dynamics. It would also be helpful to calculate observables explicitly from the simulations. In other contexts, for instance time-resolved photoelectron spectroscopies, there are examples where the measured timescales are strongly effected by e.g. windowing. In principle, something similar could be happening here. And at last, it is of course possible that there is something amiss with the experiment, rather than the theory.

6

N,*N′*-Dimethylpiperazine

6.1 Introduction

Photoinduced intramolecular charge transfer is an important photochemical process, which is involved in many molecular systems, such as photosynthesis [184, 185] and photovoltaic devices [186, 187]. Consequently, model systems are useful for understanding the underlying dynamic processes induced by photoexcitation. In particular, *N*,*N′*-dimethylpiperazine (DMP) has previously been used as a prototype system to study intramolecular charge transfer in the excited state [27, 188, 189]. DMP is a six-membered ring with C_{2h} symmetry in the ground state, leading to equivalent nitrogen atoms. Upon excitation into an electronic Rydberg state, charge transfer can occur from one nitrogen atom to the other.

Electronically excited DMP has been investigated experimentally using TRPES at multiple excitation wavelengths [188, 189] and UXS at 200 nm [27]. Deb *et al.* observed that excitation at 207 nm resulted in excitation into a charge-localised 3p state (3pL) [188]. IC then led to the formation of charge-localised (3sL) and charge-delocalised (3sD) conformers, with charge transfer occurring as the molecule explores the 3s PES. An equilibrium between these two structures on the 3s surface was established with a time constant of 2.65 ps. In the UXS experiment, representative molecular structures of these 3sL and 3sD conformers were determined, including all bond angles and atom-atom distances [27].

Although these experiments provided information about the 3sL and 3sD conformers, IC from the 3p to the 3s Rydberg state caused a loss of the vibrational coherence, as opposed to in *N*-methylmorpholine [159, 191, 192], and hence, intermediate TS structures, where the charge is transferring, were not distinguished. Therefore, the TRPES experiment has been repeated at 232 nm, which directly excites the 3s Rydberg state [189]. The resulting TRPES spectrum is shown on shorter timescales in Fig. 6.1 and on longer timescales in Ref. [189]. As shown in Fig. 6.1, a peak with a binding energy (BE) centred at 2.82 eV is observed shortly after excitation, and is attributed to the formation of the 3sL structure. Additionally,

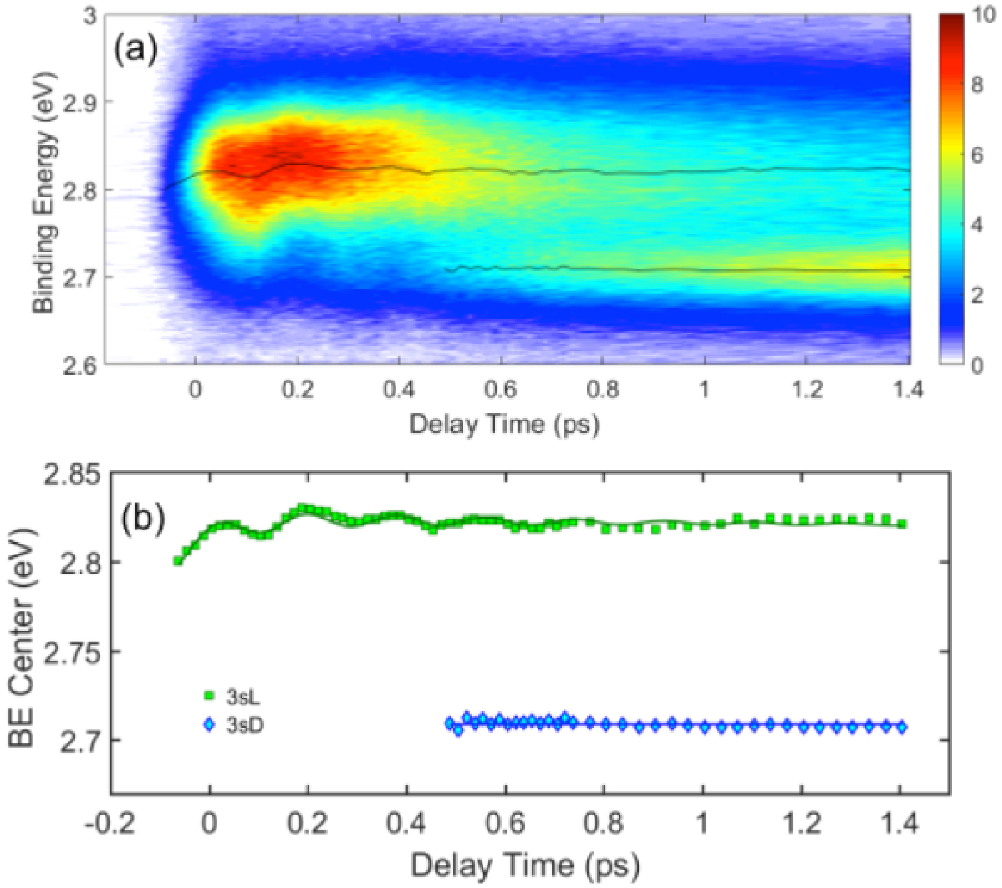

Figure 6.1: Time-resolved photoelectron spectrum of DMP (a) and the time-dependent binding energy (BE) centre position of the 3sL (green) and 3sD (blue) peaks (b), following excitation at 232 nm. The BE centres in (b) are fit to the data in (a). Figure adapted from Ref. [190].

oscillations in the BE are observed up to 500 fs, indicating coherent dynamics since the BE is sensitive to the molecular structure. After 500 fs, this peak begins to deplete as a separate peak arises at 2.71 eV ascribed to the 3sD structure.

Numerous theoretical studies have been conducted for DMP, approximating the 3s Rydberg state as the DMP cation, which has proved to be quite a controversial topic of discussion, as studies disputed whether a localised minimum exists in the cation [189, 193–195]. Recently, Reimann *et al.*, have shown that the 3s Rydberg electron binds more strongly to a localised charge distribution, which leads to a minimum on the 3s surface that is absent in the DMP cation [196]. Nevertheless, Reimann *et al.*, have shown both minima exist on the S_1 surface, which is the state probed in the TRPES and UXS experiments.

In this chapter, the charge transfer dynamics in DMP is explored, following excitation into the 3s Rydberg state (corresponding to S_1), in both a static and dynamic picture. Electronic structure calculations are used to locate the localised and delocalised minima, and the TS connecting these two structures. Next, excited state dynamics simulations are employed to map out the S_1 PES and gain insight into the timescales of these charge transfer processes. Lastly, to connect theory with experiment, the time-resolved photoelectron spectrum and time-dependent X-ray scattering signals are computed from the ensemble of trajectories and compared to previous experimental results.

6.2 Computational details

6.2.1 Electronic Structure

The electronic structure of neutral DMP was calculated at the SCS-CC2 [82, 83] level of theory with the aug-cc-pVDZ basis set. All SCS-CC2 calculations were performed using the Turbomole 7.7 software package [134]. The ground state minimum energy geometry was optimised and vertical excitation energies were computed from this geometry. The two minima on the S_1 surface, namely the 3sL and 3sD, were optimised using the experimentally determined structures as starting geometries for these optimisations [27]. All minima were confirmed by determining the vibrational normal modes. The TS linking the 3sL and 3sD structures on the S_1 surface was located by computing a MEP between these two minima and using the highest-energy geometry for an initial guess for the TS optimisation. The vibrational normal modes were computed to verify that the optimised structure contained one imaginary frequency. Additionally, an IRC calculation [141] confirmed that this TS leads to the 3sL and 3sD minima in the forward and reverse directions, respectively, on the S_1 surface.

PE profiles were constructed by LIICs from the ground state equilibrium geometry to the 3sL geometry, whereas MEP calculations were performed from the 3sL to the 3sD *via* the TS on the S_1 surface. The accuracy of these SCS-CC2 PE profiles were assessed by benchmarking with EOM-CCSD/aug-cc-pVDZ [84] and XMS(9)-CASPT2(4,6)/aug-cc-pVDZ [70]. The (4,6) active space, depicted by the black outline in Fig. 6.2, consists of four electrons in six orbitals, which includes both nitrogen lone pairs, the 3s Rydberg orbital and the $3p_{x,y,z}$ Rydberg orbitals. In these calculations the SA-CASSCF wave function was averaged over the

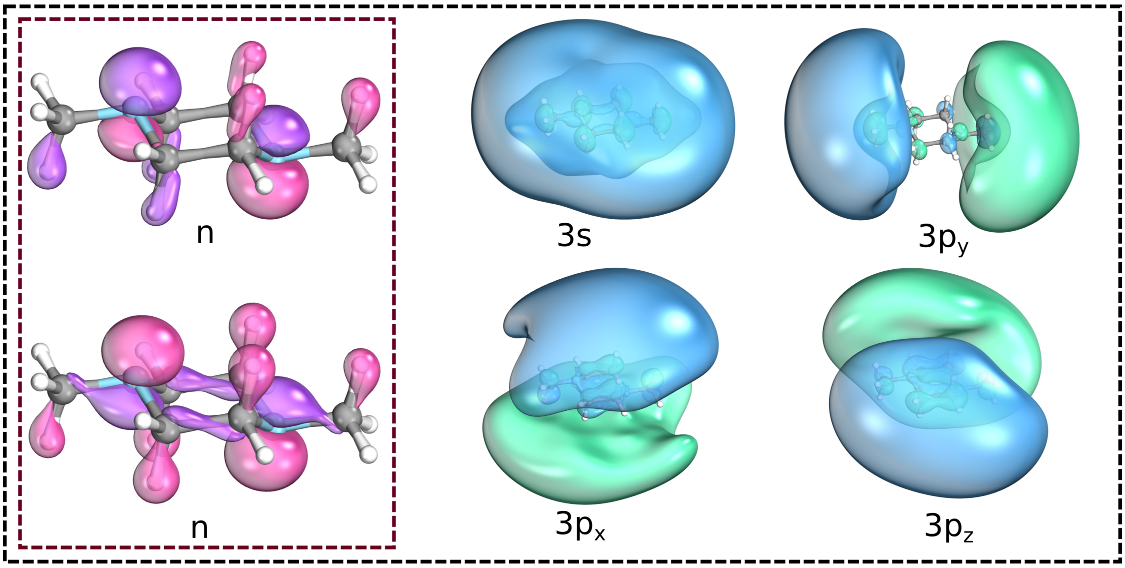

Figure 6.2: The (4,6) and (3,2) active spaces used for the XMS-CASPT2 calculations of neutral and cationic DMP, respectively. The (4,6) active space is outlined in black, and includes the two nitrogen lone pair orbitals as well as the 3s and $3p_{x,y,z}$ Rydberg orbitals, while the (3,2) active space outlined in burgundy only contains the two nitrogen lone pair orbitals.

nine lowest-lying singlet states. The XMS-CASPT2 calculations were performed with the BAGEL 1.1 software package [131] and all EOM-CCSD calculations were computed using the Orca 5.0.2 package [140].

Due to the multiconfigurational character in the ground state, the cation is not described well by the single-reference SCS-CC2 method and hence, the electronic structure of the cation was calculated at the XMS(2)-CASPT2(3,2) level of theory. This (3,2) active space is shown by the burgundy outline in Fig. 6.2, and contains three electrons in the two nitrogen lone pair orbitals. Additionally, the cation has been explored with the larger active space used in previous work [195, 196], which is composed of 11 electrons in 12 orbitals. These 12 orbitals are shown in Fig. 6.3 and include the two $CH_3{-}N$ σ, two C−C σ orbitals, two $CH_3{-}N$ σ^* and two C−C σ^* orbitals, in addition to the two nitrogen lone pair orbitals and the corresponding virtual orbitals, denoted n*. Finally, Reimann *et al.* demonstrated that the ion is also well described by IP-EOM-CCSD and hence, additionally, this method has been used for benchmarking purposes [196]. The aug-cc-pVDZ basis set has been used throughout for the cation calculations.

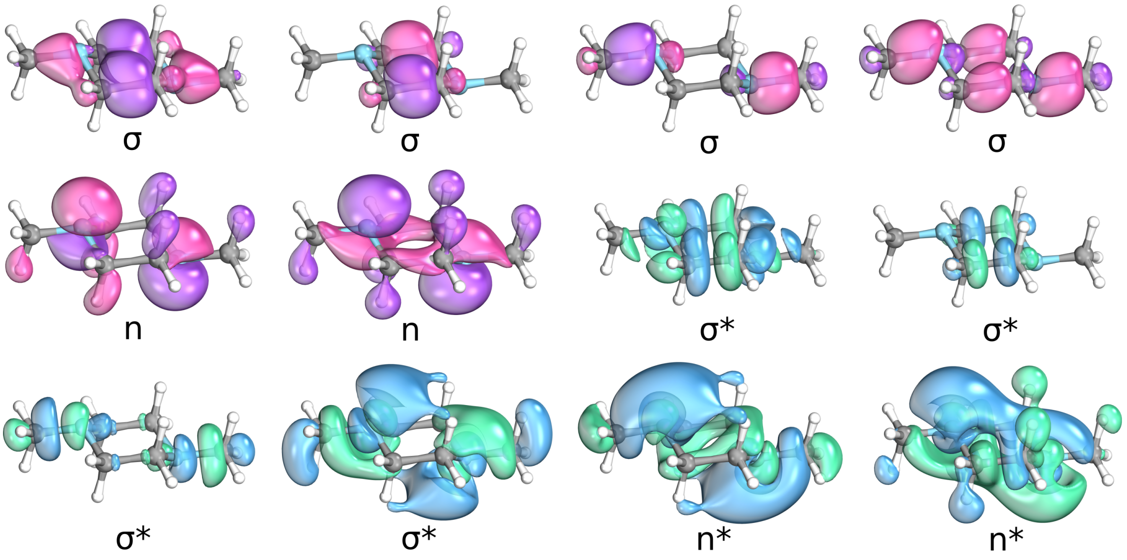

Figure 6.3: The larger (11,12) active space used for XMS-CASPT2 calculations of the DMP cation. This active space includes four sigma orbitals, the two nitrogen lone pair orbitals, four sigma antibonding orbitals, and the two nitrogen lone pair antibonding orbitals.

6.2.2 Absorption spectrum and nonadiabatic dynamics

The UV-vis absorption spectrum and the nonadiabatic molecular dynamics were performed at the CC2 level of theory with a custom basis set, where d-aug-cc-pVDZ is used for the nitrogen atoms and def2-SVP is used for all other atoms. Removing the SCS and changing to this custom basis set shows minimal effect on the shape of the PESs, which will be disccused later, and reduces the computational cost of the simulations. Therefore, the ground state geometry was re-optimised with CC2/d-aug-cc-pVDZ/def2-SVP and the vibrational normal modes were obtained. The UV-vis absorption spectrum was computed using the nuclear ensemble approach [149], calculating excitation energies and oscillator strengths for 6000 initial geometries obtained by sampling the Wigner distribution of the ground state harmonic oscillator for all vibrational normal modes. Initial conditions for the nonadiabatic dynamics simulations were selected from an excitation window of 4.66-4.74 eV, which is shifted from a central wavelength of 232 nm (5.34 eV) by 0.64 eV. This excitation window takes into account the difference in energies between the theoretical and experimental absorption spectra and ensures the correct state is excited.

The nonadiabatic dynamics were performed with Tully's fewest switches surface hopping algorithm [53] as implemented in the SHARC 2.1 software package [58, 135, 136] interfaced with Turbomole 7.7 [134], using a decoherence parameter of 0.1 Hartree [54]. The dynamics were propagated with a 0.5 fs nuclear time step and an electronic time step of 0.02 fs.

6.2.3 Time-resolved photoelectron spectrum

To compute the time-resolved photoelectron spectrum, XMS-CASPT2(4,6), for neutral DMP, and XMS(2)-CASPT2(3,2), for the DMP cation, calculations were performed every 2.5 fs along the CC2 trajectory pathways with the modified basis set used in the CC2 dynamics simulations. Dyson orbital and norm calculations were computed between between the active state in the dynamics simulations (S_1) and the two lowest-lying cationic states (D_0 and D_1). The photoelectron signal is calculated using Eq. 2.62, where the Gaussian function $g(\Delta t, E_{\mathrm{BE}})$ takes into the account the experimental cross-correlation between the pump and probe of 125 fs.

6.3 Results and discussion

6.3.1 Electronic structure

The ground state equilibrium geometry of DMP, included in Fig. 6.4 (a), has C_{2h} symmetry, where both nitrogen atom centres are equivalent. Therefore, the two lone pairs form an in-phase and out-of-phase linear combination, with the electron density delocalised over both atoms. Excitation can occur from either the in-phase or out-of-phase lone pair orbital into a Rydberg orbital, leading to an electronic Rydberg state. Vertical excitations for the eight lowest-lying singlet excited states (S_1-S_8) are shown in Table 6.1. The S_1 and S_2 states are both comprised of n3s character, where S_1 is associated with an excitation from the in-phase lone pair orbital into the 3s Rydberg orbital, whereas S_2 is associated with excitation from the out-of-phase lone pair orbital. The S_1 state has greater oscillator strength than S_2, and hence, upon excitation at the experimental wavelength of 232 nm (5.34 eV), this state would be populated. It is worth noting that the excitation energies at the SCS-CC2/aug-cc-pVDZ level are slightly lower in energy compared to experiment by ~0.2 eV, however, by benchmarking with the larger aug-cc-pVTZ

Table 6.1: Vertical excitation energies of DMP computed at the SCS-CC2/aug-cc-pVDZ level of theory from the ground state equilibrium geometry.

State	Transition	E_{exc} (eV)	f_{osc}	λ (nm)
S_1	n3s	5.53	0.031	224
S_2	n3s	5.57	0.000	223
S_3	n3p_y	5.92	0.000	209
S_4	n3p_z	5.98	0.000	207
S_5	n3p_y	6.02	0.224	206
S_6	n3p_z	6.05	0.013	205
S_7	n3p_x	6.17	0.000	201
S_8	n3p_x	6.19	0.039	200

basis set, it was shown that this shift in energy does not effect the shape of the PESs discussed in the next section.

6.3.1.1 The 3s Rydberg state surface

There are two minima on the S_1 surface, namely the 3sL and 3sD minima, shown on the left-hand side (LHS) and right-hand side (RHS) of Fig. 6.4 (b), respectively. At these geometries the S_1 state is comprised mainly of n3s character, with a small contribution of n3p character. The 3sL minimum breaks the C_{2h} symmetry as one nitrogen atom becomes sp^2 hybridised, which disrupts the orbital interaction and therefore, the electron density in the lone pair orbital localises on one of the nitrogen atoms. The 3sD minimum is largely distorted from the 3sL minimum, where both methyl groups are in an axial position, allowing orbital interaction and hence, the electron density delocalises over both nitrogen atoms. These minima are connected by a TS, where the imaginary frequency corresponds to the movement of the methyl groups.

The PES connecting the ground state minimum energy geometry to the 3sL minimum on the S_1 surface has been constructed by LIICs, and is shown in Fig.

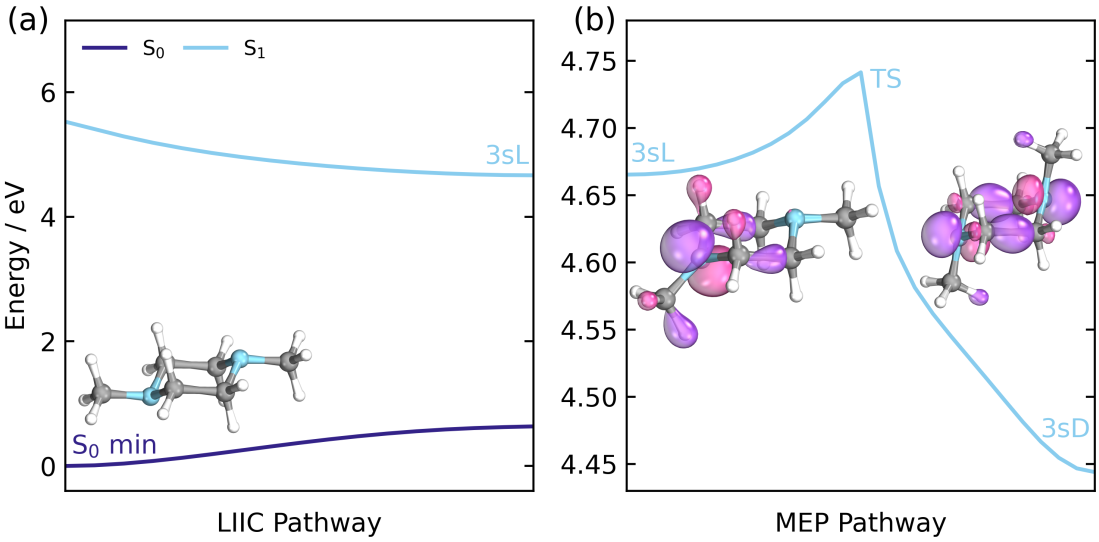

Figure 6.4: LIIC pathway connecting the S_0 minimum energy geometry of DMP to the 3sL geometry (a) and a MEP pathway from the 3sL to the 3sD *via* the optimised TS, computed on the S_1 surface (b). For clarity, the ground state has been omitted in (b). Both pathways are calculated at the SCS-CC2/aug-cc-pVDZ level of theory.

6.4 (a). Upon excitation into S_1, there is a barrierless transition to access the 3sL minimum and hence, is predicted to occur soon after excitation. To explore the PES from the 3sL to the 3sD minimum *via* the TS, MEPs were computed on the S_1 surface, where the resulting pathway is shown in Fig. 6.4 (b). Once in the 3sL minimum, there is an energy barrier of 0.08 eV to access the 3sD minimum and the reverse process has a barrier of 0.30 eV, as the 3sD minimum lies 0.22 eV below the 3sL minimum on the S_1 surface, identical to the experimentally determined value of 0.22 (0.04) eV [189]. Consequently, once the molecule has accessed the 3sD, it will likely be trapped around this minimum.

Although SCS-CC2 gives a good description of the relative differences between the two S_1 minima, the PESs shown in Fig. 6.4 have been benchmarked with two higher level methods: XMS(9)-CASPT2(4,6) and EOM-CCSD, to verify the shapes of these potentials. These potentials are shown in Fig. 6.5, where the S_0 and S_1 states are plotted for all three methods in (a), whilst only the S_1 surface in plotted in (b) for simplicity. Although not included in (b), the ground state is almost identical for all three methods, in both plots, as illustrated in (a). Furthermore,

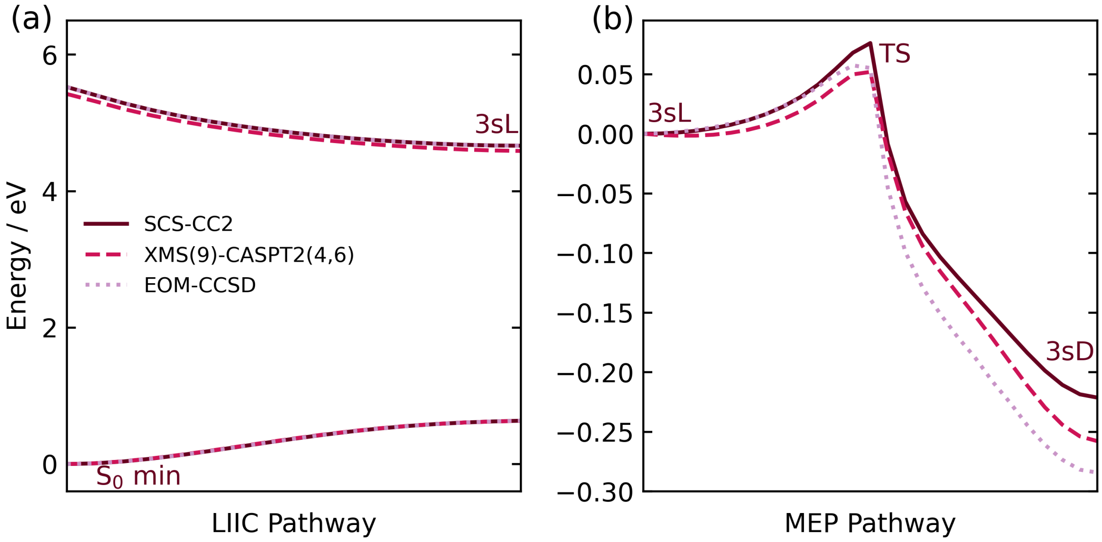

Figure 6.5: A comparison between SCS-CC2 (burgundy solid line), XMS(9)-CASPT2(4,6) (pink dashed line) and EOM-CCSD (lilac dotted line) on the LIIC and MEP pathways shown in Fig. 6.4. All calculations are performed with the aug-cc-pVDZ basis set. It should be noted that in (a) both the S_0 and S_1 states are shown, whereas in (b), only the S_1 surface is shown for simplicity with the S_1 energies relative to the 3sL geometry.

the S_1 PESs are consistently described by all three methods, where the barrier heights show relatively good agreement. Additionally, XMS(9)-CASPT2(4,6) gives a relative difference between the 3sL and 3sD geometries of 0.25 eV, which is within the error of the experimental value and EOM-CCSD is very slightly larger with a difference of 0.28 eV [189].

6.3.1.2 The DMP cation

To connect theory to experiment, eventually the photoelectron spectrum will be calculated from the dynamics simulations, which requires the cation to be computed additionally, in order to compute BEs and Dyson orbitals. Although the S_0 and S_1 states of DMP are described well by SCS-CC2, the DMP cation contains a highly multiconfigurational ground state in the FC region and hence, this method does not provide an adequate description of the cation. Additionally, Reimann *et al.* have outlined that many methods based on UHF fail to describe the ion correctly due to spatial symmetry breaking between the localised and delocalised geometries, leading to discontinuities on the PES [196]. However, these discontinuities can be removed by using SA-CASSCF approaches and IP-EOM-CCSD. Therefore, XMS(2)-CASPT2(3,2) is used here to calculate the cation across the PES pathways, shown in Fig. 6.4. In this (3,2) active space, the Rydberg orbitals have been removed from the (4,6) active space used to calculate the neutral molecule as they are not necessary for the ion calculation.

Firstly, as shown in Fig. 6.6, the ionisation potential of DMP, in the FC region, at the XMS(2)-CASPT2(3,2) level is 7.96 eV, which is an underestimation compared to the experimental value of 8.77 eV [197]. Although this will effect the raw BE values, the differences between the 3sL and 3sD BEs will be unaltered. It should also be noted that in the FC region, the D_0 and D_1 states are almost degenerate, however, moving away from this region to the 3sL geometry, these states diverge, where the D_0 PES follows a similar shape to S_1 and therefore, D_0 is the ionic state of interest. Moving from the 3sL to the 3sD structure, the S_1 and D_0 states follow different pathways, leading to a minimum existing on the S_1 surface at

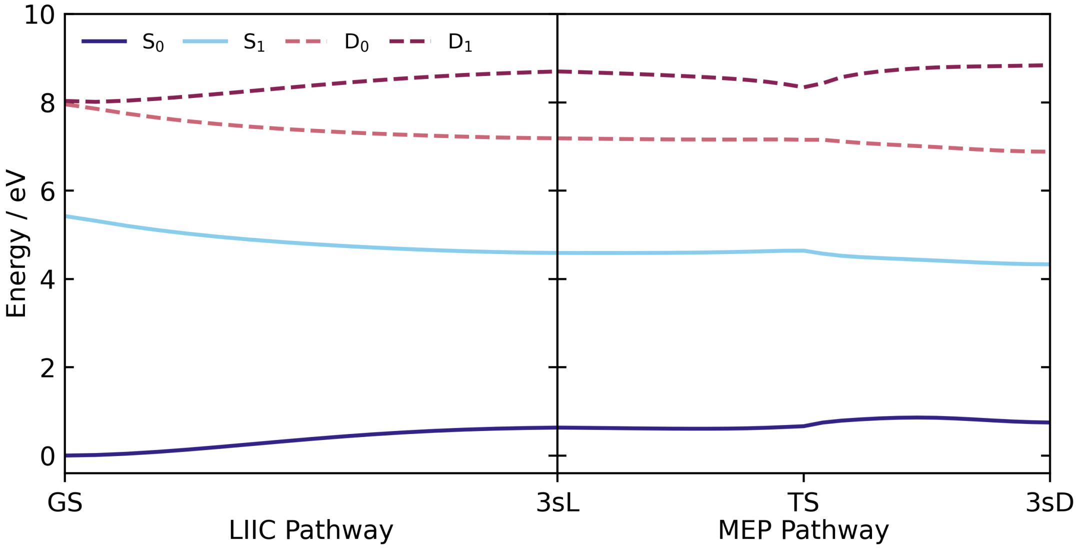

Figure 6.6: Calculation of the two lowest-lying singlet and doublet states, at the XMS(9)-CASPT2(4,6)/aug-cc-pVDZ and XMS(2)-CASPT2(3,2)/aug-cc-pVDZ levels, respectively, along the SCS-CC2/aug-cc-pVDZ pathways shown in Fig. 6.4.

the 3sL geometry, whereas on the D_0 surface, this minimum is absent. On the D_0 surface, the energy at the 3sD geometry lies 0.30 eV below the 3sL, which is slightly smaller than the experimentally calculated value of 0.33 (0.04) eV, however, is within the experimental error [189].

Even though the energy separation between the 3sL and 3sD geometries on the D_0 surface is comparable to experiment, the ion has been benchmarked with higher level methods to validate this PES. As there are limited methods that can describe the spatial symmetry breaking in the ion correctly, two tested by Reimann *et al.*, have been chosen: firstly, IP-EOM-CCSD and secondly, a SA-CASSCF(11,12) approach, although here a XMS-CASPT2 correction to the energies is applied [196]. These methods have been computed along the SCS-CC2 pathways, all with an aug-cc-pVDZ basis set, which can be seen in Fig. 6.7, where the energies are shown relative to the 3sL geometry. All methods are identical along the pathway from the ground state minimum energy geometry, in the FC region, to the 3sL, however, the methods start to differ moving from the 3sL to the 3sD, as they predict different relative energies between these two geometries. Both XMS(2)-CASPT2(11,12) and IP-EOM-CCSD predict a larger difference of 0.37 and 0.40 eV, respectively, compared

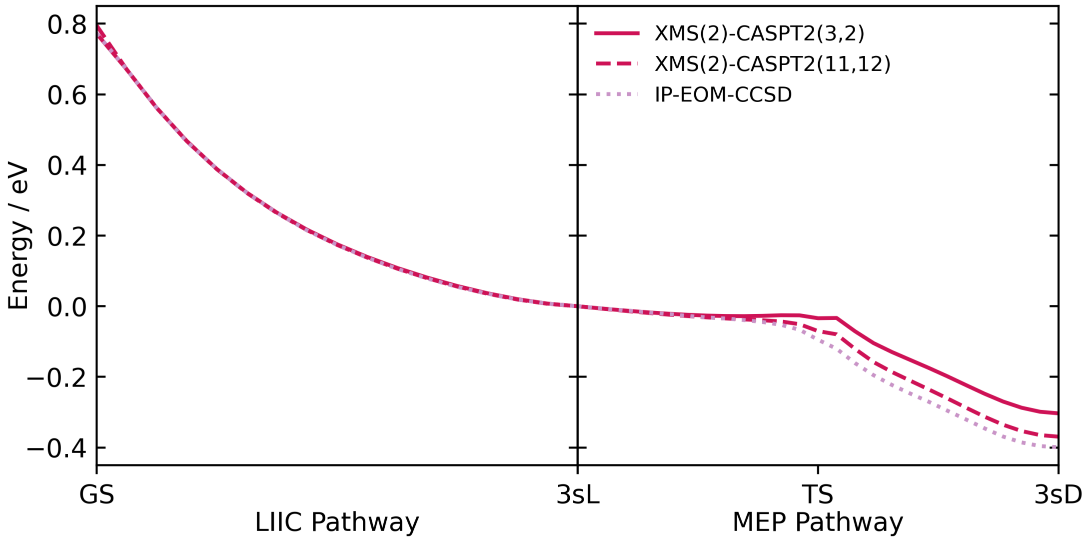

Figure 6.7: Benchmarking the D_0 state calculated at the XMS(2)-CASPT2(3,2) level (pink solid line), along the SCS-CC2 pathways shown in Fig. 6.4, at two different methods, namely XMS(2)-CASPT2(11,12) (pink dashed line) and IP-EOM-CCSD (lilac dotted line). The aug-cc-pVDZ basis has been used throughout and the resulting energies are shown relative to 3sL geometry.

to XMS(2)-CASPT2(3,2). Nevertheless, the XMS(2)-CASPT2(11,12) value is also within the experimental error, while the IP-EOM-CCSD is only slightly larger [189].

Due to the high computational cost, Rydberg orbitals cannot be added into the larger (11,12) active space to calculate the S_1 surface, therefore, XMS-CASPT2 with the smaller active space, and (IP)-EOM-CCSD are used to compute the BEs along the pathways. The BEs are taken as the difference between the D_0 and S_1 states, where the D_0 state has been calculated with XMS(2)-CASPT2(3,2) and IP-EOM-CCSD, while XMS(9)-CASPT2(4,6) and EOM-CCSD are used to calculate S_1. The resulting BEs along the pathways for both methods, can be seen in Fig. 6.8. Firstly, it should be noted that the BE values differ from the experimental values by ∼0.2 eV [188, 189], which is due to an underestimation of both S_1 and D_0 excitation energies. Despite this variation, (IP)-EOM-CCSD predicts a difference between the BEs at the 3sL and 3sD geometries of 0.12 eV, which is almost identical to the experimental value of 0.11 eV. Dissimilar, XMS-CASPT2 underestimates this value as 0.05 eV, which is due to an overestimation on the S_1 surface and an underestimation on the D_0 surface, between these two geometries. Although

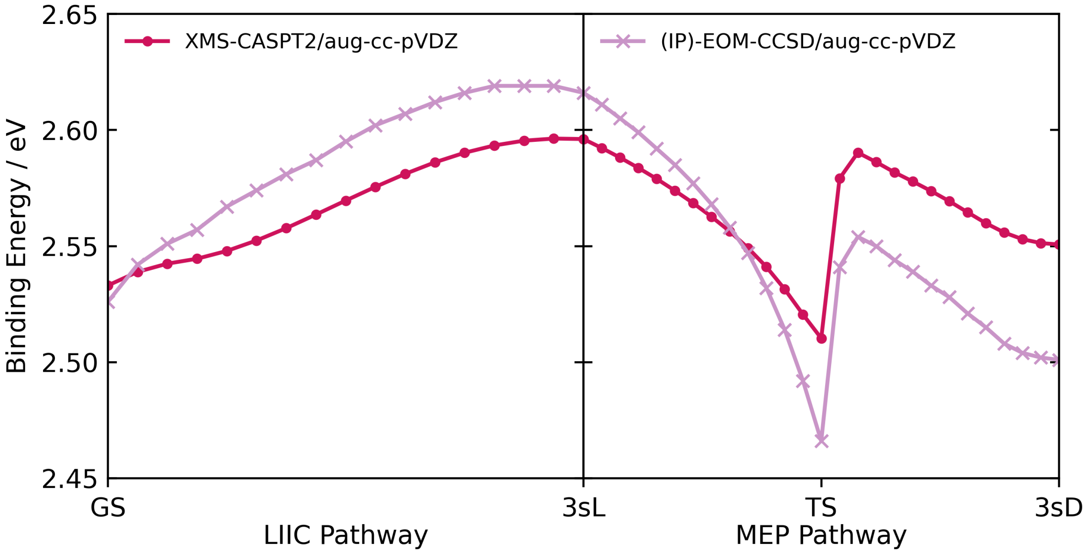

Figure 6.8: Binding energies (BEs) calculated across the SCS-CC2 pathways shown in Fig. 6.4 at the XMS-CASPT2/aug-cc-pVDZ (pink points) and (IP)-EOM-CCSD/aug-cc-pVDZ (lilac crosses) levels of theory. The BEs are computed as the difference between the D_0 and S_1 states, where D_0 state has been calculated with XMS(2)-CASPT2(3,2) and IP-EOM-CCSD, while S_1 has been calculated with XMS(9)-CASPT2(4,6) and EOM-CCSD.

XMS-CASPT2 underestimates this difference, the shape of the BEs curves across the pathways are qualitatively similar between the two methods.

6.3.1.3 Method for dynamics

Ideally, XMS-CASPT2, would be used to compute the nonadiabatic dynamics simulations and the Dyson orbitals and norms for the photoelectron spectrum. Unfortunately, this is extremely computationally demanding, and hence unfeasible. Therefore, a split method approach is needed, where the dynamics are calculated with a single-reference method and then XMS-CASPT2 is computed on these trajectory pathways in order to calculate Dyson orbitals. As shown in Fig. 6.5, SCS-CC2/aug-cc-pVDZ and XMS(9)-CASPT2(4,6)/aug-cc-pVDZ produced very similar PE profiles on the S_1 surface and hence, is suitable to use for the nonadiabatic dynamics simulations.

Although using this split method approach is more feasible, the aug-cc-pVDZ basis set is still relatively resource intensive and hence, the effect of basis sets along these pathways have been investigated for both SCS-CC2 and XMS-CASPT2. It was found that a basis of d-aug-cc-pVDZ on the nitrogen atoms and def2-SVP on all other atoms had a minimal effect on the S_1 PES for XMS-CASPT2, compared to aug-cc-pVDZ and actually improved the relative energy difference between the 3sL and 3sD minima, which can be seen in Fig. 6.9.

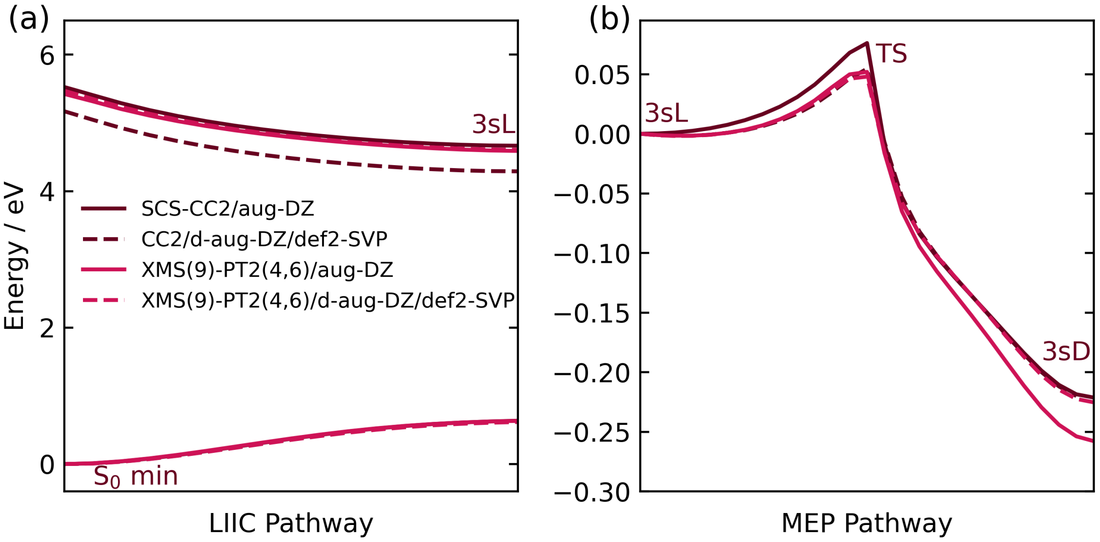

Figure 6.9: A comparison between SCS-CC2/aug-cc-pVDZ (burgundy solid line), CC2/d-aug-cc-pVDZ/def2-SVP (burgundy dashed line), XMS(9)-CASPT2(4,6)/aug-cc-pVDZ (pink solid line) and XMS(9)-CASPT2(4,6)/d-aug-cc-pVDZ/def2-SVP (pink dashed line) on the LIIC and MEP pathways shown in Fig. 6.4. The S_0 and S_1 states are shown in (a), whereas only the S_1 surface is shown in (b) with the S_1 energies relative to the 3sL geometry.

Minimal changes are observed on the PES from the FC region to the 3sL minimum with SCS-CC2/d-aug-cc-pVDZ/def2-SVP, not included in Fig. 6.9, however, there are large deviations on the S_1 surface from the 3sL to the 3sD, where the relative energy difference between the 3sL and 3sD is much smaller. Dissimilar, CC2 with this basis set produces a very similar PES shape for both pathways, compared to SCS-CC2/aug-cc-pVDZ, which is shown in Fig. 6.9, although the S_1 excitation energies are underestimated with CC2 compared to SCS-CC2. Nevertheless, this will not effect the dynamics simulations as long as the experimental excitation region is shifted to match the energies of CC2/d-aug-cc-pVDZ/def2-SVP.

6.3.2 Absorption spectrum

The UV-vis absorption spectrum was calculated with the nine lowest-lying singlet states at the CC2/d-aug-cc-pVDZ/def2-SVP level of theory and is shown in Fig. 6.10. The excitation energies are much lower with this method compared to the experimental spectrum, and therefore, a shift of 0.64 eV has been applied to

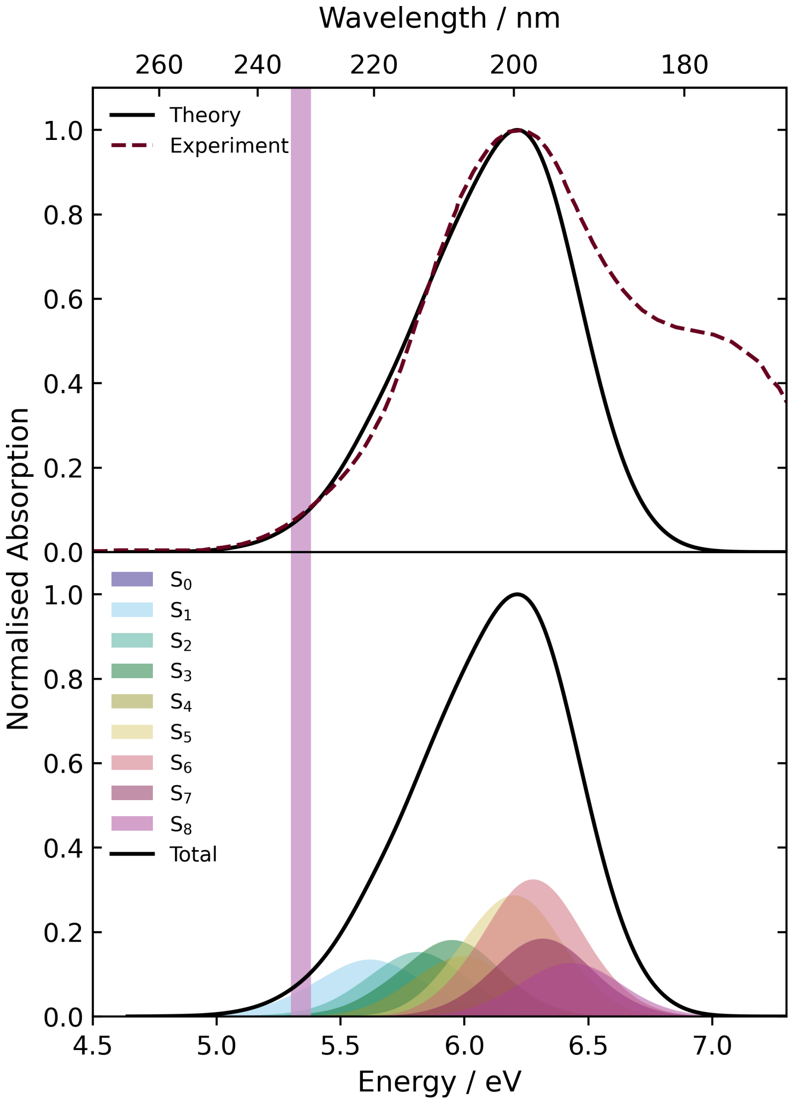

Figure 6.10: UV-vis absorption spectrum of DMP computed at the CC2/d-aug-cc-pVDZ/def2-SVP level of theory (black solid line) compared to the experimental spectrum (burgundy dashed line). A shift of 0.64 eV has been applied to the theory absorption spectrum to align the two spectra. Below, the theory spectrum is shown decomposed into contributing states. The excitation window, centred at 232 nm (5.34 eV) is show by the lilac shaded region in both plots.

the theory spectrum, in order to align the two spectra. There is one absorption band in the theory spectrum and with this shift, the peak maximum is around 6.2 eV (200 nm). As illustrated in the lower plot, all nine states contribute to this absorption band, with the peak centred around the optically bright $n3p_y$ state (S_5 in the FC region).

In comparison to the experimental spectrum, the shape of the main absorption band is very similar, however, at higher energies there is a shoulder in the experimental absorption spectrum, which is absent in the calculations. This shoulder is due to absorption into higher-lying 3d Rydberg states, which are not calculated here as they are not relevant for the nonadiabatic dynamics simulations. Finally, included in Fig. 6.10 is the excitation region centred around 5.34 eV (232 nm), which equates to 4.66-4.74 eV after removing the shift. This energy range ensures excitation occurs in the same region of the spectrum as the previous experiment for the nonadiabatic dynamics simulations [189]. As depicted in the lower plot of Fig. 6.10, this excitation window leads mainly to population of the S_1 state, however, a small number of initial conditions are excited into S_2 as well. Since only the lowest-lying excited state is populated experimentally in this region, only excitation into S_1 is accepted for the dynamics simulations. Additionally, this allows the use of CC2 as the electronic structure method in the dynamics simulations as it has previously been shown that CC2 is unstable in simulations where there are degeneracies between states [76].

6.3.3 Dynamics simulations

Nonadiabatic dynamics simulations of DMP were performed for 1.4 ps using an excitation window of 4.66-4.74 eV, allowing excitation only into the S_1 state. This led to 176 trajectories starting on this state, which is comprised of mainly n3s character in the FC region. All 176 trajectories remain in the S_1 state for the entirety of the simulations as there is no population transfer to the ground state, which is expected, as experimentally, long lifetimes in the 3s Rydberg state were observed in all studies [27, 188, 189].

6.3.3.1 Formation of the 3sD structure

As the 3sD geometry requires a large structural rearrangement from the ground state equilibrium geometry and the 3sL minimum, this structure can be detected in the dynamics simulations by calculating the root mean square deviation (RMSD) at each time step, compared to the optimised 3sD geometry, without taking into consideration the hydrogen atoms. The hydrogen atoms are excluded due to the fact that the C−H vibrational motion in the dynamics simulations leads to large deviations in their positions, compared to the optimised geometry, and hence, only the carbon and nitrogen backbone is used to calculate this value. Once the RMSD is determined, a cutoff value is used to dictate whether the trajectory is in a 3sD-like geometry. Therefore, in this case, if the RMSD is less than 0.26 Å, the geometry is deemed to be in the 3sD minimum. Figure 6.11 shows these raw 3sD populations for the ensemble of trajectories, as well as the populations convolved in time using a Gaussian with a FWHM of 125 fs, to take into consideration the time-resolution in the experiment [189].

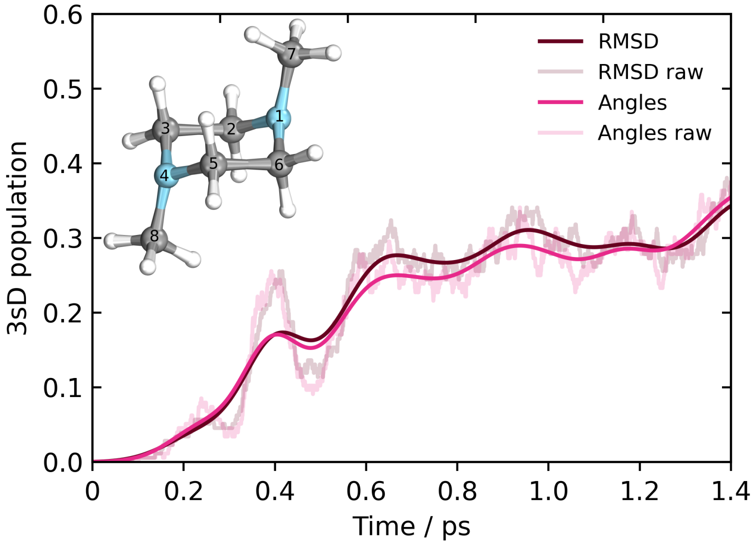

Figure 6.11: Population of DMP trajectories in the 3sD geometry over the time of the simulations, which was determined by either calculating the RMSD compared to the optimised 3sD structure (burgundy line) or computing the two $H_3C{-}N{-}N$ bond angles (pink line), at each time step. The geometry is deemed to be in the 3sD minimum if the RMSD is less than 0.26 Å or both $H_3C{-}N{-}N$ bond angles are less than 145°. The raw populations are presented for both methods in addition to the populations convolved in time using a Gaussian with a FWHM of 125 fs.

From the convolved RMSD populations in Fig. 6.11, it is observed that the 3sD population starts to rise rapidly after the first 0.2 ps, with a substantial amount of the 3sD structure seen at 0.4 ps, which is slightly earlier than the formation of the 3sD peak in the photoelectron spectrum, shown in Fig. 6.1, that appears at 0.5 ps. After this, overall, the population continues to rise over the time of the simulations, with small variations along the way. Interestingly, looking at the raw RMSD populations, there is a significant drop after 0.4 ps, which is almost absent once the convolution is applied, and hence, is not a feature in the experimental photoelectron spectrum due to the time-resolution. Furthermore, by the end of the simulations approximately 35% of the trajectories are in the 3sD geometry, which reflects the experiment as Cheng *et al.* observed that the 3sD peak intensity increased over hundreds of picoseconds, and the 3sL peak disappeared [189]. Thus, it is probable that if the simulations were run for longer the 3sD population would continue to increase.

Alternatively, the two H_3C-N-N bond angles ($C_7-N_1-N_4$ and $C_8-N_4-N_1$) can be monitored throughout the simulations, as they decrease from 152° in the ground state equilibrium geometry to 120° in the optimised 3sD minimum. Therefore, the geometry is assigned to the 3sD minimum if both angles are less than 145°, and these populations for the ensemble of trajectories based on the bond angles are also included in Fig. 6.11, with both the raw and convolved data shown. Using the bond angles to detect the 3sD geometry produces an extremely similar plot to the populations based on the RMSD, where all features are reproduced, hence, validating that the 3sD is being accurately tracked throughout the simulations.

6.3.4 Time-resolved photoelectron spectrum

To connect theory to experiment, the time-resolved photoelectron spectrum has been computed for the ensemble of trajectories. However, as discussed in Section 6.3.1.2, the cation cannot be accurately described with CC2; thus, a split method approach is employed. Consequently, the CC2 trajectory pathways are recalculated with XMS-CASPT2, using a (4,6) active space for the S_1 state, while the D_0 and D_1 ion states are computed with XMS-CASPT2(3,2). The photoelectron signal is obtained using Eq. 2.62, and the resulting spectrum is presented in Fig. 6.12. Since XMS-CASPT2 underestimates the binding BEs, as illustrated in Fig. 6.8, a constant energy correction of 0.25 eV has been added to the raw BEs.

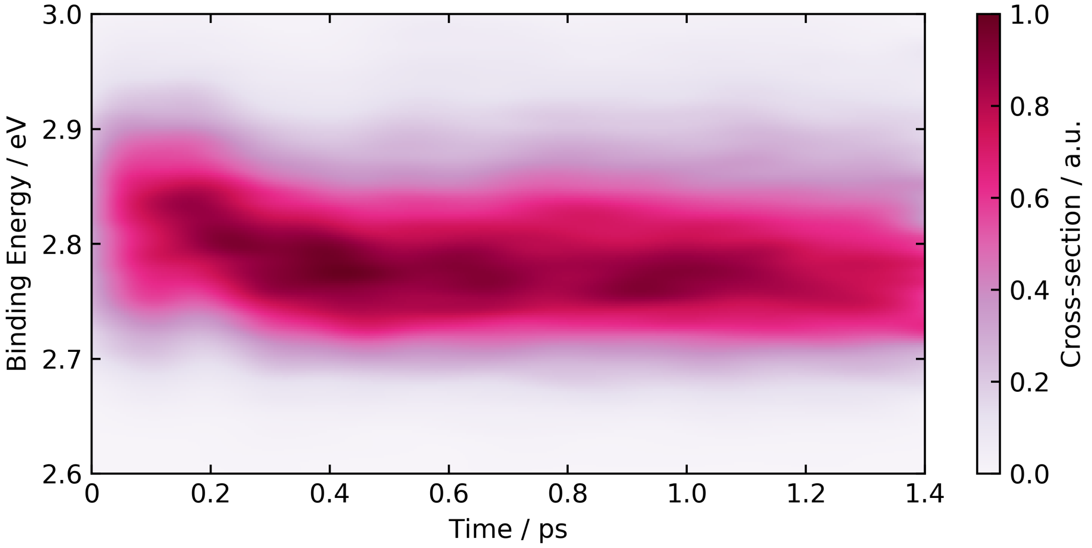

Figure 6.12: Time-resolved photoelectron spectrum of DMP calculated for the ensemble of CC2 trajectories with XMS-CASPT2, using a (4,6) active space for the neutral molecule and a (3,2) active space for the cation. These calculations have been performed with a d-aug-cc-pVDZ basis set on the nitrogen atoms and def2-SVP is used for all other atoms.

Compared to Fig. 6.1, the calculated spectrum in Fig. 6.12 shows significant differences. The computed spectrum exhibits a single broad peak, dissimilar to the experimental spectrum, which has two distinct peaks associated with the 3sL and 3sD geometries. As a result, no clear information about the formation of the 3sD structure can be extracted from this spectrum. However, within the first 0.2 ps, a small oscillation in the broad peak is observed, similar to the experimental result, followed by a downward shift in energy, which may indicate an increase in the population of the 3sD structure. Beyond this, no further insights can be drawn from the spectrum. Moreover, initial investigations computing the BEs with (IP)-EOM-CCSD have shown no significant improvement, which may indicate that the issue is not solely caused by the underestimation of BEs between the 3sL and 3sD geometries at the XMS-CASPT2(3,2) level.

As it is difficult to simultaneously calculate both the S_1 and ion states accurately for the ensemble of trajectories from the dynamics simulations, the time-resolved photoelectron spectrum has been computed using experimental BE values from Fig. 6.1, for the 3sL and 3sD peaks, in addition to the widths of these peaks and is shown in Fig. 6.13. Moreover, the raw RMSD 3sD populations in Fig. 6.11 have been utilised to define whether the molecule is in a 3sD geometry. If the geometry at time t is deemed to a be in the 3sD conformer, it is assigned a BE of 2.71 eV otherwise, a BE value of 2.82 eV is allocated. These values are then convolved using a Gaussian with a FWHM of 0.05 and 0.15 eV, respectively, and the total spectrum is then convolved in time.

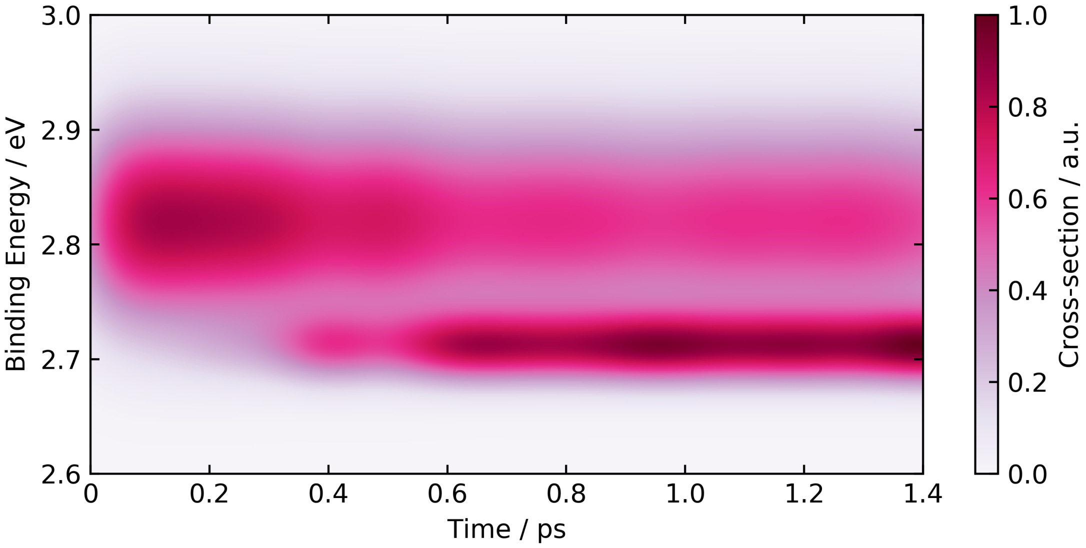

Figure 6.13: Time-resolved photoelectron spectrum of DMP for the ensemble of trajectories computed using experimental BE values and peak widths.

Using this metric, the spectrum based on the trajectories in Fig. 6.13, reproduces the main features from Fig. 6.1. Initially, a broad band centred at 2.82 eV appears soon after excitation and begins to deplete after 0.35 ps as a new band appears at 2.71 eV, attributed to the conversion from the 3sL to the 3sD. The formation of the band at 2.71 eV occurs slightly earlier than in experiment, where it appears after 0.5 ps, however, the timescale is on a similar order of magnitude. Additionally, the intensity of this band increases over the time of the simulation, as the population of the 3sD conformer rises, which is congruent with Fig. 6.1. The key difference between the spectra is the absence of BE oscillations in the theory, which arises from assigning a uniform BE of 2.82 eV to all geometries not classified as the 3sD and hence, coherent motion cannot be observed. Nevertheless, the overall agreement validates the dynamics simulations, particularly the conversion rate between the 3sL and 3sD minima, in comparison to experiment.

6.3.5 Ultrafast X-ray scattering

To calculate the UXS signal for the ensemble of trajectories, the IAM has been employed, which calculates the dominant signal due to structural dynamics. As discussed in Chapter 3, to compare with experiment, the calculated signals are represented as percent differences [153], defined as,

$$\Delta\% I(q,t) = 100 \times \frac{I(q,t) - I_{\mathrm{ref}}(q)}{I_{\mathrm{ref}}(q)}, \tag{6.1}$$

where $I(q,t)$ is the scattering signal at time t and $I_{\mathrm{ref}}(q)$ is the reference signal before the excitation pump is applied, which corresponds to the molecule in its ground state. Moreover, the percent differences are convolved in time with a Gaussian using a FWHM of 30 fs. Although UXS experiments have not currently been performed using a 232 nm excitation pulse, previous experiments were performed at 200 nm [27], where a time-resolution of 30 fs was achieved and hence, this resolution has been applied to the calculations as an approximation.

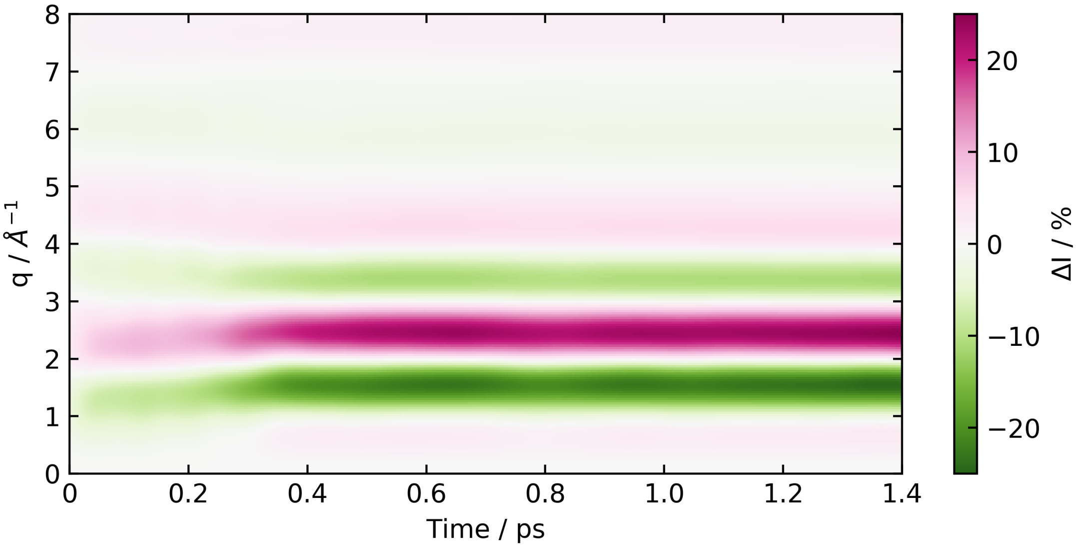

Figure 6.14: Time-dependent percent difference scattering signals for the ensemble of trajectories, throughout the simulations, calculated using the IAM.

The time-dependent percent difference total X-ray scattering signal for the ensemble of trajectories is shown in Fig. 6.14. Firstly, there are three main bands in the region of $q < 4$ Å^{-1}, which change over the time of the simulations, whereas the intensity of the scattering signal at $q > 4$ Å^{-1} remains relatively low for the entirety of the simulations and hence, not much information can be extracted from this region. The intensity of the three main bands increases after 0.3 ps, and the position of these bands are also altered, where the first two in the region of $1 < q < 3$ Å^{-1} shift slightly higher in q and the third band in the $3 < q < 4$ Å^{-1} region shifts to a slightly lower q value. These observations can be seen more clearly by plotting the scattering signal at different time delays of 0.1, 0.3 and 1.2 ps, which is shown in Fig. 6.15.

The variation in the scattering signal throughout the dynamics simulations can be attributed to the structural changes occurring on the S_1 surface. Therefore, the static scattering signals for the optimised 3sL and 3sD minima have been computed, and are shown in Fig. 6.16 as percent differences, using the ground state equilibrium as the reference geometry. From Fig. 6.16, it can be seen that the overall intensity of the scattering for the 3sD minimum is greater than for the 3sL, reflecting the larger geometrical change from the ground state equilibrium geometry. Additionally, the

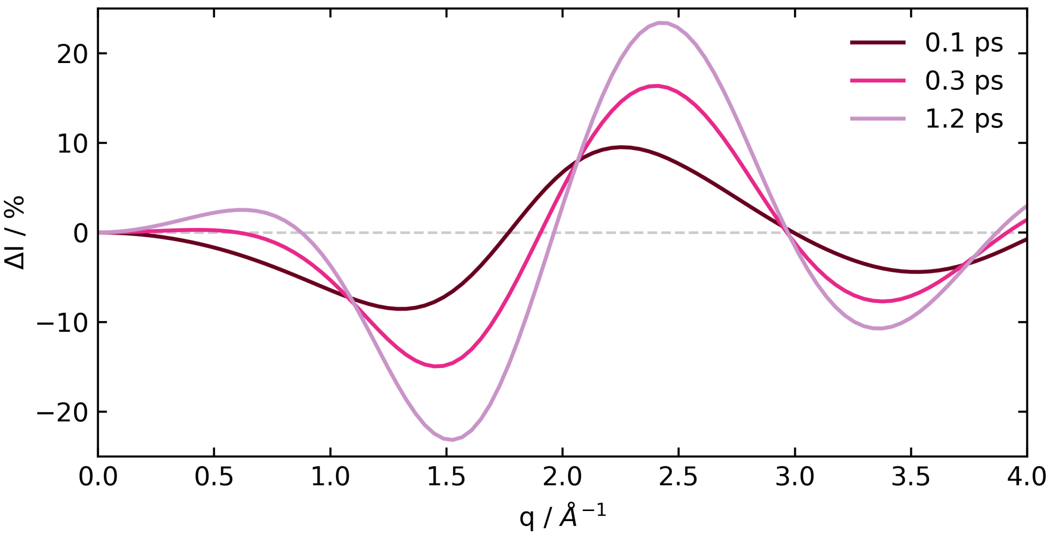

Figure 6.15: Percent difference scattering signals at given time delays (0.1, 0.3 and 1.2 ps) from the time-dependent percent difference scattering signals for the ensemble of trajectories shown in Fig. 6.14.

two peaks in the $1 < q < 3$ Å^{-1} range, also shift to a slightly higher q range from the 3sL to the 3sD. Thus, the changes seen in the time-dependent scattering signal can be ascribed to the increase in population of the 3sD structure. In particular, the signal at specific time delays shown in Fig. 6.15 can be related directly to the 3sD populations in Fig. 6.11, where at 0.1 ps there is very little population of the 3sD and hence, the scattering signal is mostly due to the 3sL geometry. At a time delay of 0.3 ps, the signal is larger and the three main peaks start to shift to different values of q, which is indicative of the rise in 3sD population seen in Fig. 6.15. Finally, at 1.2 ps the signal mirrors the static signal for the optimised 3sD geometry, characteristic of the larger amount of 3sD population.

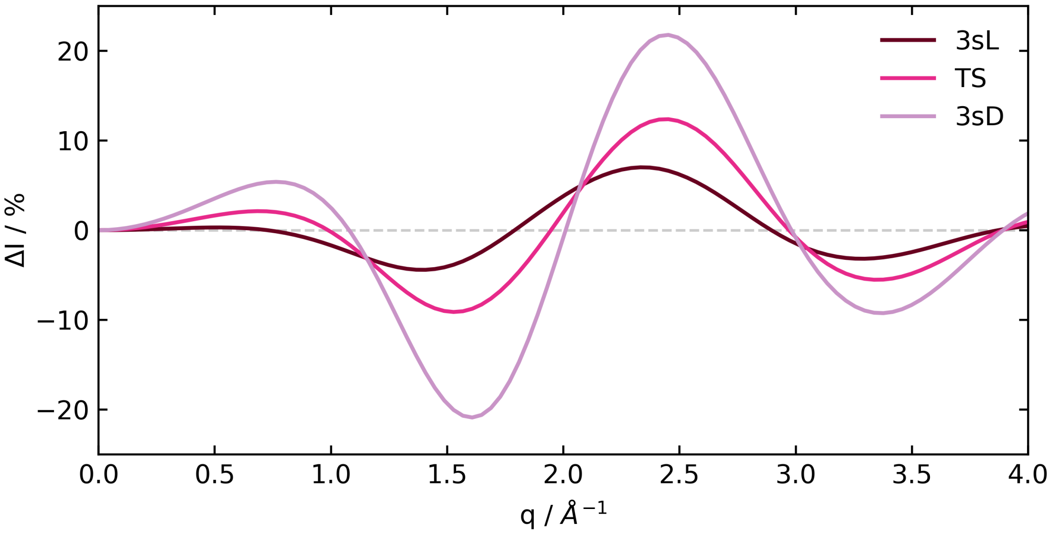

Figure 6.16: Percent difference scattering signals for the 3sL and 3sD minima as well as the TS on the S_1 surface connecting these two minima, computed with the IAM, where the ground state minimum energy geometry of DMP is used as a reference. All structures were optimised at the SCS-CC2/aug-cc-pVDZ level of theory.

6.3.5.1 Comparison to experiment

In comparison to the UXS experiments performed with a 200 nm excitation pulse [27], the time-dependent scattering signal displayed in Fig. 6.14 is very similar, where after 0.3 ps the positions of the three main bands at $q < 4$ Å^{-1} are almost identical. It should be noted that the percent difference values in the experiment are ∼10% of the calculated values, which is due to the fact that experimentally, the excitation fraction was only $9.4 \pm 0.3\%$ and here, the calculated scattering signal is computed assuming 100% excitation. Nevertheless, even with this difference accounted for, the intensity of the peak at $q \approx 2.5$ Å^{-1} seems to be slightly underestimated in the calculations, which can be seen more clearly when comparing the individual experimental 3sL and 3sD percent difference patterns to the signals for the these two optimised geometries at the SCS-CC2/aug-cc-pVDZ level, shown in Fig. 6.16.

Although there are some subtle differences in the scattering signals between experiment and the theory presented here, the main difference is the relative shift of the $q \approx 1.5$ Å^{-1} and $q \approx 2.5$ Å^{-1} peaks for the 3sL and the 3sD conformers, which is more distinguishable in the theory. Interestingly, the experimental 3sL scattering pattern reflects the optimised TS pattern, also included in Fig. 6.16, more closely. At the SCS-CC2/aug-cc-pVDZ level of theory, the TS geometry has one axial methyl group compared to the 3sL minimum, where this methyl group is in between an axial and equatorial position. Additionally, there are also minor differences in the ring structure between these two geometries. Therefore, this reflects that small changes to the molecular geometry can affect the signal significantly and hence, it is likely that in reality the 3sL conformer resembles a geometry more similar to the optimised TS. Finally, it should be noted that the signal at $q \leq 1$ Å^{-1} differs in most of the computed signals compared to the experiment due to electronic effects resulting from electron density redistribution in excited electronic Rydberg states [159, 198], which in future could be investigated with *ab initio* scattering [97, 98, 163, 164].

6.4 Conclusion

The electronic structure calculations and excited state dynamics simulations uncover the photoinduced charge transfer mechanism occurring on the 3s Rydberg state in DMP, highlighting the existence of a TS that links the charge-localised minimum to the charge-delocalised minimum on the S_1 surface. The significant structural rearrangement that accompanies charge delocalisation on the S_1 state makes this structure easily identifiable in the simulations. Moreover, the conversion from the charge-localised to charge-delocalised geometries occurs on a similar rate consistent with the previous experiment.

Calculating observables for TRPES from the ensemble of trajectories has been challenging due to the difficulty of simultaneously obtaining an accurate description of both neutral DMP and the cation, with a method that is computationally feasible. The cation is especially difficult to model because of its multiconfigurational nature in the FC region, which necessitated the use of a split-method approach. However, this approach still fell short, as the time-resolved photoelectron spectrum provided limited information, displaying only a single broad peak instead of two distinct peaks for the charge-localised and charge-delocalised structures. A more successful strategy involved incorporating experimental parameters and using the population of the charge-delocalised structure in the simulations to assign BE values corresponding to either the charge-localised or charge-delocalised peaks at a given time.

Finally, UXS signals were predicted using the ensemble of trajectories and the IAM. After 0.3 ps, the bands shift to different values of q, corresponding to the increasing populations of the charge-delocalised geometry. Compared to the experimental results, there are subtle differences in the peak positions for the charge-localised conformer, reflecting that the total scattering is highly sensitive to the molecular geometry. Additionally, discrepancies at low q arise due to the exclusion of electronic effects, which could be further explored in the future using *ab initio* scattering methods, as demonstrated in Chapter 3.

7

Conclusions

7.1 Summary

The research presented in this thesis demonstrates that theoretical simulations provide valuable insights into the underlying mechanisms of photodynamical processes and enhance the interpretation of cutting-edge ultrafast experiments. Multiple electronic structure methods have been employed to compute ground and excited electronic states across a span of energies and molecular geometries relevant to the photochemical dynamics of the molecules of interest. These electronic structure calculations have been benchmarked extensively, with the topography of the states carefully analysed. Additionally, these methods have been coupled with trajectory surface hopping (TSH) to compute the nonadiabatic dynamics. Where applicable, these dynamics simulations were used to calculate observables, enabling direct comparisons with experimental data.

Specifically, in Chapter 3, the dynamics of cyclopentadiene (CP) upon photoexcitation were thoroughly explored. The simulations revealed that, on short timescales, the system encounters a conical intersection seam, which results in either the formation of the bicyclo[2.1.0]pentene (BP) photoproduct or the regeneration of CP on the ground state. On longer timescales, two key reactions were identified on the hot ground state, including the conversion of BP back to CP. To complement these findings, X-ray scattering signals for the ensemble of trajectories were predicted using the independent atom model (IAM). These calculations were performed prior to the experiments, providing essential guidance on what features to expect in the data and were later instrumental in interpreting the experimental results. Additionally, the influence of electronic effects on the scattering signal was examined, which may be detectable in future experiments, potentially enabling the monitoring of excited state population transfer.

Next, Chapter 4 investigated the photochemical trends in a static picture across a series of six azanaphthalene molecules, each differing by the nitrogen atom(s) positions. Here, electronic structure calculations were used to explain the observations from recent transient absorption spectroscopy (TAS) experiments, which identified three distinct lifetimes related to internal conversion (IC) to the S_1 state, first, the competition between IC to the ground state and intersystem crossing (ISC) into the triplet manifold from S_1, second, and the dynamics in the triplet state, third. Significant differences in the propensity for ISC vs IC were observed in the experiments across the molecular series, affecting the rates of deactivation. The calculations effectively account for the observed patterns of photochemical behaviour, which can be attributed to spin-orbit coupling (SOC) effects and potential energy (PE) barriers. The ability of these calculations to achieve detailed agreement with experimental data across six molecules with subtle variations in their composition exemplifies how theory can complement experimental findings and highlights future opportunities for the rational design of photoactive molecules.

Following on, in Chapter 5, nonadiabatic simulations were conducted on a representative subset of azanaphthalenes, highlighting interesting cases from the TAS experiments that exhibit varying lifetimes and propensities for ISC. The simulations qualitatively agree with the predictions from Chapter 4, showing that the decay to S_1 and its subsequent decay align with the trends predicted by the quantum chemical calculations and follow the same relative patterns observed in the TAS experiments. However, large discrepancies exist between the magnitudes of the lifetimes from the simulations and those measured in the TAS experiments. The issue with the

S_1 decay lifetime is tentatively attributed to an underestimation of the PE barrier heights, but no clear conclusions have been reached regarding why the lifetimes ascribed to the initial decay to S_1 are approximately two orders of magnitude faster than those observed experimentally, indicating a need for further investigation.

Finally, Chapter 6 studied the photoinduced charge transfer dynamics in N,N'-dimethylpiperazine (DMP) upon excitation into a Rydberg state. The transition state (TS) was located between the two excited state minima, facilitating the charge transfer process. Excited state dynamics simulations revealed that the molecule slowly transitions from the charge-localised minimum to the charge-delocalised minimum, proceeding at a rate comparable to previous experiments. Although calculating observables for time-resolved photoelectron spectroscopy (TRPES) experiments has been challenging due to the difficulties in accurately describing both DMP and its cation simultaneously, this study has provided a more in-depth understanding of the charge transfer mechanism on the excited state. Additionally, it presented an interesting case for using the CC2 method in dynamics simulations, as only one excited state needed to be modelled.

In conclusion, a key takeaway from this thesis is that detailed computational analysis can both rationalise experimental results and provide a more qualitative understanding of the underlying chemistry. This approach can potentially lead to the development of design rules for chemical engineering. Furthermore, the connection between theory and experiment allows for the benchmarking of theoretical calculations, helping to identify their limitations and areas of applicability. This combined approach is particularly valuable for studying complex molecular systems where experimental techniques are difficult or offer only a partial understanding of the total dynamics. Only by combining theoretical and experimental methods can a comprehensive understanding of the true dynamics be achieved.

7.2 Outlook

This thesis leaves some questions unanswered, particularly regarding discrepancies between theory and experiment, while also opening new directions for further research. For instance, in the case of CP, additional ultrafast experiments could be interpreted using the model developed in this work. Specifically, TRPES experiments have already been conducted [199], and therefore, observables can be calculated from the ensemble of trajectories presented in Chapter 3 to aid the interpretation of these measurements. This would provide a further test of our current model of CP photochemistry, especially since the relevant ion states need to be calculated using the same electronic structure method, something which has not been attempted yet. Furthermore, ultrafast electron diffraction (UED) has also been utilised to study the photoexcited dynamics in CP [200], with observable calculations for this technique currently underway, again with the goal of aiding the interpretation of the experimental data.

Additionally, the effect of adding methyl groups to the carbon atoms in CP has been investigated experimentally using both TRPES [199] and UED [200]. Studies on 1,2,3,4-tetramethylcyclopentadiene and 1,2,3,4,5-pentamethylcyclopentadiene have shown slower dynamics compared to CP, where the methyl groups seem to also influence the photoproducts formed. Simulations could assist in interpreting these experiments and provide a better understanding of the underlying photorelaxation mechanisms. However, these molecules present a more challenging case than CP due to the presence of low-lying Rydberg states. Moreover, these simulations would be significantly more computationally demanding, due to both the size of the molecules and the slower dynamics, adding an extra layer of complexity.

Regarding the azanaphthalene dynamics, some unresolved issues remain concerning the magnitude of the timescales observed in the simulations compared to experiments. While it has been determined that the ground state population appears more quickly in the simulations due to an underestimation of the barrier heights using SCS-ADC(2), no clear explanation was found for the large discrepancy in the decay from the initially excited state down to S_1, despite extensive benchmarking with XMS-CASPT2 and exploring the effect of implicit solvation on the calculations. Moving forward, one of the three molecules, such as isoquinoline, could be chosen for further investigation, as it exhibits the simplest dynamics. A starting point could involve testing whether the molecule has too much initial kinetic energy, and how this impacts the timescales of the dynamics. If no significant change is seen, another route is to explore the use of a linear vibronic coupling model to perform TSH simulations, which would allow higher-level electronic structure methods, such as XMS-CASPT2, to be utilised. This approach would help assess whether subtle changes in the electronic structure leads to notably different dynamics. Moreover, one could consider explicit solvation modelling. A final potential avenue of research for this project would be to calculate TAS observables from the simulations to provide a more comprehensive comparison with the experimental data.

In attempting to calculate TRPES observables for DMP, discrepancies were observed between the experimental data and the electronic structure calculations. Interestingly, a simple experimentally parametrised model showed good agreement with the experimental results, suggesting that the underlying dynamics were largely accurate. This points to a possible issue either with the calculated binding energies (BEs) or with the regions explored during the dynamics simulations. Therefore, future research should seek to understand this discrepancy further, particularly assessing whether it stems from using a different electronic structure method to calculate the BEs compared to the one used for the dynamics simulations.

Further developments in this study include exploring the photoinduced charge transfer dynamics in N,N'-dimethylhomopiperazine (DMHP), a seven-membered ring with an extra CH_2 moiety in the ring compared to DMP. Recent TRPES experiments on DMHP revealed similar characteristic peaks associated with the charge-localised and charge-delocalised structures as seen in DMP [201]. However, the dynamics appear to differ significantly, with large binding energy oscillations in the charge-localised peak and population oscillations between the two bands, which are not observed in DMP. Moreover, the conversion to the charge-delocalised structure occurs over a longer timescale. Therefore, the aim is to compare and contrast the dynamics simulations of these two molecules and identify the features that lead such distinct dynamics.

Overall, this thesis highlights the importance of theory in advancing the understanding of photoinduced dynamical processes. Our investigations of three complex molecules have demonstrated how computational simulations can be used to both interpret experimental observations and offer guidance for future experiments. These studies, along with future explorations, emphasise the ongoing efforts to combine theory with ultrafast experiments in order to further the field of photochemistry.

Appendices

A

Calculation of absorption spectra

The absorption spectra presented in this thesis were calculated using the nuclear ensemble approach [149], as implemented in SHARC [50]. In this approach, the ground state wave function is sampled using a method of choice, with Wigner sampling employed here to generate the initial geometries. For each geometry k, single-point calculations are performed to compute the excitation energies $E_{k,\alpha}$ and oscillator strengths $f^{\mathrm{osc}}_{k,\alpha}$ for the electronic states of interest α. This results in a stick spectrum, which is then convolved with a Gaussian function to produce a broadened spectrum. Therefore, the photoabsorption cross-section for each geometry is expressed as,

$$\sigma_k(E) \propto f^{\mathrm{osc}}_{k,\alpha}\exp(c(E - E_{k,\alpha})^2), \tag{A.1}$$

where c is related to the full width at half maximum (FWHM) by,

$$c = -\frac{4\ln(2)}{\mathrm{FWHM}^2}. \tag{A.2}$$

The overall photoabsorption cross-section is then summed over all the geometries following,

$$\sigma(E) = \sum_{k}^{N} \sigma_k(E). \tag{A.3}$$

The nuclear ensemble approach is a widely used and effective method for calculating absorption spectra, providing a relatively straightforward way to simulate electronic transitions from a ground state distribution of molecular geometries. However, this approach has some limitations, particularly its inability to describe vibrational structure. This arises from the fact that the nuclear ensemble method does not explicitly calculate the overlap between vibrational wave functions of the ground and excited states. Therefore, alternative methods such as Franck-Condon calculations can be employed to calculate these vibrational peaks [132].

B

Additional potential energy surfaces

B.1 Cyclopentadiene

To identify a suitable DFT functional for propagating ground state dynamics, five DFT functionals were benchmarked against the ground state PE profiles, obtained using XMS(3)-CASPT2(4,4)/cc-pVDZ, shown in Figs. 3.5 and 3.6 (b). The selected

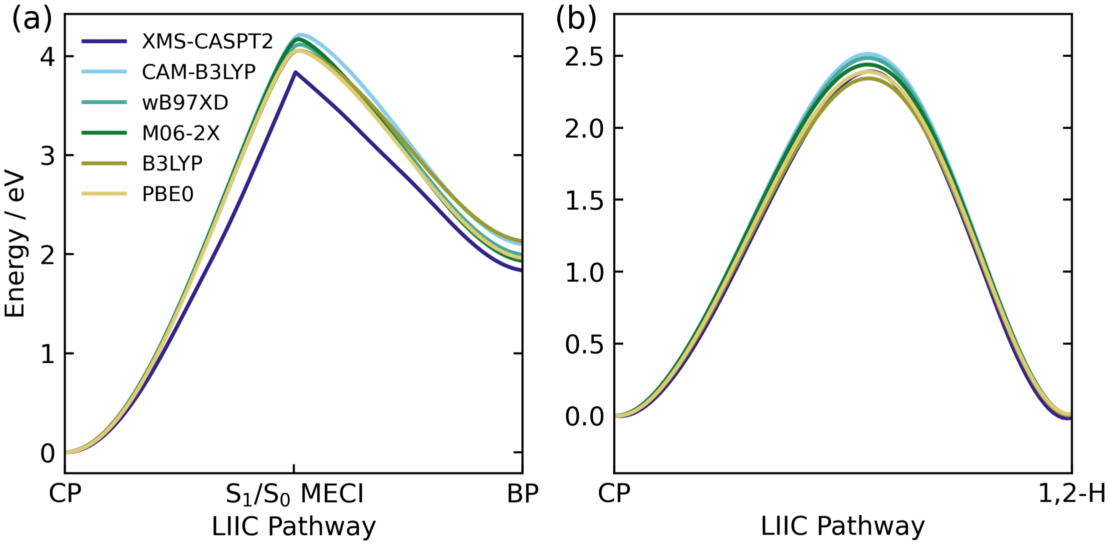

Figure B.1: Benchmarking five different DFT functionals compared to XMS(3)-CASPT2(4,4)/cc-pVDZ energies along the LIIC pathway from the S$_0$ minimum in CP to the photoproduct BP *via* the S$_1$/S$_0$ MECI and from the S$_0$ minimum in CP to 1,2-hydrogen shift product. All DFT functionals were computed with the def2-SV(P) basis set.

functionals were CAM-B3LYP, wB97XD, M06-2X, B3LYP and PBE0. Given the need for computational efficiency to allow for up to 10 ps of ground state dynamics, the def2-SV(P) basis set was employed. The resulting PESs are presented in Fig. B.1 (a) and (b). The PBE0 functional yielded the most similar energies compared to XMS-CASPT2 along both of these pathways, and hence, was chosen for the ground state dynamics simulations.

B.2 Azanaphthalenes

B.2.1 Potential energy profiles to the S_1 state

The PE profiles from the initially excited S_3 state (S_4 in 1,6- and 1,8-naphthyridine) to the S_1 surface in isoquinoline, quinoline, quinazoline, quinoxaline, 1,6- and 1,8-naphthyridine, shown in Fig. 4.3 in the main text, are also included below in Fig. B.2 with all excited states displayed.

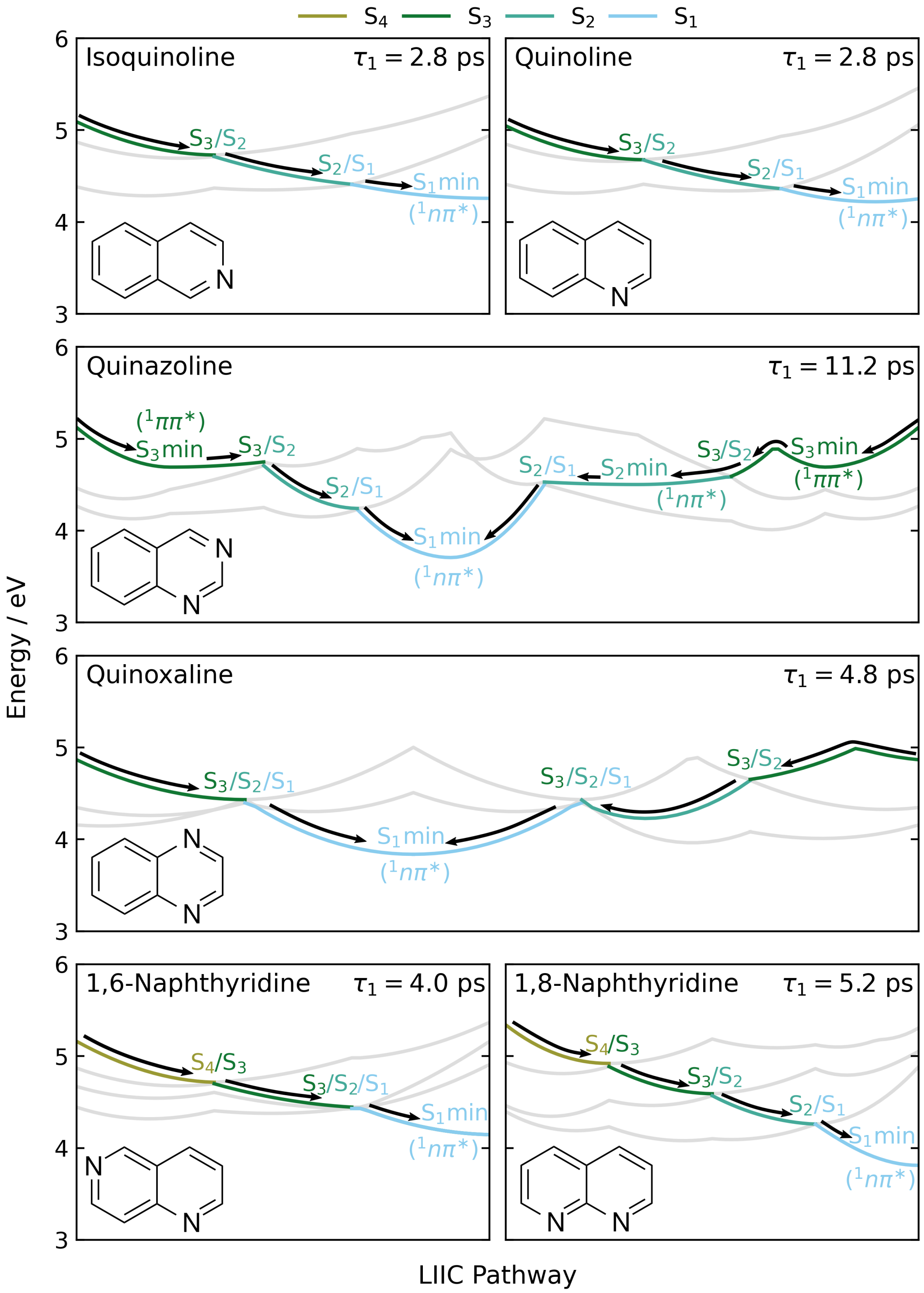

Figure B.2: Potential energy profiles of the photorelaxation pathways from S$_3$ (S$_4$ for 1,6- and 1,8-naphthyridine) onto the S$_1$ surface, shown in Fig. 4.3, with all excited states shown. The inactive states along the pathways are shown in light grey.

B.2.2 Benchmarking with COSMO

The comparison between SCS-ADC(2)/cc-pVDZ in the gas phase and with the implicit solvation model COSMO to represent bulk hexane solvation for the S_1 PES plots (Fig. 4.5) in isoquinoline, quinoline, and quinazoline is shown in Fig. B.3. The plots are almost identical, though the barriers decrease marginally when hexane solvation is included.

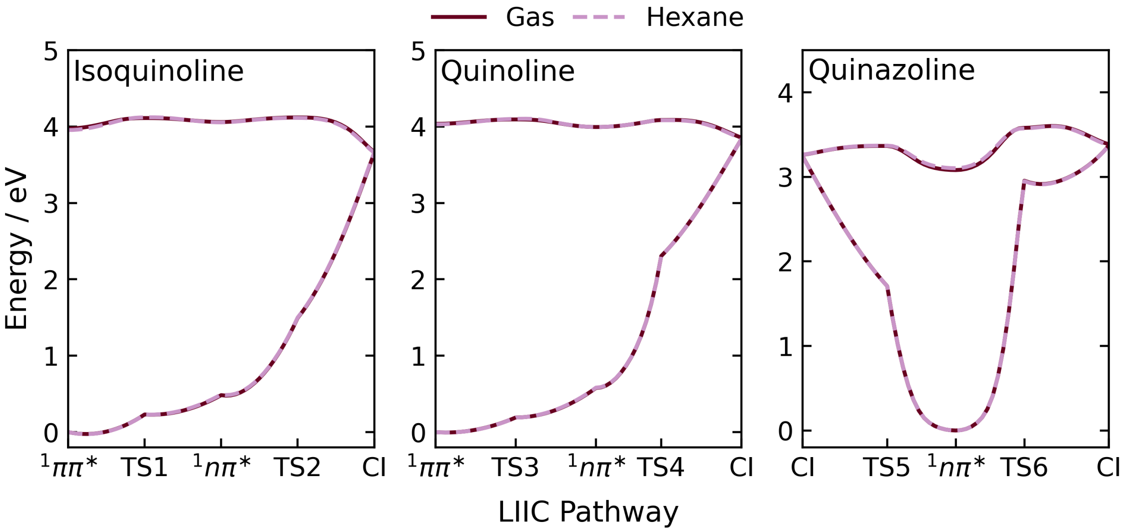

Figure B.3: A comparison between SCS-ADC(2)/cc-pVDZ in the gas phase (burgundy solid line) and using the COSMO as an implicit solvation model for hexane (lilac dashed line) along the S_1 photorelaxation pathways shown in Fig. 4.5, for isoquinoline, quinoline and quinazoline.

Bibliography

[1] H. Gaffron and E. W. Fager, *Annu. Rev. Plant. Physiol.*, 1951, **2**, 87–114.

[2] Q. Wang, R. W. Schoenlein, L. A. Peteanu, R. A. Mathies and C. V. Shank, *Science*, 1994, **266**, 422–424.

[3] S. Hahn and G. Stock, *J. Phys. Chem. B*, 2000, **104**, 1146–1149.

[4] H. Kandori, Y. Shichida and T. Yoshizawa, *Biochemistry (Mosc)*, 2001, **66**, 1197–1209.

[5] E. Tapavicza, A. M. Meyer and F. Furche, *Phys. Chem. Chem. Phys.*, 2011, **13**, 20986.

[6] E. Havinga, R. J. de Kock and M. P. Rappoldt, *Tetrahedron*, 1960, **11**, 276–284.

[7] N. A. Anderson, J. J. Shiang and R. J. Sension, *J. Phys. Chem. A*, 1999, **103**, 10730–10736.

[8] S. Mamba, D. S. Perry, M. Tsige and G. Pellicane, *J. Phys. Chem. A*, 2021, **125**, 10593–10603.

[9] J. Fu, Q. Yang, P. Huang, S. Chung, K. Cho, Z. Kan, H. Liu, X. Lu, Y. Lang, H. Lai, F. He, P. W. K. Fong, S. Lu, Y. Yang, Z. Xiao and G. Li, *Nat. Commun.*, 2024, **15**, 1830.

[10] S.-J. Zou, Y. Shen, F.-M. Xie, J.-D. Chen, Y.-Q. Li and J.-X. Tang, *Mater. Chem. Front.*, 2020, **4**, 788–820.

[11] N. Thejo Kalyani and S. J. Dhoble, *Renew. Sustain. Energy Rev.*, 2012, **16**, 2696–2723.

[12] B. Li, Z. Wang, S.-J. Su, F. Guo, Y. Cao and Y. Zhang, *Adv. Opt. Mater.*, 2019, **7**, 1801496.

[13] M. Lan, S. Zhao, W. Liu, C.-S. Lee, W. Zhang and P. Wang, *Adv. Healthc. Mater.*, 2019, **8**, 1900132.

[14] A. A. Buglak, M. A. Kapitonova, Y. L. Vechtomova and T. A. Telegina, *Int. J. Mol. Sci.*, 2022, **23**, 15222.

[15] A. Jabłoński, *Z. Physik*, 1935, **95**, 53–65.

[16] *Femtosecond spectroscopy*, `https://www.temps.phc.uni-kiel.de/en/research/laboratories-and-instrumentation/femtosecond-spectroscopy`.

[17] D. M. Neumark, *Annu. Rev. Phys. Chem.*, 2001, **52**, 255–277.

[18] A. Stolow, *Annu. Rev. Phys. Chem.*, 2003, **54**, 89–119.

[19] A. Stolow, A. E. Bragg and D. M. Neumark, *Chem. Rev.*, 2004, **104**, 1719–1758.

[20] T. Suzuki, *Annu. Rev. Phys. Chem.*, 2006, **57**, 555–592.

[21] R. Berera, R. van Grondelle and J. T. M. Kennis, *Photosynth. Res.*, 2009, **101**, 105–118.

[22] S. W. Crane, M. Garrow, P. D. Lane, K. Robertson, A. Waugh, J. M. Woolley, V. G. Stavros, M. J. Paterson, S. J. Greaves and D. Townsend, *J. Phys. Chem. A*, 2023, **127**, 6425–6436.

[23] J. I. Selco, P. L. Holt and R. B. Weisman, *J. Chem. Phys.*, 1983, **79**, 3269–3278.

[24] R. W. Anderson, Jr., D. E. Damschen, G. W. Scott and L. D. Talley, *J. Chem. Phys.*, 1979, **71**, 1134–1140.

[25] B. Stankus, H. Yong, J. Ruddock, L. Ma, A. M. Carrascosa, N. Goff, S. Boutet, X. Xu, N. Zotev, A. Kirrander, M. Minitti and P. M. Weber, *J. Phys. B*, 2020.

[26] A. Barty, J. Küpper and H. N. Chapman, *Annu. Rev. Phys. Chem.*, 2012, **64**, 130118162050005.

[27] H. Yong, X. Xu, J. M. Ruddock, B. Stankus, A. M. Carrascosa, N. Zotev, D. Bellshaw, W. Du, N. Goff, Y. Chang, S. Boutet, S. Carbajo, J. E. Koglin, M. Liang, J. S. Robinson, A. Kirrander, M. P. Minitti and P. M. Weber, *Proc. Nat. Acad. Sci.*, 2021, **118**, e2021714118.

[28] M. Centurion, T. J. Wolf and J. Yang, *Annu. Rev. Phys. Chem.*, 2022, **73**, 21–42.

[29] D. Filippetto, P. Musumeci, R. Li, B. Siwick, M. Otto, M. Centurion and J. Nunes, *Rev. Mod. Phys.*, 2022, **94**, 045004.

[30] P. Chakraborty, Y. Liu, S. McClung, T. Weinacht and S. Matsika, *J. Phys. Chem. Lett.*, 2021, **12**, 5099–5104.

[31] M. Simmermacher, P. M. Weber and A. Kirrander, in *Structural Dynamics with X-ray and Electron Scattering*, Royal Society of Chemistry, 2023, vol. 25, pp. 85–125.

[32] H. Yong, A. M. Carrascosa, L. Ma, B. Stankus, M. P. Minitti, A. Kirrander and P. M. Weber, *Faraday Discuss.*, 2021, **228**, 104–122.

[33] M. Born and R. Oppenheimer, *Ann. Phys.*, 1927, **389**, 457–484.

[34] M. Born, K. Huang, M. Born and K. Huang, *Dynamical Theory of Crystal Lattices*, Oxford University Press, Oxford, New York, 1998.

[35] S. Matsika, in *Reviews in Computational Chemistry*, John Wiley & Sons, Ltd, 2007, pp. 83–124.

[36] G. J. Atchity, S. S. Xantheas and K. Ruedenberg, *J. Chem. Phys.*, 1991, **95**, 1862–1876.

[37] C. A. Farfan and D. B. Turner, *Phys. Chem. Chem. Phys.*, 2020, **22**, 20265–20283.

[38] M. S. Schuurman and A. Stolow, *Annu. Rev. Phys. Chem.*, 2018, **69**, 427–450.

[39] C. M. Marian, *WIREs Comput. Mol. Sci.*, 2012, **2**, 187–203.

[40] T. J. Penfold, E. Gindensperger, C. Daniel and C. M. Marian, *Chem. Rev.*, 2018, **118**, 6975–7025.

[41] M. A. El-Sayed, *J. Chem. Phys.*, 1963, **38**, 2834–2838.

[42] H. D. Meyer, U. Manthe and L. S. Cederbaum, *Chem. Phys. Lett.*, 1990, **165**, 73–78.

[43] J. C. Tully, *Faraday Discuss.*, 1998, **110**, 407–419.

[44] S. Mai, P. Marquetand and L. González, in *Quantum Chemistry and Dynamics of Excited States*, John Wiley & Sons, Ltd, 2020, pp. 499–530.

[45] M. Barbatti, *WIREs Comput. Mol. Sci.*, 2011, **1**, 620–633.

[46] D. V. Shalashilin, *J. Chem. Phys.*, 2009, **130**, 244101.

[47] M. Ben-Nun and T. J. Martınez, *Chem. Phys. Lett.*, 1998, **298**, 57–65.

[48] L. Verlet, *Phys. Rev.*, 1967, **159**, 98–103.

[49] S. Mai, P. Marquetand and L. González, *Int. J. Quant. Chem.*, 2015, **115**, 1215.

[50] S. Mai, M. Richter, M. Ruckenbauer, M. Oppel, P. Marquetand and L. González, *SHARC: Surface Hopping Including Arbitrary Couplings - Program Package for Non-Adiabatic Dynamics*, sharc-md.org, 2014.

[51] S. Hammes-Schiffer and J. C. Tully, *J. Chem. Phys.*, 1994, **101**, 4657–4667.

[52] J. Pittner, H. Lischka and M. Barbatti, *Chem. Phys.*, 2009, **356**, 147–152.

[53] J. C. Tully, *J. Chem. Phys.*, 1990, **93**, 1061–1071.

[54] G. Granucci and M. Persico, *J. Chem. Phys.*, 2007, **126**, 134114.

[55] G. Granucci, M. Persico and A. Zoccante, *J. Chem. Phys.*, 2010, **133**, 134111.

[56] E. Wigner, *Phys. Rev.*, 1932, **40**, 749–759.

[57] J. P. Dahl and M. Springborg, *J. Chem. Phys.*, 1988, **88**, 4535–4547.

[58] S. Mai, M. Richter, M. Heindl, M. F. S. J. Menger, A. Atkins, M. Ruckenbauer, F. Plasser, L. M. Ibele, S. Kropf, M. Oppel, P. Marquetand and L. González, *SHARC2.1: Surface Hopping Including Arbitrary Couplings — Program package for Non-Adiabatic Dynamics*, sharc-md.org, 2019.

[59] T. V. Papineau, D. Jacquemin and M. Vacher, *J. Phys. Chem. Lett.*, 2024, **15**, 636–643.

[60] D. R. Hartree and W. Hartree, *Proc. R. Soc. Lond. A Math. Phys. Sci.*, 1997, **150**, 9–33.

[61] B. O. Roos, P. R. Taylor and P. E. M. Sigbahn, *Chem. Phys.*, 1980, **48**, 157–173.

[62] P. Å. Malmqvist and B. O. Roos, *Chem. Phys. Lett.*, 1989, **155**, 189–194.

[63] J. Olsen, *Int. J. Quantum Chem.*, 2011, **111**, 3267–3272.

[64] L. Serrano-Andrés, B. O. Roos and M. Merchán, *Theoret. Chim. Acta*, 1994, **87**, 387–402.

[65] J. M. O. Matos, B. O. Roos and P. Å. Malmqvist, *J. Chem. Phys.*, 1987, **86**, 1458–1466.

[66] K. Andersson, P. Å. Malmqvist, B. O. Roos, A. J. Sadlej and K. Wolinski, *J. Phys. Chem.*, 1990, **94**, 5483–5488.

[67] K. Andersson, P. Å. Malmqvist and B. O. Roos, *J. Chem. Phys.*, 1992, **96**, 1218–1226.

[68] R. Lindh and I. F. Galván, in *Quantum Chemistry and Dynamics of Excited States*, John Wiley & Sons, Ltd, 2020, pp. 299–353.

[69] J. Finley, P. Å. Malmqvist, B. O. Roos and L. Serrano-Andrés, *Chem. Phys. Lett.*, 1998, **288**, 299–306.

[70] T. Shiozaki, W. Győrffy, P. Celani and H.-J. Werner, *J. Chem. Phys.*, 2011, **135**, 081106.

[71] S. Sen and I. Schapiro, *Mol. Phys.*, 2018, **116**, 2571–2582.

[72] D. Roca-Sanjuán, F. Aquilante and R. Lindh, *WIREs Comput. Mol. Sci.*, 2012, **2**, 585–603.

[73] B. O. Roos and K. Andersson, *Chem. Phys. Lett.*, 1995, **245**, 215–223.

[74] J. Schirmer, *Phys. Rev. A*, 1982, **26**, 2395–2416.

[75] A. Dreuw and M. Wormit, *WIREs Comput. Mol. Sci.*, 2015, **5**, 82–95.

[76] F. Plasser, R. Crespo-Otero, M. Pederzoli, J. Pittner, H. Lischka and M. Barbatti, *J. Chem. Theory Comput.*, 2014, **10**, 1395–1405.

[77] D. Tuna, D. Lefrancois, Wolański, S. Gozem, I. Schapiro, T. Andruniów, A. Dreuw and M. Olivucci, *J. Chem. Theory Comput.*, 2015, **11**, 5758–5781.

[78] L. Hutton and B. F. E. Curchod, *ChemPhotoChem*, 2022, **6**, e202200151.

[79] S. Grimme, *J. Chem. Phys.*, 2003, **118**, 9095–9102.

[80] A. Tajti, L. Tulipán and P. G. Szalay, *J. Chem. Theory Comput.*, 2020, **16**, 468–474.

[81] A. Tajti and P. G. Szalay, *J. Chem. Theory Comput.*, 2019, **15**, 5523–5531.

[82] A. Hellweg, S. A. Grün and C. Hättig, *Phys. Chem. Chem. Phys.*, 2008, **10**, 4119–4127.

[83] O. Christiansen, H. Koch and P. Jørgensen, *Chem. Phys. Lett.*, 1995, **243**, 409–418.

[84] J. F. Stanton and R. J. Bartlett, *J. Chem. Phys.*, 1993, **98**, 7029–7039.

[85] R. J. Bartlett and M. Musiał, *Rev. Mod. Phys.*, 2007, **79**, 291–352.

[86] P. Hohenberg and W. Kohn, *Phys. Rev.*, 1964, **136**, B864–B871.

[87] W. Kohn and L. J. Sham, *Phys. Rev.*, 1965, **140**, A1133–A1138.

[88] J. P. Perdew, J. A. Chevary, S. H. Vosko, K. A. Jackson, M. R. Pederson, D. J. Singh and C. Fiolhais, *Phys. Rev. B*, 1992, **46**, 6671–6687.

[89] C. Adamo and V. Barone, *J. Chem. Phys.*, 1999, **110**, 6158–6170.

[90] J. P. Perdew, K. Burke and M. Ernzerhof, *Phys. Rev. Lett.*, 1996, **77**, 3865–3868.

[91] K. Burke, *J. Chem. Phys.*, 2012, **136**, 150901.

[92] R. E. Stratmann, G. E. Scuseria and M. J. Frisch, *J. Chem. Phys.*, 1998, **109**, 8218–8224.

[93] D. J. Tozer, R. D. Amos, N. C. Handy, B. O. Roos and L. Serrano-Andres, *Mol. Phys.*, 1999, **97**, 859–868.

[94] D. J. Tozer, *J. Chem. Phys.*, 2003, **119**, 12697–12699.

[95] M. Simmermacher, N. E. Henriksen, K. B. Møller, A. Moreno Carrascosa and A. Kirrander, *J. Chem. Phys.*, 2019, **151**, 174302.

[96] M. Simmermacher, N. E. Henriksen, K. B. Møller, A. Moreno Carrascosa and A. Kirrander, *Phys. Rev. Lett.*, 2019, **122**, 073003.

[97] A. M. Carrascosa, H. Yong, D. L. Crittenden, P. M. Weber and A. Kirrander, *J. Chem. Theory Comp.*, 2019, **15**, 2836–2846.

[98] N. Zotev, A. M. Carrascosa, M. Simmermacher and A. Kirrander, *J. Chem. Theory Comput.*, 2020, **16**, 2594–2605.

[99] T. Northey, N. Zotev and A. Kirrander, *J. Chem. Theory Comput.*, 2014, **10**, 4911.

[100] T. Northey, A. M. Carrascosa, S. Schäfer and A. Kirrander, *J. Chem. Phys.*, 2016, **145**, 154304.

[101] A. M. Carrascosa, T. Northey and A. Kirrander, *Phys. Chem. Chem. Phys.*, 2017, **19**, 7853–7863.

[102] T. Northey and A. Kirrander, *J. Phys. Chem. A*, 2019, **123**, 3395–3406.

[103] P. Debye, *Ann. Phys.*, 1915, **46**, 809.

[104] A. Kirrander and P. M. Weber, *Appl. Science*, 2017, **7**, 534.

[105] *International Tables for Crystallography Volume C: Mathematical, physical and chemical tables*, ed. E. Prince, Wiley, 2006th edn., 2006.

[106] R. F. Stewart, E. R. Davidson and W. T. Simpson, *J. Chem. Phys.*, 1965, **42**, 3175.

[107] R. F. Stewart, J. Bentley and B. Goodman, *J. Chem. Phys.*, 1975, **63**, 3786.

[108] P. Chakraborty and S. Matsika, *WIREs Comput. Mol. Sci.*, 2024, **14**, e1715.

[109] C. Melania Oana and A. I. Krylov, *J. Chem. Phys.*, 2009, **131**, 124114.

[110] C. Melania Oana and A. I. Krylov, *J. Chem. Phys.*, 2007, **127**, 234106.

[111] S. Gozem and A. I. Krylov, *WIREs Comput. Mol. Sci.*, 2022, **12**, 1–22.

[112] Z. Mašín, J. Benda, J. D. Gorfinkiel, A. G. Harvey and J. Tennyson, *Comput. Phys. Commun.*, 2020, **249**, 107092.

[113] L. Bertram, P. M. Weber and A. Kirrander, *Faraday Discuss.*, 2023, 269–293.

[114] W. Fuß, S. Panja, W. E. Schmid and S. A. Trushin, *Mol. Phys.*, 2006, **104**, 1133–1143.

[115] W. G. Dauben, B. Disanayaka, D. J. H. Funhoff, B. Zhou, B. E. Kohler and D. E. Schilke, *J. Am. Chem. Soc.*, 1991, **113**, 8367–8374.

[116] J. I. Brauman, L. E. Ellis and E. E. van Tamelen, *J. Am. Chem. Soc.*, 1966, **88**, 846–848.

[117] E. E. Van Tamelen, J. I. Brauman and L. E. Ellis, *J. Am. Chem. Soc.*, 1971, **93**, 6145–6151.

[118] G. D. Andrews and J. E. Baldwin, *J. Am. Chem. Soc.*, 1977, **99**, 4851–4853.

[119] P. Celani, F. Bernardi, M. Olivucci and M. A. Robb, *J. Chem. Phys.*, 1995, **102**, 5733–5742.

[120] M. Squillacote and T. C. Semple, *J. Am. Chem. Soc.*, 1990, **112**, 5546–5551.

[121] M. Olivucci, I. N. Ragazos, F. Bernardi and M. A. Robb, *J. Am. Chem. Soc.*, 1993, **115**, 3710–3721.

[122] P. Chakraborty, Y. Liu, T. Weinacht and S. Matsika, *J. Chem. Phys.*, 2020, **152**, 174302.

[123] W. Fuß, W. E. Schmid and S. A. Trushin, *Chem. Phys.*, 2005, **316**, 225–234.

[124] O. Schalk, A. E. Boguslavskiy and A. Stolow, *J. Phys. Chem. A*, 2010, **114**, 4058–4064.

[125] F. Rudakov and P. M. Weber, *J. Phys. Chem. A*, 2010, **114**, 4501–4506.

[126] T. S. Kuhlman, W. J. Glover, T. Mori, K. B. Møller and T. J. Martinez, *Faraday Discuss.*, 2012, **157**, 193.

[127] H. Nakano, T. Tsuneda, T. Hashimoto and K. Hirao, *J. Chem. Phys.*, 1996, **104**, 2312–2320.

[128] L. Serrano-Andres, M. Merchan, I. Nebot-Gil, B. O. Roos and M. Fulscher, *J. Am. Chem. Soc.*, 1993, **115**, 6184–6197.

[129] Y. J. Bomble, K. W. Sattelmeyer, J. F. Stanton and J. Gauss, *J. Chem. Phys.*, 2004, **121**, 5236–5240.

[130] *BAGEL, Brilliantly Advanced General Electronic-structure Library. http://www.nubakery.org under the GNU General Public License.*

[131] T. Shiozaki, *WIREs Comput. Mol. Sci.*, 2018, **8**, e1331.

[132] F. J. A. Ferrer and F. Santoro, *Phys. Chem. Chem. Phys.*, 2012, **14**, 13549–13563.

[133] J. Cerezo and F. Santoro, *J. Comput. Chem.*, 2023, **44**, 626–643.

[134] *TURBOMOLE V7.7 2020, a development of University of Karlsruhe and Forschungszentrum Karlsruhe GmbH, 1989-2007,TURBOMOLE GmbH, since 2007; available from* `https://www.turbomole.org`.

[135] M. Richter, P. Marquetand, J. González-Vázquez, I. Sola and L. González, *J. Chem. Theory Comput.*, 2011, **7**, 1253–1258.

[136] S. Mai, P. Marquetand and L. González, *WIREs Comput. Mol. Sci.*, 2018, **8**, e1370.

[137] *TURBOMOLE V7.5 2020, a development of University of Karlsruhe and Forschungszentrum Karlsruhe GmbH, 1989-2007,TURBOMOLE GmbH, since 2007; available from* `https://www.turbomole.org`.

[138] M. Barbatti, G. Granucci, M. Ruckenbauer, F. Plasser, R. Crespo-Otero, J. Pittner, M. Persico and H. Lischka, *NEWTON-X: A package for Newtonian Dynamics Close to the Crossing Seam (v. 2.4)*, Available via the Internet at www.newtonx.org, 2018.

[139] M. Barbatti, M. Ruckenbauer, F. Plasser, J. Pittner, G. Granucci, M. Persico and H. Lischka, *WIREs Comput. Mol. Sci.*, 2014, **4**, 26–33.

[140] F. Neese, *WIREs Comput. Mol. Sci.*, 2012, **2**, 73–78.

[141] K. Ishida, K. Morokuma and A. Komornicki, *J. Chem. Phys.*, 1977, **66**, 2153–2156.

[142] G. Henkelman and H. Jónsson, *J. Chem. Phys.*, 2000, **113**, 9978–9985.

[143] I. Fdez. Galván, M. Vacher, A. Alavi, C. Angeli, F. Aquilante, J. Autschbach, J. J. Bao, S. I. Bokarev, N. A. Bogdanov, R. K. Carlson, L. F. Chibotaru, J. Creutzberg, N. Dattani, M. G. Delcey, S. S. Dong, A. Dreuw, L. Freitag, L. M. Frutos, L. Gagliardi, F. Gendron, A. Giussani, L. González, G. Grell, M. Guo, C. E. Hoyer, M. Johansson, S. Keller, S. Knecht, G. Kovačević, E. Källman, G. Li Manni, M. Lundberg, Y. Ma, S. Mai, J. P. Malhado, P. Å. Malmqvist, P. Marquetand, S. A. Mewes, J. Norell, M. Olivucci, M. Oppel, Q. M. Phung, K. Pierloot, F. Plasser, M. Reiher, A. M. Sand, I. Schapiro, P. Sharma, C. J. Stein, L. K. Sørensen, D. G. Truhlar, M. Ugandi, L. Ungur, A. Valentini, S. Vancoillie, V. Veryazov, O. Weser, T. A. Wesołowski, P.-O. Widmark, S. Wouters, A. Zech, J. P. Zobel and R. Lindh, *J. Chem. Theory Comput.*, 2019, **15**, 5925–5964.

[144] F. Aquilante, J. Autschbach, A. Baiardi, S. Battaglia, V. A. Borin, L. F. Chibotaru, I. Conti, L. De Vico, M. Delcey, I. Fdez. Galván, N. Ferré, L. Freitag, M. Garavelli, X. Gong, S. Knecht, E. D. Larsson, R. Lindh, M. Lundberg, P. Å. Malmqvist, A. Nenov, J. Norell, M. Odelius, M. Olivucci, T. B. Pedersen, L. Pedraza-González, Q. M. Phung, K. Pierloot, M. Reiher, I. Schapiro, J. Segarra-Martí, F. Segatta, L. Seijo, S. Sen, D.-C. Sergentu, C. J. Stein, L. Ungur, M. Vacher, A. Valentini and V. Veryazov, *J. Chem. Phys.*, 2020, **152**, 214117.

[145] R. P. Frueholz, W. M. Flicker, O. A. Mosher and A. Kuppermann, *J. Chem. Phys.*, 1979, **70**, 2003–2013.

[146] V. Santolini, J. P. Malhado, M. A. Robb, M. Garavelli and M. J. Bearpark, *Mol. Phys.*, 2015, **113**, 1978–1990.

[147] I. Fdez. Galván, M. G. Delcey, T. B. Pedersen, F. Aquilante and R. Lindh, *J. Chem. Theory Comput.*, 2016, **12**, 3636–3653.

[148] S. Wilsey and K. N. Houk, *J. Am. Chem. Soc.*, 2000, **122**, 2651–2652.

[149] R. Crespo-Otero and M. Barbatti, *Theor. Chem. Acc.*, 2012, **131**, 1237.

[150] L. Huang, L. Bertram, L. Ma, N. Goff, S. W. Crane, A. Odate, T. Northey, A. M. Carrascosa, M. Simmermacher, S. B. Muvva, J. D. Geiser, M. J. Lueckheide, Z. Phelps, M. Liang, X. Cheng, R. Forbes, J. S. Robinson, M. J. Hayes, F. Allum, A. E. Green, K. Lopata, A. Rudenko, T. J. A. Wolf, M. Centurion, D. Rolles, M. P. Minitti, A. Kirrander and P. M. Weber, *J. Phys. Chem. A*, 2024, **128**, 4992–4998.

[151] A. Sabljić and R. McDiarmid, *J. Chem. Phys.*, 1990, **93**, 3850–3855.

[152] J. M. Ruddock, N. Zotev, B. Stankus, H.-W. Yong, D. Bellshaw, S. Boutet, T. J. Lane, M. Liang, S. Carbajo, W. Du, A. Kirrander, M. P. Minitti and P. M. Weber, *Angew. Chem. Int. Ed.*, 2019, **58**, 6371–6375.

[153] J. M. Budarz, M. P. Minitti, D. V. Cofer-Shabica, B. Stankus, A. Kirrander, J. B. Hastings and P. M. Weber, *J. Phys. B*, 2016, **49**, 034001.

[154] M. P. Minitti, J. M. Budarz, A. Kirrander, J. Robinson, T. J. Lane, D. Ratner, K. Saita, T. Northey, B. Stankus, V. Cofer-Shabica, J. Hastings and P. M. Weber, *Faraday Discuss.*, 2014, **171**, 81.

[155] M. P. Minitti, J. M. Budarz, A. Kirrander, J. S. Robinson, D. Ratner, T. J. Lane, D. Zhu, J. M. Glownia, M. Kozina, H. T. Lemke, M. Sikorski, Y. Feng, S. Nelson, K. Saita, B. Stankus, T. Northey, J. B. Hastings and P. M. Weber, *Phys. Rev. Lett.*, 2015, **114**, 255501.

[156] W. O. Razmus, K. Acheson, P. Bucksbaum, M. Centurion, E. Champenois, I. Gabalski, M. C. Hoffman, A. Howard, M.-F. Lin, Y. Liu, P. Nunes, S. Saha, X. Shen, M. Ware, E. M. Warne, T. Weinacht, K. Wilkin, J. Yang, T. J. A. Wolf, A. Kirrander, R. S. Minns and R. Forbes, *Phys. Chem. Chem. Phys.*, 2022, **24**, 15416–15427.

[157] I. Gabalski, M. Sere, K. Acheson, F. Allum, S. Boutet, G. Dixit, R. Forbes, J. M. Glownia, N. Goff, K. Hegazy, A. J. Howard, M. Liang, M. P. Minitti, R. S. Minns, A. Natan, N. Peard, W. O. Rasmus, R. J. Sension, M. R. Ware, P. M. Weber, N. Werby, T. J. A. Wolf, A. Kirrander and P. H. Bucksbaum, *J. Chem. Phys.*, 2022, **157**, 164305.

[158] K. Acheson and A. Kirrander, *J. Chem. Theory Comput.*, 2023, **19**, 2721–2734.

[159] B. Stankus, H. Yong, N. Zotev, J. M. Ruddock, D. Bellshaw, T. J. Lane, M. Liang, S. Boutet, S. Carbajo, J. S. Robinson, W. Du, N. Goff, Y. Chang, J. E. Koglin, M. P. Minitti, A. Kirrander and P. M. Weber, *Nat. Chem.*, 2019, **11**, 716–721.

[160] H. Yong, J. M. Ruddock, B. Stankus, L. Ma, W. Du, N. Goff, Y. Chang, N. Zotev, D. Bellshaw, S. Boutet, S. Carbajo, J. E. Koglin, M. Liang, J. S. Robinson, A. Kirrander, M. P. Minitti and P. M. Weber, *J. Chem. Phys.*, 2019, **151**, 084301.

[161] D. Bellshaw, R. S. Minns and A. Kirrander, *Phys. Chem. Chem. Phys.*, 2019, **21**, 14226–14237.

[162] J. M. Ruddock, H. Yong, B. Stankus, W. Du, N. Goff, Y. Chang, A. Odate, A. M. Carrascosa, D. Bellshaw, N. Zotev, M. Liang, S. Carbajo, J. Koglin, J. S. Robinson, S. Boutet, A. Kirrander, M. P. Minitti and P. M. Weber, *Sci. Adv.*, 2019, **5**, eaax6625.

[163] A. M. Carrascosa, J. P. Coe, M. Simmermacher, M. J. Paterson and A. Kirrander, *Phys. Chem. Chem. Phys.*, 2022, **24**, 24542–24552.

[164] J. P. Coe, A. Moreno Carrascosa, M. Simmermacher, A. Kirrander and M. J. Paterson, *J. Chem. Theory Comp.*, 2022, **18**, 6690–6699.

[165] B. Stankus, N. Zotev, D. M. Rogers, Y. Gao, A. Odate, A. Kirrander and P. M. Weber, *J. Chem. Phys.*, 2018, **148**, 194306.

[166] M. Tudorovskaya, R. S. Minns and A. Kirrander, *Phys. Chem. Chem. Phys.*, 2018, **20**, 17714–17726.

[167] J. Yang, X. Zhu, J. P. F. Nunes, J. K. Yu, R. M. Parrish, T. J. A. Wolf, M. Centurion, M. Gühr, R. Li, Y. Liu, B. Moore, M. Niebuhr, S. Park, X. Shen, S. Weathersby, T. Weinacht, T. J. Martinez and X. Wang, *Science*, 2020, **368**, 885–889.

[168] M. Stefanou, K. Saita, D. V. Shalashilin and A. Kirrander, *Chem. Phys. Lett.*, 2017, **683**, 300–305.

[169] C. C. Pemberton, Y. Zhang, K. Saita, A. Kirrander and P. M. Weber, *J. Phys. Chem. A*, 2015, **119**, 8832.

[170] M. Garrow, L. Bertram, A. Winter, A. W. Prentice, S. W. Crane, P. D. Lane, S. J. Greaves, M. J. Paterson, A. Kirrander and D. Townsend, *Commun. Chem.*, 2025, **8**, 1–11.

[171] L. D. Elliott, S. Kayal, M. W. George and K. Booker-Milburn, *J. Am. Chem. Soc.*, 2020, **142**, 14947–14956.

[172] Y. Harabuchi, K. Saita and S. Maeda, *Photochem. Photobiol. Sci.*, 2018, **17**, 315–322.

[173] T. J. Krogmeier, E. S. Pappas, K. A. Reardon, M. R. Rivera, K. Head-Marsden, B. F. Parsons and A. W. Schlimgen, *J. Chem. Phys.*, 2023, **159**, 134305.

[174] M. Etinski and C. M. Marian, *Phys. Chem. Chem. Phys.*, 2017, **19**, 13828–13837.

[175] B. G. Levine, J. D. Coe, A. M. Virshup and T. J. Martinez, *Chem. Phys.*, 2008, **347**, 3.

[176] A. Klamt and G. Schüürmann, *J. Chem. Soc., Perkin Trans. 2*, 1993, 799–805.

[177] D. W. Boldridge and G. W. Scott, *J. Chem. Phys.*, 1986, **84**, 6790–6798.

[178] S. J. Komorowski, Z. R. Grabowski and W. Zielenkiewicz, *J. Photochem.*, 1985, **30**, 141–151.

[179] M. Terazima and T. Azumi, *Chem. Phys. Lett.*, 1987, **141**, 237–240.

[180] S. Leach, N. C. Jones, S. V. Hoffmann and S. Un, *RSC Adv.*, 2019, **9**, 5121–5141.

[181] S. Leach, N. C. Jones, S. V. Hoffmann and S. Un, *J. Phys. Chem. A*, 2018, **122**, 5832–5847.

[182] J. P. Zobel, M. Heindl, F. Plasser, S. Mai and L. González, *Acc. Chem. Res.*, 2021, **54**, 3760–3771.

[183] S. Polonius, O. Zhuravel, B. Bachmair and S. Mai, *J. Chem. Theory Comput.*, 2023, **19**, 7171–7186.

[184] C. C. Moser, J. M. Keske, K. Warncke, R. S. Farid and P. L. Dutton, *Nature*, 1992, **355**, 796–802.

[185] M. R. Wasielewski, *Chem. Rev.*, 1992, **92**, 435–461.

[186] S. M. Falke, C. A. Rozzi, D. Brida, M. Maiuri, M. Amato, E. Sommer, A. De Sio, A. Rubio, G. Cerullo, E. Molinari and C. Lienau, *Science*, 2014, **344**, 1001–1005.

[187] H. J. Wörner, C. A. Arrell, N. Banerji, A. Cannizzo, M. Chergui, A. K. Das, P. Hamm, U. Keller, P. M. Kraus, E. Liberatore, P. Lopez-Tarifa, M. Lucchini, M. Meuwly, C. Milne, J.-E. Moser, U. Rothlisberger, G. Smolentsev, J. Teuscher, J. A. van Bokhoven and O. Wenger, *Struc. Dyn.*, 2017, **4**, 061508.

[188] S. Deb, X. Cheng and P. M. Weber, *J. Phys. Chem. Lett.*, 2013, **4**, 2780–2784.

[189] X. Cheng, Y. Zhang, E. Jónsson, H. Jónsson and P. M. Weber, *Nat. Commun.*, 2016, **7**, 11013.

[190] X. Cheng, Personal communication.

[191] Y. Zhang, H. Jónsson and P. M. Weber, *Phys. Chem. Chem. Phys.*, 2017, **19**, 26403–26411.

[192] Y. Zhang, S. Deb, H. Jónsson and P. M. Weber, *J. Phys. Chem. Lett.*, 2017, **8**, 3740–3744.

[193] Z. A. Ali, F. W. Aquino and B. M. Wong, *Nat. Commun.*, 2018, **9**, 4733.

[194] X. Cheng, E. Jónsson, H. Jónsson and P. M. Weber, *Nat. Commun.*, 2018, **9**, 5348.

[195] M. Gałyńska, V. Ásgeirsson, H. Jónsson and R. Bjornsson, *J. Phys. Chem. Lett.*, 2021, **12**, 1250–1255.

[196] M. Reimann, C. Kirsch, D. Sebastiani and M. Kaupp, *Nat. Commun.*, 2024, **15**, 293.

[197] S. F. Nelsen and J. M. Buschek, *J. Am. Chem. Soc.*, 1974, **96**, 7930–7934.

[198] H. Yong, N. Zotev, J. M. Ruddock, B. Stankus, M. Simmermacher, A. M. Carrascosa, W. Du, N. Goff, Y. Chang, D. Bellshaw, M. Liang, S. Carbajo, J. E. Koglin, J. S. Robinson, S. Boutet, M. P. Minitti, A. Kirrander and P. M. Weber, *Nat. Commun.*, 2020, **11**, 2157.

[199] D. Rolles, Personal communication.

[200] M. Centurion, Personal communication.

[201] P. M. Weber, Personal communication.